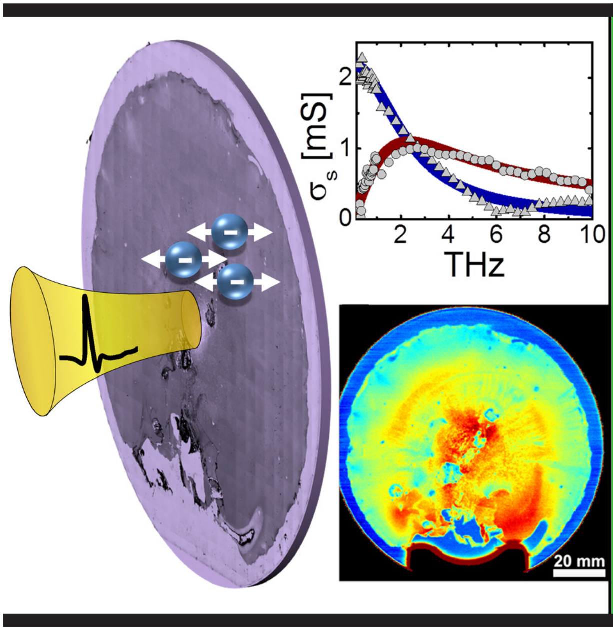
σs [mS]
0
1
2
2
4
6
8
10
THz
20 mm

Terahertz transport dynamics of graphene charge carriers

Jonas Christian Due Buron
PhD Thesis
October 2013

DTU Fotonik
Department of Photonics Engineering

Terahertz transport dynamics of graphene charge carriers

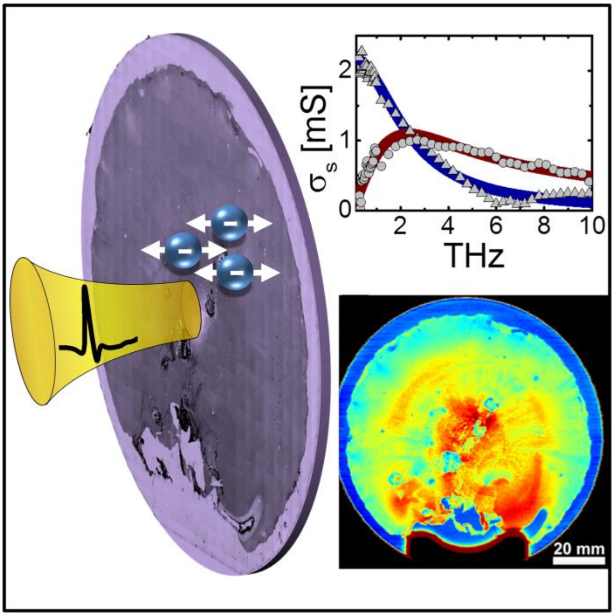
σ_s [mS]
2
1
0
2
4
6
8
10
THz
20 mm

Jonas Christian Due Buron

October 2013

DTU Fotonik
Department of Photonics Engineering

DTU Nanotech
Department of Micro- and Nanotechnology

Abstract

The electronic transport dynamics of graphene charge carriers at femtosecond (10^{-15} s) to picosecond ($10^{-12}\,\mathrm{s}$) time scales are investigated using terahertz ($10^{12}\,\mathrm{Hz}$) time-domain spectroscopy (THz-TDS). The technique uses sub-picosecond pulses of electromagnetic radiation to gauge the electrodynamic response of thin conducting films at up to multi-terahertz frequencies. In this thesis THz-TDS is applied towards two main goals; (1) investigation of the fundamental carrier transport dynamics in graphene at femtosecond to picosecond timescales and (2) application of terahertz time-domain spectroscopy to rapid and non-contact electrical characterization of large-area graphene, relevant for industrial integration.

We show that THz-TDS is an accurate and reliable probe of graphene sheet conductance, and that the technique provides insight into fundamental aspects of the nanoscopic nature of conduction in graphene films. This is demonstrated by experimental observation of diffusive transport as well as signatures of preferential back-scattering of carriers on a nanoscopic scale in poly-crystalline graphene, which may be related to reflections at crystal domain boundaries. This is the first observation of preferential back-scattering of graphene charge carriers in THz-TDS measurements, and the results are expected to have a significant impact on the graphene and THz-TDS communities, as they may provide insight into the impact of nanoscopic morphology on the electrical conduction in poly-crystalline graphene. Through THz-TDS measurements with accurate carrier density control by careful electrical back-gating, we find that terahertz conductance scales linearly with carrier density, consistent with charge transport limited by long-range scattering on charged impurities, which is also observed in most contact-based transport measurements.

By demonstrations of wafer-scale sheet conductance mapping and large-area field-effect mobility mapping, it is shown that the non-contact nature of THz-TDS measurements facilitates the rapid and reliable large-scale characterization of graphene electronic properties and their uniformity, that might be viewed as a vital requirement for industrial implementation of the material. We find significant spatial variations in carrier mobility of a factor of 2-3 on a scale of just few millimeters, which highlights the importance of techniques that provide highly statistical or spatially resolved approaches to electronic characterization of large-area graphene. In a comparative study, we observe significant suppression of DC micrometer-scale transport, probed using micro four-point probe conductance mapping, relative to AC nanoscopic transport, probed by THz-TDS conductance mapping. A detailed analysis of micro four-point probe, THz-TDS and Raman spectroscopy data reveals that the suppression of micrometer-scale conductance is a signature of electrical defects on the scale of 10 μm, giving rise to 1D-like micrometer-scale transport.

Resume

Den elektroniske transport dynamic for graphene ladningsbærere på femtosekund (10^{-15} s) til picosekund (10^{-12} s) tidsskala undersøges ved hjælp af terahertz tids-domæne spektroskopi (THz-TDS). Teknikken, som benytter sub-picosekund pulser af elektromagnetisk stråling til at måle det elektrodynamiske respons for tynde, lendende film ved op til multi-THz frekvenser, anvendes i denne afhandling med henblik på 2 primære mål; (1) undersøgelse af fundamental dynamik i ladningsbærertransport for graphene på femtosekund til picosekund tidsskalaer og (2) anvendelse af terahertz tids-domæne spektroskopi til hurtig og kontaktfri elektrisk karakterisering af stor-skala graphene, relevant for industrielle anvendelser.

Vi viser at THz-TDS giver et nøjagtigt og pålideligt mål for fladekonduktansen af graphene såvel som fundamentale aspekter af den elektriske ledningsproces i graphene. Dette demonstreres ved eksperimentel observation af diffusiv ladningsransport og signaturer fra præferentiel tilbagespredning af graphene ladningsbærere på nanoskopisk skala i polykrystallinsk graphene, som kan være relateret til reflektioner ved krystaldomænegrænser. Dette er den første observation af præferentiel tilbagespredning af graphene ladningsbærere i THz-TDS målinger, og det forventes at resultaterne vil have stor betydning indenfor graphene og THz-TDS felterne, da de kan give indsigt i indflyselsen af nanoskopisk morfologi på den elektriske ledningsevne i polykrystallinsk graphene. Ud fra THz-TDS målinger med præcis control over ladningsbærertætheden ved hjælp af nøje udført elektrisk forspænding, finder vi at terahertz konduktansen skalerer lineært med ladningsbærertæthed, hvilket afspejler ladningstransport begrænset af langdistance spredning af ladningsbærere på ladede urenheder, som også observeres i de fleste kontakt-baserede transport målinger.

Ved demonstration af wafer-skala fladekonduktans-billeddannelse og stor-skala felteffekt bevægeligheds-billeddannelse viser vi at den kontakt-fri natur af THz-TDS målinger muliggør den hurtige og pålidelige stor-skala karakterisering af graphene’s elektroniske egenskaber og deres uniformitet, som kan anses for at være af afgørende nødvendighed for industriel implementering af materialet. Vi finder betydelig rumlig variation i ladningsbærerbevægeligheden på en faktor 2-3 over kun få millimeter, hvilket understreger vigtigheden af teknikker der muliggør statistiske eller rumligt opløste tilgange til elektronisk karakterisering af stor-skala graphene. I en komparativ undersøgelse observerer vi signifikant reduktion af DC

mikrometer-skala transport, udmålt ved hjælp af mikro-firpunkts-probe konduktans kortlægning, i forhold til AC nanoskopisk transport, udmålt ved hjælp af THz-TDS konduktans kortlægning. En detaljeret analyse af mikro-firpunkts-probe-, THz-TDS- og Raman spektroskopi-data afslører at reduktionen af mikrometer-skala ledningsevnen er et resultat af elektriske defekter på en 10 μm-skala, som giver anledning til 1D-lignende mikrometer-skala transport.

Preface

This Ph.D. thesis is the result of research conducted during my time as a Ph.D. student at the technical University of Denmark (DTU) in the period from August 1st 2010 to October 31st 2013. The research was carried out under supervision of professor Peter Uhd Jepsen, head of the Terahertz Technologies and Biophotonics Group at DTU Fotonik, and associate professor Peter Bøggild, head of the Nanocarbon Group at DTU Nanotech.

All terahertz time-domain spectroscopy results presented in the thesis were obtained at DTU Fotonik, Department of Photonics engineering. Raman spectroscopy measurements were performed at DTU Nanotech, Department of Micro- and Nanotechnology. Silicon microfabrication was performed at the cleanroom facility, DTU Danchip.

The micro four-point probe measurements presented in the thesis were obtained by senior scientist Dirch Hjorth Petersen at DTU Nanotech and Capres A/S. The CVD graphene samples presented in chapter 4 were prepared by Ph.D. student Filippo Pizzocchero at DTU Nanotech, Ph.D. student Eric Whiteway and associate professor Michael Hilke at McGill University, Montreal, Quebec, Canada, and Alba Centeno and Dr. Amaia Zurutuza at Graphenea S.A., Donostia-San Sebastian, Spain. The CVD graphene samples presented in chapter 5 were prepared by assistant professor Jie Sun at the Quantum Device Physics Laboratory, Chalmers University of Technology, Gothenburg, Sweden. The CVD graphene samples presented in chapter 6 were prepared by Ph.D. student Filippo Pizzocchero at DTU Nanotech.

This Ph.D. project was partially financed by DTU Fotonik (2/3) and DTU Nanotech (1/3). I have received financial support for an external research stay in Kyoto, Japan from Valdemar Selmer Tranes Fond, Augustinus Fonden and Otto Mønsteds Fond. Financial support was given for laboratory equipment and travel expenses by Augustinus Fonden, Oticon Fonden and Taumoses Fond.

Jonas Christian Due Buron
Kongens Lyngby, October 31st 2013

Acknowledgements

There is a long list of people that I am grateful to have had the pleasure of knowing and working with during my Ph.D. project, without whom it is likely that this thesis would never have come to be.

I would first of all like to thank my two supervisors, Prof. Peter Uhd Jepsen and Prof. Peter Bøggild, for their supervision and guidance throughout the past 5 years. I am extremely grateful to have been introduced to the world of academic research by two people who, each in their own way, wield a contagious passion and fervor for everything they undertake in their research, and yet equally appreciate the importance of unwinding with aspects of life not related to scientific endeavors. Not rarely in the vicinity of a bar counter. I am certain that I would not have found myself in academia today, had I not crossed paths with supervisors that I appreciate and relate to on a personal level as much as Peter and Peter.

I am very thankful to Dr. David Cooke, who has been a true inspiration for me and who shaped me and my research in graphene terahertz dynamics from the first encounter in an under-graduate course at DTU. He is a remarkable experimentalist and scientist who showed me the ropes in an optics lab, and always challenged me with inspiring views and discussions in the lab. I hope his lab stool still manages to make appearances in the terahertz labs at McGill University.

I want to thank Dr. Dirch Hjorth Petersen, who has been a source of constant frustration in the best possible way. As long as I have known Dirch he has kept me on my toes, by exerting his god-given talent for, most often completely justified, scrutinizing the validity of scientific results. Always with a good sense of humor. There is no doubt i have benefited greatly both scientifically and personally from knowing and working with Dirch.

I have been lucky to work closely with fellow Ph.D. student Filippo Pizzocchero, whose productivity in our collaborations was only surpassed by his flair for physics. Thanks for the always interesting collaborations and discussions. I hope there are a lot more to come.

Though I cannot mention everyone by name, I want to express my thanks to all current and former members of the Terahertz Technologies Group and Nanocarbon Goup for an always inspiring and very enjoyable environment. A special thank you to Dr. Maksim Zalkovskij for fruitful advice and discussions. He was an office mate, lab mate, travel mate, and a good friend throughout the entire project. Also a thank you to fellow Ph.D. student Pernille Klarskov Pedersen for many hours of distractions.

Finally, I want to thank my family and friends for always supporting and helping me, and my friends in Grupo Ginga for always providing a perfect escape from an at times stressful Ph.D. project.

List of acronyms

1D – one-dimensional

2D – two-dimensional

2DEG – two-dimensional electron gas

μ-Raman – micro-Raman

AC – alternating current

AlGaAs – aluminum gallium arsenide

Ar – argon

BHF – buffered hydrofluoric acid

CH_4 – methane

Cu – copper

CVD – chemical vapor deposition

CNP – charge-neutrality-point

CW – continuous wave

DC – direct current

fs – femtosecond (10^{-15} s)

FTIR – fourier transform infrared spectroscopy

FWHM – full width at half maximum

GaAs – gallium arsenide

GHz – gigahertz (10^9 Hz)

HEMT – high electron mobility transistor

HR-Si – high resistivity silicon

HNO_3 – nitric acid

InGaAs – indium gallium arsenide

InP – indium phosphide

ITO – indium tin oxide

LED – light emitting diode

LT-GaAs – low temperature.-grown gallium arsenide

LT-InGaAs – low temperature-grown indium gallium arsenide

M4PP – micro four-point probe

MBE – molecular beam epitaxy

MC – Monte Carlo

MOS – metal-oxide-semiconductor

$(NH_4)_2S_2O_8$ – ammonium persulfate

Nd:YLF – neodymium-doped yttrium lithium fluoride

nm – nanometer (10^{-9} m)

PCS – photoconductive switch

PECVD – plasma-enhanced chemical vapour deposition

PMMA – polymethyl-methacrylate

Poly-C – poly-crystalline

Poly-Si – poly-crystalline silicon

ps – picosecond (10^{-12} s)

QHE – quantum hall effect

r-GO – reduced graphene oxide

RD-SOS – radiation damaged silicon-on-sapphire

RF – radio frequency

S-C – single-crystalline

sccm – standard cubic centimeter

SH – second harmonic

SHG – second harmonic generation

Si – silicon

SiC – silicon carbide

Si_3N_4 – silicon nitride

SiN – silicon nitride

SiO_2 – silicon dioxide

THz – terahertz (10^{12} Hz)

THz-TDS – terahertz time-domain spectroscopy

Ti:Sapphire – titanium-sapphire

UHV – ultra-high vacuum

Å – angstrom (10^{-10} m)

List of Figures

Figure 1.1: Transmittance and sheet resistance data for graphene films appearing in the literature along with the industry standard defined by ITO. These are broken down into films prepared by CVD, or from reduced graphene oxide or chemically modified graphene, pristine exfoliated graphene, or chemically synthesized graphene. The star represents the minimum industry requirement, corresponding to σ_{DC}/σ_{Op}=35. The dashed line indicates all points corresponding to this ratio. The full line corresponds to a calculated case of highly doped graphene layers. Reprinted[5] .. 3

Figure 1.2: Complexity and feature sizes in integrated circuitry has followed Gordon Moore statement from 1965, also known as'Moore's law', that transistor counts would double every 18-24 months. Reprinted[7] 4

Table 1: Carrier mobility for typical semiconducting materials. 5

Figure 1.3: Allotropes of hexagonal carbon. Schematic showing how the atomic structure of graphene relates to other allotropes of hexagonal carbon. Reprinted[15] ... 5

Figure 2.1 : The hexagonal graphene crystal structure is constructed by a triangular Bravais lattice with a two-atom structure within each unit cell, marked in dashed line. On the right the corresponding Brillouin zone is shown. The band structure of graphene can be calculated based on a tight-binding nearest-neighbor-hopping approximation. The hopping potential between neighboring atoms is $V_{pp\pi}$=-2.8 eV11

Figure 2.2 : (a) Energy-momentum dispersion for graphene obtained from nearest-neighbour tight-binding approximation in equation (2.4). Reprinted[18]. (b) Band diagram for graphene. Reprinted[20]. 13

Figure 2.3 : Raman spectra of pristine (top) and defected (bottom) graphene. The main peaks are labelled. Reprinted[23]. 15

Figure 2.4 : (a) Schematic of the sample structure used in the initial work on electric field effect in graphene films. (b) Sheet conductance as a function of back-gate voltage for a micro-mechanically exfoliated monolayer graphene flake at T=10K. The slopes reflect a field effect carrier mobility of around 15,000 cm^2/Vs. Reprinted[2]. (c) Hall measurements of carrier density and Hall mobility as a function of back-gate voltage at T=1.7K. Reprinted[3] 17

Figure 2.5 : Sheet carrier density calculated from the full expression in equation (2.7) (red lines) and approximate expression where the quantum capacitance, expressed in the second term on the right-hand-side is neglected (black lines), for (a) 5 Å SiO_2 gate dielectric and (b) 50 nm SiO_2 gate dielectric.................................... 18

Figure 2.6 : (a) The minimum conductivity and metallic-regime-mobility (mL) for 19 different graphene devices measured at 1.6 K. Filled symbols indicate two devices made from the same graphene flake, as shown in the inset. Reprinted[32] (b) Colour map of the spatial carrier density variations in a graphene flake, extracted from surface potential measurements. The blue regions correspond to holes and the red regions to electrons. Reprinted[33]. (c) Histogram of the density fluctuations in (b). Reprinted[33] 19

Figure 2.7 : The mobility progress achieved at Bell Labs for GaAs 2DEGs over the last three decades, leading up to the present mobility record of 36.000.000 cm^2/Vs. The curve labelled 'bulk' is for GaAs single crystal doped with the same concentration of electrons as the 2DEGs. MBE: molecular-beam epitaxy; LN2: liquid nitrogen; 'undoped setback': and undoped layer prior to the modulation doping to further separate the ionized impurities from the 2DEG. Reprinted[39]. 21

Figure 2.8 : (a) The conductivity vs. gate voltage for a pristine graphene film (black) and three different potassium doping concentrations (blue, purple, red) taken at 20K in ultra high vacuum. Reprinted[36] (b)The conductivity vs. gate voltage of five different graphene samples with different levels of disorder. For clarity, the curves are vertically displaced. The horizontal dashed lines indicate the zero conductance for each curve. Dotted curves are fits to a Boltzmann transport model for charged impurity scattering, taking into account the effect of impurity density on the slope, minimum conductivity position and width as well as minimum conductivity value. The inset shows a detailed view of the density-dependent conductivity near the CNP. Reprinted[32]. (c) Resistivity r (blue curve) and conductivity s=1/r (green curve) as a function of gate voltage. When a density-independent resistivity contribution from short-ranged scattering is subtracted, the conductivity due to long-range charged impurity scattering, linear with V_g, is recovered. Reprinted[21]. 23

Figure 2.9 : Drude-Smith conductivity normalized to the Drude weight for scattering time $\tau = 50$ fs and back-scattering parameter c ranging from 0 til -1. Full lines are the real part of the conductivity and dashed lines are the imaginary part of the conductivity. Based on equations (2.25) and (2.26).. 31

Figure 2.10 : A direct impact of the phenomenological inclusion of back-scattering in the Drude-Smith model can be seen in the impulse current response function, here plotted for three different values of *c*. In the Drude-case (*c*=0) the current falls monotonically to zero as an exponential decay, while the current actually goes negative for negative values of c, directly reflecting back-scattering. Reprinted[65] .. 32

Figure 3.1: The electromagnetic spectrum. The THz frequency region, or "THz gap", is situated between microwaves and infrared regions.................................... 35

Figure 3.2: Schematic of the components in the Picometrix© T-ray™ commercial fiber-coupled terahertz time-domain spectrometer. Alongside is shown a photograph of the THz spectrometer along with a laptop running the control software (www.picometrix.com). 37

Figure 3.3: Schematic layout of traditional photoconductive switches. (a) Front view of a PCS showing the metallic electrode and photoconductive gap forming the Hertzian dipole antenna responsible for THz emission. (b) Side view showing the HR-Si substrate lens used to collect and collimate the highly diverging THz radiation emerging from the Hertzian dipole point-source. (c) Top view showing the configurational scheme for THz generation in a PCS. (d) Top view showing the coniguratonal scheme for THz detection in a PCS. 38

Figure 3.4: Transient sheet photoconductivity of a detector system with τ_c=500 fs, τ_s=30 fs and an optical pulse FWHM of 132.8 fs. (a) time-domain representation (b) frequency-domain representation. The dashed line indicates the response function of the detector when diffraction effects are included. Reprinted[98] 40

Figure 3.5: (a) Terahertz time-domain waveform recorded with the Picometrx© T-ray™ 4000 system using 22mm thick aspheric poly-ethylene lenses with a working distance of 25.4 mm. (b) Fourier transform of the THz transient in (a). 41

Figure 3.6: (a) FWHM as a function of frequency for the Picometrix© T-ray™ 4000 system using aspheric poly-ethylene with a working distance of 25.4 mm. Data is obtained by scanning the focused THz beam across the edge of a very straight and highly uniform CVD graphene film. (b) THz image formation in the Picometrix© T-ray™ 4000 is carried out by raster scanning the sample in the focal plane between THz emitter and detector equipped with aspheric poly-ethylene lenses with working distance of 25.4mm. Full THz time-domain waveforms are recorded in each pixel of an image. 42

Figure 3.7: Schematic of experimental setup for generation of free-space THz transients from a two-color laser induced air plasma. 44

Figure 3.8: Schematic of experimental setup for air-biased coherent detection of THz transients. 45

Figure 3.9: Schematic of experimental setup for ultra-broadband THz-TDS by two-color plasma THz generation and air-biased coherent detection. 46

Figure 3.10: THz waveforms recorded in the THz air photonics spectrometer provide bandwidth from 1 to up to 30 THz. (a) time-domain THz waveform recorded with a temporal resolution of 10 fs. Inset shows the full temporal trace from 0 to 3 ps (b) Fourier transform of the temporal waveform in (a) shows bandwidth from approximately 1-30 THz.. 47

Figure 3.11: Spitfire Pro Ti:Sapphire regenerative amplifier system from Spectra-physics. Reprinted[118] 48

Figure 3.12: The THz response of the conducting thin film is isolated in the complex-valued transmission function, T_{film}, as the sample Fourier transform divided by the reference Fourier transform. 50

Figure 3.13: The transmitted THz field are given by a combination of transmission, reflection and propagation coefficients for each of the temporally separated echoes, caused by multiple internal reflections. 51

Table 2: Transmission and reflection coefficients at normal incidence for boundaries formed between air and a bulk, continuous medium. 52

Figure 4.1: Monolayer graphene films exhibit an extraordinarily large THz response due to an exceptionally high conductance. A single atomic layer of CVD graphene is sufficient to reduce the amplitude of transmitted THz pulses by up to 20% as shown for (a) time-domain, and (b) frequency-domain. 55

Figure 4.2: (a) Schematic of the sample structure. CVD graphene grown on single-crystalline Cu (111), transferred to HR-Si wafer with 300 nm SiO_2 layer. (b) Optical microscopy image of the CVD graphene grown on single-crystalline Cu after transfer onto oxidized HR-Si wafer. (c) Optical microscopy image of the CVD graphene grown on poly-crystalline Cu after transfer onto oxidized HR-Si wafer. Scale bars are 2 mm. 58

Figure 4.3: Sample and reference THz time-domain waveforms for CVD graphene films grown on (a) single-crystalline Cu (111) substrate (b) poly-crystalline Cu foil. Resulting sheet conductance spectra for (c) single-crystalline Cu (111) substrate (d) poly-crystalline Cu foil. 59

Figure 4.4: Secondary electron micrograph of a micro four-point probe. Reprinted[135] 62

Figure 4.5: Illustration of the 3 independent configurations of contacts for current injection and contacts for probing potential difference without presence of a magnetic field. 63

Figure 4.6: Example of the measurement outcome in a dual configuration M4PP sheet resistance measurement. As indicated, the ratio between resistances obtained in the A and B configurations is nominally 1.26 for an infinite, uniformly conducting sheet. 64

Figure 4.7: (a) Optical micrograph of the CVD graphene film grown on single-crystalline Cu (111). The dashed line indicates the line along which the sheet conductance was mapped by THz-TDS and dual configuration M4PP sheet resistance line scan measurement. (b) M4PP and THz-TDS DC-extrapolated sheet conductance as a function of position along the dashed line in (a). 65

Figure 4.8: (a) Sheet conductance measured by THz-TDS and M4PP with 4, 8, 12, 50, and 100 μm probe pitch as a function of positions. (b) M4PP sheet conductance for various probe pitches plotted against THz-TDS sheet conductance shows an almost perfect 1:1 correlation. The full red line indicates a 1:1 correlation............ 66

Figure 4.9: (a) Indications of the randomized M4PP sheet conductance measurement locations on the poly-C Cu foil graphene film. (b) Correlation plot showing measured M4PP sheet conductance as a function of measured THz-TDS sheet conductance in the locations on the graphene films indicated in (a). The full red line indicates a 1:1 correlation. 67

Figure 4.10: The substrate thickness of a 1mm thick HR-Si wafer was mapped with 100 μm step size in an 11.4x11.4 mm^2 area. The substrate thickness was obtained in each pixel of the map by a fitting routine. On the right an example of the outcome of one such fitting procedure is shown... 69

Figure 4.11: Sample and reference THz time-domain waveforms for CVD graphene films grown on (a) single-crystalline Cu (111) substrate (b) poly-crystalline Cu foil. Resulting sheet conductance spectra for (c) single-crystalline Cu (111) substrate (d) poly-crystalline Cu foil. 70

Figure 4.12: (a) Tiled optical microscopy image and (b) THz sheet conductance map of CVD graphene film grown on single-crystalline Cu (111) substrate (average sheet conductance in band from 0.9-1.0 THz). 74

Figure 4.13: (a) Optical microscopy image and (b) THz sheet conductance map of a 4 inch circular CVD graphene film grown on a high purity Cu film sputtered onto a 4 inch Si/SiO$_2$ wafer. Transferred to HR-Si wafer by electrochemical transfer technique. Average sheet conductance in band from 0.9-1.0 THz. (c) THz sheet conductance map of a 6x4 cm^2 CVD graphene film grown on Cu foil. Transferred to HR-Si by sacrificial etching of Cu foil. Average sheet conductance in band from 0.9-1.0 THz. (graphene film is courtesy of Graphenea Inc.) (d) THz sheet conductance map of a 4 inch circular CVD graphene film grown on Cu foil. Transferred to HR-Si by sacrificial etching of Cu foil. Average sheet conductance in band from 0.9-1.0 THz. (graphene film is courtesy of Graphenea Inc.) 76

Figure 5.1: Combined THz-TDS, M4PP, Raman and optical mapping of large area graphene on SiO2-on-Si substrate. Sketch depicting the principle of parallel mapping of electrical conductance, Raman response and optical absorption on a single-layer large area graphene film by THz-TDS, M4PP, μ-Raman and optical microscopy. Bottom panel shows the relevant length scales of the physical processes probed by each techniques. The combined information of these techniques facilitates determination of electrical uniformity on nanometer and micrometer length scales and correlation of electrical features to Raman and structural features. The sketch is based on actual data maps. 81

Figure 5.2: Representative Raman spectra for the two investigated CVD graphene samples. 84

Figure 5.3: Example of THz-TDS time-domain data showing multiple echoes from partial internal reflections in the SiO2-on-Si sample substrate. Sheet conductance extraction is based on the Fourier transform (FFT amplitude shown in inset) of the time-windowed 2nd transmitted pulse, E2 (indicated by gray shading), for areas with (black line) and without (red line) graphene on the surface of the wafer. 85

Figure 5.4: (a) Spectrally resolved sheet conductance of the two graphene films, measured by THz-TDS. Characteristic length scales are based on an estimated diffusion constant of D = 66 cm^2/s. Triangles represent Re(σ_s) and circles represent Im(σ_s). The spectra are obtained in the center of Figure 5.5(a) (sample 1, light grey) and in the central conducting part of Figure 5.7(b) (sample 2, black). The full red lines indicate the average real sheet conductances of the two samples, while the dashed red lines indicates the zero-value of the negligible imaginary sheet conductances of the two samples. The observed drop in THz sheet conductance at the low end of the spectrum for sample 2 is caused by the low frequency parts of the THz spot extending outside the area with uniform graphene coverage, as indicated in the inset, and the small peak observed at 1.1 THz in Re(σ_s) is an artifact caused by the water vapour absorption line of ambient air. The indicated characteristic length scale is discussed in the text. (b) Measured FWHM of the THz beam as a function of frequency. 87

Figure 5.5: Images of homogeneous CVD grown graphene film on 90 nm SiO2 on Si (sample 1). Scale bars are 2 mm. (a) THz sheet conductance map. Average sheet conductance in 1.3-1.4 THz band. (b) Tiled optical microscope image. 88

Figure 5.6: μ-Raman maps of homogeneous CVD grown graphene film on 90 nm SiO2 on Si (sample 1). Scale bars are 2 mm. (a) D peak height (b) G peak height (c) 2D peak height (d) D peak spectral position (e) G peak spectral position (f) 2D peak spectral position (g) G/D peak amplitude ratio (h) 2D/G peak amplitude ratio. 89

Figure 5.7: Images of a damaged CVD graphene film on 90 nm SiO2 on Si. Scale bars are 2mm. (a) Tiled optical microscope image, (b) THz sheet conductance image (1.3-1.4 THz), (c) M4PP sheet conductance map, (d) M4PP sheet conductance map convoluted with a 2D Gaussian profile of FWHM=0.32mm. 91

Figure 5.8: μ-Raman maps of inhomogeneous CVD grown graphene film on 90 nm SiO2 on Si (sample 2). Scale bars are 2 mm. (a) D peak height (b) G peak height (c) 2D peak height (d) D peak spectral position (e) G peak spectral position (f) 2D peak spectral position. 91

Figure 5.9: THz/M4PP correlation analysis. (a) Correlation diagram of THz and M4PP sheet conductance measurements for sample 1(dark gray triangles) and sample 2(light gray, blue and red circles). The full black line indicates 1:1 correlation. (b) Sample map showing pixel positions of correlation data for sample 2. In (a) and (b), the data subset with $\Gamma = \sigma_{s,M4PP}/\ \sigma_{s,THz} > 1.1$ is plotted as red dots and the data subset with $\Gamma = \sigma_{s,M4PP}/\ \sigma_{s,THz} < 0.4$ is plotted as blue dots. The red dots tend to cluster near the edges of the sample, while the blue dots dominate areas with large holes and other distinct visible transfer damages. 93

Figure 5.10: Distribution of measured resistance ratio R_A/R_B in the dual configuration M4PP map shown in Figure 5.7(c) (turquoise bars), Monte Carlo simulation of R_A/R_B distribution for an infinite, continuous conducting sheet with 500 nm normal distributed electrode position errors (dashed, black line) and running average of the measured dual configuration sheet conductance as a function of R_A/R_B (full, orange curve). 94

Figure 5.11: M4PP dual configuration sheet conductance and R_A/R_B values for different electrode pitches and positions along two line-scans in a highly conducting region and a poorly conducting region on 'sample 2'. The data is recorded with a 12 point probe, facilitating 7 different equidistant M4PP configurations, in 6 engages with 5 µm spacing. 95

Figure 5.12: average M4PP dual configuration sheet conductance of 6 engages as a function of electrode pitch for a highly conducting region and a poorly conducting region on 'sample 2' 95

Figure 6.1: SEM micrograph of graphene Hall bar device and gate-sweep measurement showing dependence of graphene sheet conductance on back-gate voltage. Graphene film is separated from a highly doped Si wafer by a 300 nm thick SiO_2 layer. Reprinted[2] 102

Figure 6.2: Back-gated CVD graphene THz-TDS conductance maps. Fermi level is controlled during THz-TDS conductance mapping by applying a DC voltage between CVD graphene film and a semi-transparent n-type silicon substrate (1.6 Ω-cm) separated by a 300 nm SiO_2 film 104

Figure 6.3: Silicon-dielectric-graphene capacitor structure where the silicon substrate is in (a) accumulation and (b) depletion. 105

Figure 6.4: a) Schematic of sample consisting of large-area monolayer CVD graphene film residing on layered substrate comprising 525 mm HR-Si, 50 nm boron-doped poly-crystalline silicon with n ≈ 10^{18} cm-3, and 300 nm Si3N4. Au contacts are used for contacting the graphene film and the poly-crystalline silicon film. (b) Time-domain waveforms of THz pulses transmitted through a bare HR-Si substrate and a layered HR-Si/poly-Si/Si3N4 substrate (c) Amplitude transmission coefficient and phase-shift for poly-Si and Si3N4 films. The THz response of the thin films is found to be negligible.. 107

Figure 6.5: Outline of the design and fabrication of substrates for quantitative extraction of carrier mobility from THz-TDS measurement. Based on poly-crystalline silicon thin film back-gate and plasma-enhanced chemical vapour deposited Si_3N_4 gate dielectric 109

Figure 6.6: (a) Raster images showing the transmitted THz power at different gate voltages. The THz power scale has been compressed to highlight the contrast of the graphene film. White scale bars are 5 mm. (b) Frequency-dependent, gate-induced sheet conductance of the graphene film in the central region at series of different gate voltages. Left: real part of the sheet conductance. Right: imaginary part of the sheet conductance. The features around 1.15 THz are artifacts due to residual atmospheric water vapour absorption. 111

Figure 6.7: Sheet conductance images represented by the average, real sheet conductance value from 0.5-0.9 THz.. 113

Figure 6.8: (a) Average, real, gate-induced sheet conductance from 0.5 to 0.9 THz as a function of Vg for 3 distinct positions of the mapped area. Circles, triangles and squares are experimental data and the full lines are linear fits to the data for Vg from -25V to +20V. (b) Map showing the spatial distribution of field effect mobility across the CVD graphene film evaluated at 0.5-0.9 THz...................................... 114

Contents

Abstract .... **i**

Resume .... **v**

Preface .... **ix**

Acknowledgements .... **xi**

List of acronyms .... **xv**

List of Figures .... **xvii**

1 Introduction **1**

- 1.1 Graphene for transparent electrodes in displays and photovoltaics 2
- 1.2 Graphene applications in high-speed electronics 4
- 1.3 Scope of this thesis 6

2 Graphene electronic properties **11**

- 2.1 Linear energy dispersion and massless charge carriers 14
- 2.2 Raman spectroscopy of graphene 15
- 2.3 Electric field effect, minimum conductance and charge puddles 16
- 2.4 High mobility monolayer crystals and the scattering mechanisms in graphene… 20
- 2.5 The Drude model 24
- 2.6 Defects in large-scale graphene 26
  - 2.6.1 Liquid-phase exfoliation 27
  - 2.6.2 Epitaxial growth on SiC 27
  - 2.6.3 Chemical vapor deposition on metal catalysts 28
  - 2.6.4 Extended defects in large-area graphene 28
- 2.7 The Drude-Smith Model 29

3 Terahertz time-domain conductance spectroscopy **35**

- 3.1 Picometrix T-ray 4000 fiber-coupled terahertz time-domain spectrometer & imaging system 36
- 3.2 Ultra-broadband terahertz time-domain spectroscopy based on THz air photonics 42
  - 3.2.1 THz pulse generation in a two-color laser-induced air plasma 43
  - 3.2.2 Air-biased coherent detection of THz pulses 44
  - 3.2.3 THz air photonics spectrometer 46
  - 3.2.4 Spectra-physics Spitfire Pro Ti:Sapphire regenerative amplifier system……………. 48
- 3.3 Fresnel equations & THz thin film conductance 49

4 Study 1: Broadband terahertz time-domain conductance spectroscopy and imaging of graphene films **55**

- 4.1 Complex conductance of CVD graphene at 0.15 to 1.5 THz 57

4.2 Experimental comparison between non-contact THz-TDS and contact-based M4PP conductance measurements 61

4.2.1 Micro four-point probes 62

4.2.2 THz-TDS vs M4PP conductance: S-C Cu (111) graphene film 64

4.2.3 THz-TDS vs M4PP conductance: poly-C Cu foil graphene film 67

4.3 Carrier nano-localization and preferential back-scattering: Ultra-broadband THz conductance spectroscopy of CVD graphene at 1 to 15 THz 68

4.4 Wafer-scale graphene conductance mapping by THz-TDS imaging 74

5 Study 2: THz and M4PP large area conductance mapping and correlation – a new light on defects 79

5.1 Corrections 79

5.2 Introduction 80

5.3 Experimental details 83

5.4 AC and DC graphene conductance mapping 86

5.5 New light on electrical defects: Correlating THz and DC conductivity 92

5.6 Conclusions 97

6 Study 3: Gated THz conductance mapping for non-contact graphene mobility mapping 101

6.1 THz conductance mapping of back-gated graphene: Low-doped silicon back-gate 103

6.2 Quantitative large-area mapping of carrier mobility in graphene: Highly doped poly-silicon back-gate 106

6.2.1 Method 106

6.2.2 Substrate fabrication 108

6.2.3 Results and Discussion 110

6.2.4 Conclusion 115

7 Conclusions 119

8 Bibliography 123

8.1 List of references 123

8.2 List of Publications 141

8.2.1 Peer reviewed Journal publications 141

8.2.2 Conference Proceedings 141

8.2.3 Conference contributions 142

8.2.4 Patent applications 144

1 Introduction

After its first isolation in 2004[1], the atomically thin carbon crystal known as graphene has offered itself as a very promising candidate for numerous electronic applications. Due to the monatomic thickness and unique electronic spectrum of graphene, resulting in quasi-relativistic charge carrier transport, the thin carbon film offers a suite of extremely favorable properties, including record-breaking electrical conductivity and mobility, high optical transparency and extreme mechanical strength and flexibility. This is a combination of attributes never before found in a single material system. Thus, in addition to having provided the scientific community with access to quantum-relativistic phenomena in table-top experiments on a solid-state system[2,3], graphene shows a very large potential for usage in commercial applications.

In particular, graphene looks promising as a sustainable and performance-superior replacement for a range of scarce rare-earth materials that are used widely in the electronics and photo-voltaics industry today. Consumer electronics in the form of e.g. smartphones, laptops, tablets, flat panels and even different forms of wearable electronics have never been produced at a higher rate than they are today. Since more and more of these applications include touch-screens, flat panels and high-frequency electronics for wireless communication purposes, which all utilize ecologically unfriendly and rare materials such as e.g. indium, gallium and germanium, the high production rates put a critical pressure on the global supply and reserves of such materials[4] – a phenomenon that has already lead to international disputes and worker exploitation through black markets.

Graphene, which consists of one of the most abundant elements on earth, possesses properties that potentially allows it to replace indium-tin-oxide in its use as transparent electrode in the growing markets of flat panels, touch-screens and solar panels. It also holds electronic properties that may allow the replacement of gallium-arsenide/aluminum-gallium-arsenide/indium-gallium-arsenide (GaAs/AlGaAs/InGaAs) as well as silicon-germanium (SiGe) alloys in high-electron-mobility transistors (HEMT) used in the radio-frequency circuits of e.g. cell phones for wireless communication approaching terahertz carrier frequencies. In addition to having relevance in conventional electronic applications, graphene is expected to offer access to a new suite of novel electronic applications such as for instance transparent and flexible electronics and photo-voltaics, facilitated by graphenes unmatched combination of flexibility, durability and transparency.

1.1 Graphene for transparent electrodes in displays and photovoltaics

At present time the demand and production of consumer-grade flat panels, touch screens and light-emitting diodes (LED) as well as solar panels for green energy production is at an all-time high. A vital component within this family of devices is a transparent conducting film, commonly known as a transparent electrode, which allows the passage of light while enabling electrical contact to individual pixels in flat panel and touch screen displays, or enables collection of free electrons and holes generated by photon absorption in a solar cell. The most important requirements for transparent electrodes are the optical transparency in the visible region of the electromagnetic spectrum and the electrical sheet conductance, which should both be as high as possible. At present, the most widespread material platform for transparent electrodes is indium-tin-oxides (ITO). The continued use of ITO is however threatened by highly limited global supplies of indium in the face of an ever increasing demand[5,6]. The composition of indium, tin and oxygen in ITO films means that indium composes nearly 75% of the mass of an ITO film, resulting in around ¾ of the currently produced indium being consumed for ITO applications[6]. To enable continuation of the current development of solar panels, LEDs and flat panel and touchscreen displays, it will be necessary to find a replacement material for ITO, which is also used in increasing amounts in photonics applications for telecommunication purposes. Commercially available ITO films provide sheet conductances between 10Ω and 100Ω at optical transmittances of 85%-90%, which sets the industry standards that an alternative material candidate should meet for commercial implementation[5], as indicated in Figure 1.1.

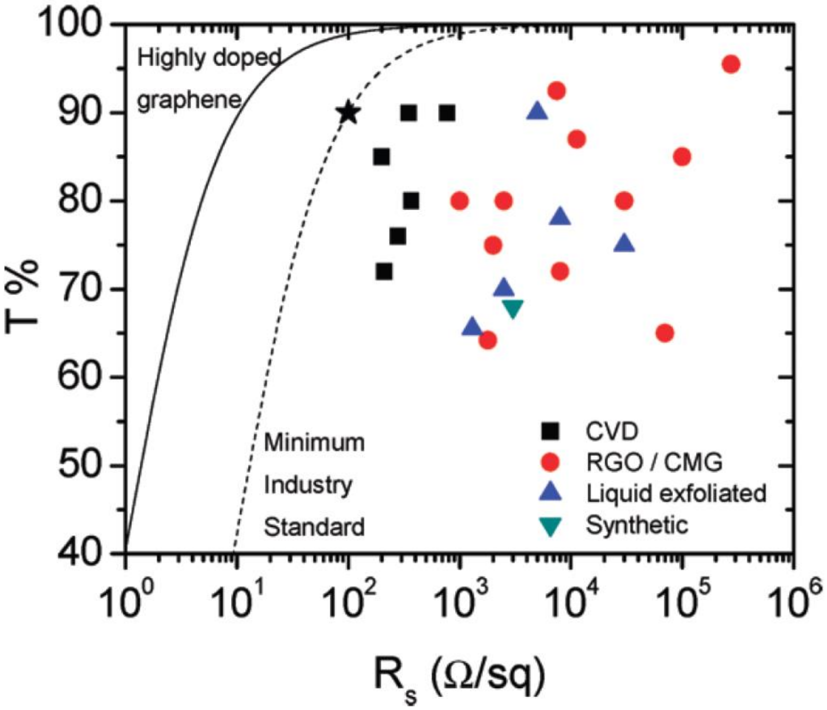

Figure 1.1: Transmittance and sheet resistance data for graphene films appearing in the literature along with the industry standard defined by ITO. These are broken down into films prepared by CVD, or from reduced graphene oxide or chemically modified graphene, pristine exfoliated graphene, or chemically synthesized graphene. The star represents the minimum industry requirement, corresponding to σ_{DC}/σ_{Op}=35. The dashed line indicates all points corresponding to this ratio. The full line corresponds to a calculated case of highly doped graphene layers. Reprinted[5]

Due to its atomic thickness and highly mobile charge carriers, graphene combines high optical transparency with relatively high sheet conductance, which has spurred interest in graphene as a candidate for future transparent electrode films. As shown in Figure 1.1, graphene has shown combinations of sheet conductance and optical transmittance that approaches that obtainable in ITO films, with graphene grown by chemical vapor deposition (CVD) techniques showing the best results. Reported results are however highly dependent on the specific fabrication process as well as the specific investigation, illustrating that the technology at this point is far from a mature state and that further process optimizations are needed. In addition, graphene is able to address some of the fundamental drawbacks of ITO films relating to mechanical fragility and long term degradation. ITO is a very brittle material and is therefore prone to damage from mechanical straining. It is therefore not compatible with applications that require mechanical flexibility, and its electrical properties are shown to degrade in long term cyclic testing due to formation of micro-cracks already at 2-3% mechanical strain[6]. Due to its high mechanical strength and flexibility, graphene may therefore facilitate development of innovative devices such as flexible solar panels and flexible displays.

1.2 *Graphene applications in high-speed electronics*

As formulated and foreseen by Gordon Moore in 1965, the electronics industry has achieved a mind staggering evolution in the computing power of integrated circuits over the course of the last 4 decades. He foresaw that the number of transistors pr. unit area in integrated circuits would double every 18-24 months (known as Moore's law).

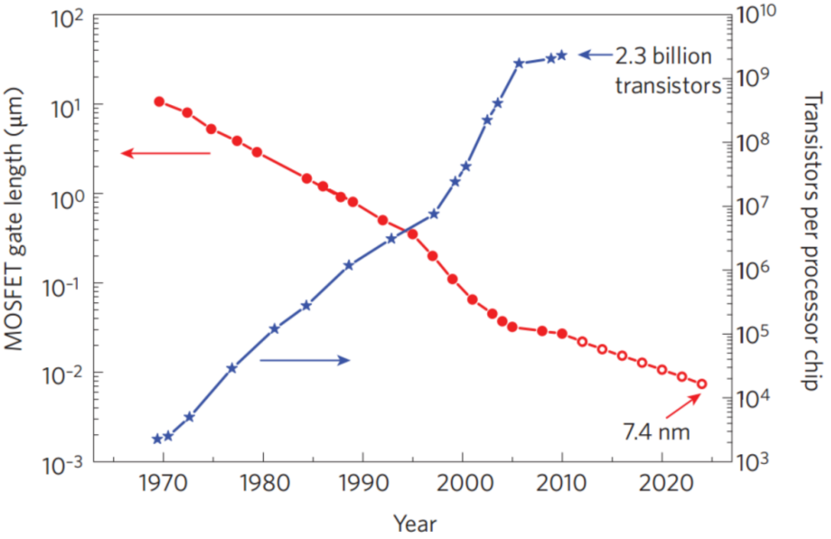

Figure 1.2: Complexity and feature sizes in integrated circuitry has followed Gordon Moore statement from 1965, also known as'Moore's law', that transistor counts would double every 18-24 months. Reprinted[7]

We have since witnessed the fulfillment of Gordon Moore's prediction, as shown in Figure 1.2, accompanied by a continuous increase in the switching speed of integrated circuits facilitated mainly by decreasing transistor gate lengths. The result has been a tremendous escalation in the computing power available from integrated electronics. Moore's law was effectuated by the impressive advances in silicon processing technology, which have yielded some of the most complex structures ever created by mankind.

Material	**Electron (hole) mobility [cm^2/Vs]**
Silicon	1,400 (450) [8]
Germanium	3,900 (1,900) [9,10]
GaAs	8,500 (400) [11]
InAs	40,000 (500) [12]
Carbon nanotubes	Up to 100,000 [13]
Graphene	Up to 500,000 [14]

Table 1: Carrier mobility for typical semiconducting materials.

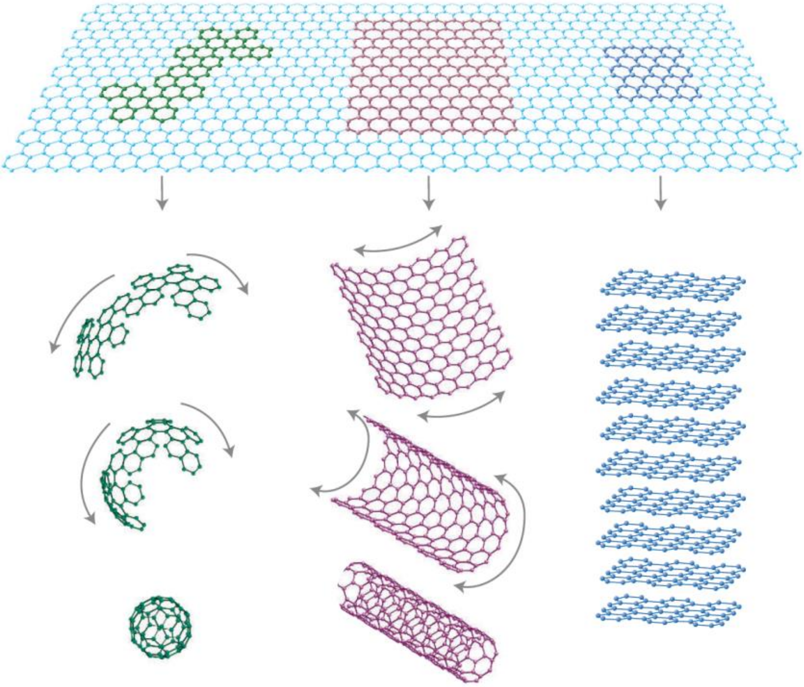

Figure 1.3: Allotropes of hexagonal carbon. Schematic showing how the atomic structure of graphene relates to other allotropes of hexagonal carbon. Reprinted[15]

However, realization of the silicon-based devices with transistor dimensions of single-digit nanometers that are projected for the near future is a steep challenge that has yet to be faced. In addition, the silicon technology has seen a stagnation in the switching speed of integrated circuits over the last 5 years, mainly because of the high power consumption penalty associated with pushing silicon-based transistors to greater speeds. These issues have initiated substantial research efforts into alternative materials that can provide smaller structures or higher switching speeds. Some of the considered candidates are listed in Table 1.

Graphene has lately emerged as a possible candidate for facilitating both transistor downscaling and increased switching speeds. Graphene is a single layer of carbon atoms arranged in a hexagonal crystal lattice, as shown in Figure 1.3, and in its intrinsic form is a zero-bandgap, high mobility semiconductor. The single-atomic thickness of the crystal offers unprecedented potential for scaling devices to the extreme nanoscopic limit, and a record high room temperature carrier mobility of up to 500,000 cm^2/Vs [14] holds promise for pushing transistor switching speeds to new heights. This combination of features suggests graphene as a possible successor to silicon for realization of next generation planar electronics. Furthermore, graphene may offer the exciting and entirely new perspective of high-performance, flexible and transparent electronics due to its high mechanical flexibility, strength and durability.

1.3 Scope of this thesis

Quite substantial progress is already seen at a research level in terms of the large-scale synthesis of graphene that is necessary for practical implementation of in the above-mentioned commercial contexts. However promising, synthesized graphene in general shows huge variations in electronic quality, highlighting a need for electronic characterization on a large scale for further development of the material towards a position as a real alternative for electronic applications. In spite of very impressive advances in the available processes for large-scale synthesis, however, development of techniques targeting such electronic characterization of graphene on a large scale has not kept pace. This essentially leaves the rapidly progressing research field with inadequate means of assessing electronic quality and uniformity on a large scale.

The work presented in this thesis attempts to address this issue by applying the emerging technique known as terahertz time-domain spectroscopy (THz-TDS) as a high-throughput, non-contact probe of the electronic properties of large-area graphene. In addition to accurate and direct observation of fundamental transport properties as well as carrier dynamics at terahertz frequencies, it is shown that THz-TDS can indeed facilitate the rapid and reliable large-scale measurement of electronic properties and their uniformity in large-scale graphene that might be viewed as a vital requirement for industrial implementation of the material.

In chapter 2 the electronic properties of graphene are introduced. In particular, the unusual linear energy dispersion of graphene charge carriers and its consequences for electronic transport in graphene are described. The linear dispersion leads to a range of exotic quantum effects including the half-integer quantum Hall effect (QHE), a non-zero Berry's phase, as well as Klein tunneling, leading to de-localization of carriers at low densities. Perhaps most importantly, the linear dispersion leads to quasi-relativistic behavior of graphene carriers, which are described analogously to Dirac Fermions with zero rest mass. It is argued that in the typically observed diffusive regime dominated by long-range scattering on charged impurities, the carrier momentum relaxation time scales with the square-root of carrier density, while the graphene conductance scales linear with carrier density. On this basis the carrier mobility in graphene is expressed in terms of the carrier relaxation time, readily evaluated in a Drude framework based on broadband THz-TDS experiments. The chapter concludes with a description of the electronic defects specific to large-scale synthesized graphene and their relation to the concept of preferential carrier back-scattering. This phenomenon gives rise to distinct features in the THz conductivity, which is modelled on a phenomenological basis in the Drude-Smith model.

Chapter 3 summarizes the main principles of THz-TDS and provides descriptions of the experimental methods and setups used for conventional and ultra-broadband THz-TDS in this thesis.

Chapter 4 presents an experimental study where the THz conductance response, measured by conventional and ultra-broadband THz-TDS, of large-area graphene grown by CVD on poly-crystalline and single-crystalline copper substrates are compared. Carrier momentum relaxation times are measured directly for both films and used to evaluate the mean free path and carrier mobility. In addition, qualitatively different transport characteristics are found for the two films by ultra-broadband THz-TDS, revealing that preferential carrier back-scattering is significant in the CVD graphene film grown on poly-crystalline copper. Through comparison with DC micro four-point probe conductance measurements it is established by a one-to-one correlation, where $\sigma_{THz-TDS} = \sigma_{M4PP}$, that the conductance measured by THz-TDS in the low frequency limit reflects the DC conductance. Finally, based on this observation, a demonstration of wafer-scale graphene conductance mapping is presented based on THz time-domain spectroscopic imaging.

In chapter 5, the characteristics of electrical defects in cm-scale CVD graphene are investigated by concurrent conductance mapping by THz-TDS and M4PP. It is shown, on a statistical basis of more than 4000 correlated conductance measurements, that the nanoscale transport, probed by THz-TDS, is significantly higher than the micro-scale transport, probed by M4PP. Based on detailed analysis of the results of the two measurement techniques, it is concluded that the film is electrically continuous on the nanoscopic scale, but dominated in its microscopic electronic transport by defects on a ~10 μm scale.

Finally, chapter 6 provides an investigation of the electrically gated THz conductivity in CVD graphene, resulting in a demonstration of large-area graphene field-effect mobility mapping. To isolate the gate-induced conductance of the graphene film from that of the underlying gate electrode, a low-mobility, high carrier density gate material is used. This allows reliable observation of a THz sheet conductance that varies linearly with gate voltage and inherent accurate extraction of graphene field effect mobility and its spatial variation.

2 Graphene electronic properties

Graphene is a monolayer of carbon atoms packed into a two dimensional honeycomb crystal structure as shown in Figure 2.1, which was isolated by micromechanical exfoliation of graphite crystals onto SiO_2 surfaces for the first time in 2004[1,16].

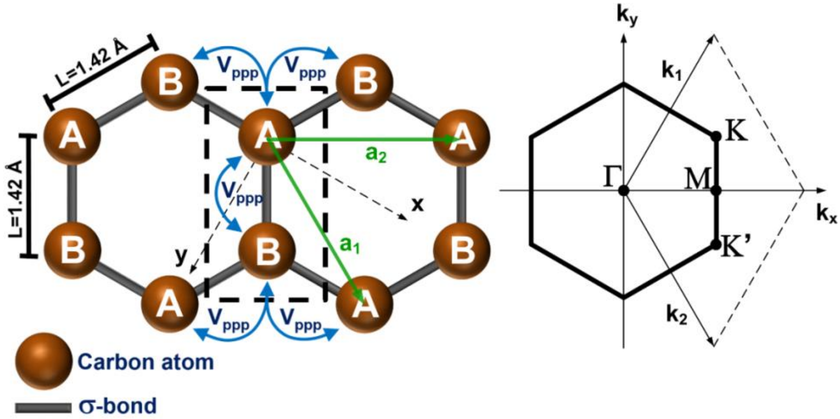

Figure 2.1 : The hexagonal graphene crystal structure is constructed by a triangular Bravais lattice with a two-atom structure within each unit cell, marked in dashed line. On the right the corresponding Brillouin zone is shown. The band structure of graphene can be calculated based on a tight-binding nearest-neighbor-hopping approximation. The hopping potential between neighboring atoms is $V_{pp\pi}$=-2.8 eV

In graphene, hybridization of the 2s, $2p_x$ and $2p_y$ orbitals of the carbon atom lead to formation of three sp^2 orbitals in the crystal plane, leaving one out-of-plane $2p_z$ orbital per carbon atom. Overlapping sp^2 orbitals of neighboring carbon atoms form strong covalent σ-bonds with tightly bounds electrons, whereas delocalized electrons occupy the bonding π and anti-bonding π^* states formed by the overlap of neighboring $2p_z$ orbitals. As shown in Figure 2.1, the honeycomb crystal can be viewed as a triangular Bravais lattice with two atoms per unit cell, constructed from the two lattice vectors

$$\mathbf{a_1} = \frac{a}{2}\left(3,\sqrt{3}\right), \mathbf{a}_2 = \frac{a}{2}\left(3,-\sqrt{3}\right), \tag{2.1}$$

where $a \approx 1.42$ Å is the carbon-carbon distance in graphene .These result in the reciprocal lattice vectors

$$\mathbf{k_1} = \frac{2\pi}{3a}\left(1,\sqrt{3}\right), \mathbf{k_2} = \frac{2\pi}{3a}\left(1,-\sqrt{3}\right), \tag{2.2}$$

defining the first Brillouin zone.

The electronic properties of graphene are largely defined by the behavior of the delocalized electrons in these out-of-plane π-states, since the σ-states are very far away from the Fermi energy and since the overlap between the p_z orbitals and the s, p_x and p_y orbitals is strictly zero by symmetry[17].

A good qualitative description of the electronic band structure of graphene can be obtained from a simple nearest-neighbor, tight-binding calculation, which solely considers the hopping behavior of π-electrons between ‘A’ and ‘B’ sites, as shown in Figure 2.1. Within this π-band approximation, the electronic dispersion relation can be obtained on basis of a relatively simple Hamiltonian, considering the primitive unit cell, containing two atomic sites[18].

$$\hat{H}\left(\mathbf{k}_1,\mathbf{k}_2\right) = V_{pp\pi}\begin{bmatrix} 0 & 1+e^{i\mathbf{k}_1}+e^{i\mathbf{k}_2} \\ 1+e^{-i\mathbf{k}_1}+e^{-i\mathbf{k}_2} & 0 \end{bmatrix}, \tag{2.3}$$

constructed by assuming zero on-site energy and a fixed nearest-neighbor hopping potential $V_{pp\pi}$ (typical values are 2.5-3.1 eV [17–19]) between sites ‘A’ and ‘B’ and applying bloch’s theorem for periodic crystals. By expressing $\mathbf{k}_1$ and $\mathbf{k}_2$ momentum vectors in terms of k_x and k_y and solving for the Eigen-energies of the system, the dispersion relation restricted to nearest-neighbor interactions is obtained as[18]

$$E^{\pm}\left(k_x, k_y\right) = \pm V_{pp\pi}\sqrt{3 + 2\cos\left(\sqrt{3}ak_y\right) + 4\cos\left(\frac{\sqrt{3}a}{2}k_y\right)\cos\left(\frac{3a}{2}k_x\right)}, \quad (2.4)$$

In the resulting band structure, shown in Figure 2.2 in the case where next-nearest neighbor hopping is included, the bonding π states (the negative energy branch, E^-, in equation(2.4)) form a continuous valence energy band, fully occupied by the p_z electrons. The anti-bonding π^* states (the positive energy branch, E^+, in equation(2.4)) similarly form a continuous conduction energy band, which is totally empty.

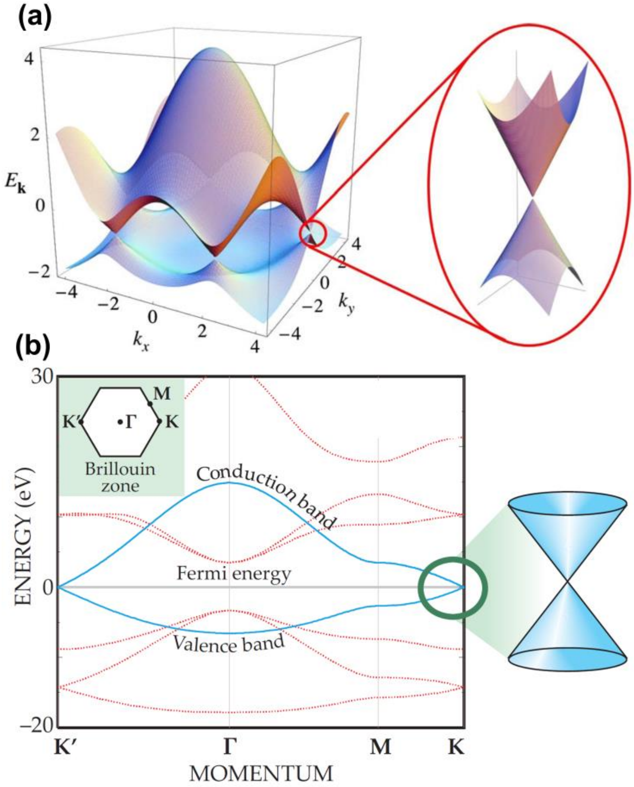

Figure 2.2 : (a) Energy-momentum dispersion for graphene obtained from nearest-neighbour tight-binding approximation in equation (2.4). Reprinted[18]. (b) Band diagram for graphene. Reprinted[20].

The band structure has 2 non-degenerate points, also known as the Dirac or charge-neutrality points K and K'. Here valence and conduction bands touch at the Fermi energy, reducing the Fermi surface to these discrete points and causing what is sometimes referred to as a gapless semiconducting or semi-metallic behavior in graphene.

2.1 Linear energy dispersion and massless charge carriers

One of the most important features of the graphene band structure is the linear dispersion observed in the distinct cone shape close to the K and K' points. Through an expansion around the **K** (or **K'**) vectors, the low energy dispersion can be expressed as[17,18]

$$E^{\pm}(\mathbf{q}) \approx \pm\hbar \mathrm{v_F}\,|\mathbf{q}| + O[(\mathrm{q}/\mathrm{K})^2], \tag{2.5}$$

where $\mathbf{q} = (\mathrm{k_x}, \mathrm{k_y}) - \mathbf{K}$ and $\mathbf{q} \ll \mathbf{K}$, and $\mathrm{v_F}$ is the momentum-independent electronic group velocity or constant Fermi velocity, given by

$$\mathrm{v_F} = \frac{3aV_{pp\pi}}{2\hbar} \approx 10^6\ \mathrm{m/s}. \tag{2.6}$$

For small **q**, corresponding to electron energies close to the Fermi energy, equation (2.5) thus expresses the linear nature of the electronic dispersion. This feature implies that carrier movement in graphene is analogous to that of relativistic particles with zero rest mass, described by Dirac's relativistic equation[19]. This stands in grave contrast with conventional solid-state-systems with parabolic dispersion relations, where carrier transport is fundamentally described by the Schrödinger equation. The consequence of this linear electronic spectrum is a condensed matter system in which the charge carriers move in the crystal with zero effective mass and show many traits of relativistic quantum electrodynamics even at room temperature[2,3]. Graphene charge carriers thus effectively mimic photon behavior with a rest mass equal to zero and a group velocity that is roughly 1/300 of the speed of light, resulting in extraordinarily high mobilities and ballistic transport across micrometer distances at room temperature[2,14,21].

Amongst the distinctive phenomena arising from the quasi-relativistic nature of the Dirac fermions in graphene are measured effective carrier masses as low as $0.007m_e$ when approaching the charge-neutrality point[3], an anomalous half-integer quantum hall effect[2,3], observation of a non-zero Berry's phase[3], as well as Klein tunneling[2,18], where the latter has the effect of inhibiting carrier localization in the low density limit.

2.2 Raman spectroscopy of graphene

Raman spectroscopy provides a fast and non-destructive way of characterizing graphene. It is not within the scope of this section to provide the details of Raman spectroscopy in graphene and graphite, for which the interested reader is referred to papers by Ferrari et al.[22,23] and Yu et al.[24], but a summary of the most basic use of Raman spectroscopy as a graphene characterization technique will be provided. Raman spectroscopy provides information about vibrational and rotational modes in the graphene lattice by measuring the scattering of laser light on phonons in the hexagonal lattice. The Raman spectrum of graphene can yield information on the number of layers, density of certain types of defects, strain, edges and doping level[23].

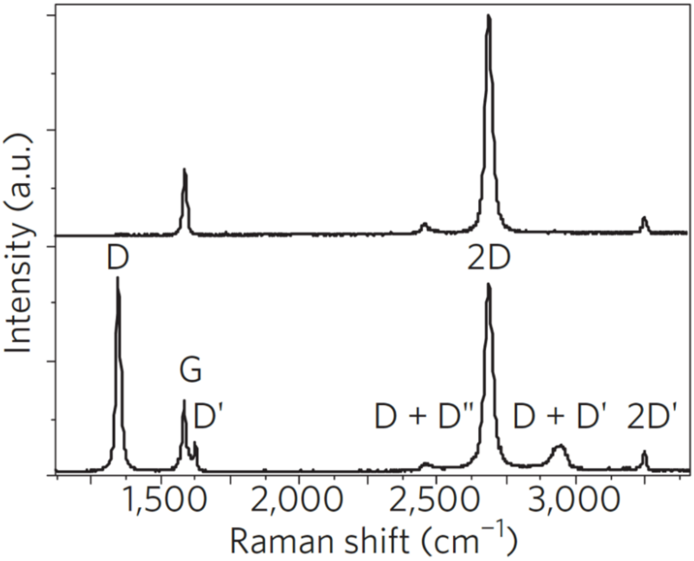

Figure 2.3 : Raman spectra of pristine (top) and defected (bottom) graphene. The main peaks are labelled. Reprinted[23].

Figure 2.3 shows examples of Raman spectra of pristine single layer graphene (top panel) and defected single layer graphene (bottom panel).

The most widely used Raman indicators used for graphene characterization are the D, G, and 2D bands, indicated in Figure 2.3. These correspond to the breathing-mode of the six atoms in the hexagonal cell which requires a defect for activation (D band), bond stretching of all pairs of sp2 atoms in both rings and chains (G band), and the overtone of the fundamental D band (2D band). Because the G and 2D bands originate from momentum-conserving 1-phonon and 2-phonon processes, respectively, they do not require a defect for activation and are always present.[23] Commonly, the ratio of D band to G band intensity, I_D/I_G , is used as an indicator of defect density, as the D band intensity is related lattice defects, edge states and amorphicity. The intensity of the 2D band shows a significant sensitivity to the number of graphene layers, for which reason the ratio of 2D to G band intensity, I_{2D}/I_G , is used for identifying the number of layers. Single layer graphene typically shows ratios of at least $I_{2D}/I_G \geq 1.5$. The width and shape of the D and 2D peaks, which are well described as single lorentzian peaks for single layer graphene but splits into a superposition of several peaks for multiple layers, are used for characterization of the number of graphene layers in a sample.

The less distinct and seldomly analysed peaks in Figure 2.3 are associated with an intra-valley double-resonance process (D' band), a combination of a D phonon and the D'' longitudinal acoustic phonon at 1,100 cm^{-1} (D+D'' band), a combination of D and D' phonons, and the overtone of the D' band. [23]

2.3 Electric field effect, minimum conductance and charge puddles

The possibility of controlling the carrier concentration in semi-metallic few-layer and monolayer graphene films by utilization of the electric field effect was first demonstrated by Novoselov et al. in 2004[1] and by Zhang et al. in 2005[3], respectively. In the experiments the carrier concentration in the graphene films was controlled by applying a back-gate voltage in a graphene/SiO2/Si MOSFET-like structure as indicated in Figure 2.4(a).

As seen in Figure 2.4(b) and (c), it was shown that the gapless electronic spectrum of monolayer graphene allows continuous tuning of the carrier density and type from an electron regime to a hole regime. The experiments showed a linear modulation of the conductivity in the graphene films with the applied gate voltage and a minimum appearing at zero gate bias, interpreted as tuning of the Fermi level to the charge neutrality point.

Application of a gate voltage, V_g, between a back-gate electrode and the graphene film induces a linearly proportional sheet density of carriers, n_s, in the graphene film described as[19]

$$\left|n_s\right| = \frac{C_g}{e}V_g + n_Q\left[1+\sqrt{1+\frac{C_gV_g}{en_Q}}\right]. \tag{2.7}$$

Here C_g is the gate capacitance, e is the electronic charge and $n_Q \equiv (\pi/2)\left(C_g\hbar v_F/e^2\right)^2$. The second term on the right-hand side of equation (2.7) is the so-called quantum capacitance. Under typical experiment conditions with a dielectric constant $\varepsilon_r \approx 4$, and gate dielectric thickness larger than 50 nm, the quantum capacitance of the system can be neglected for gate voltages larger than few hundred mV[19].

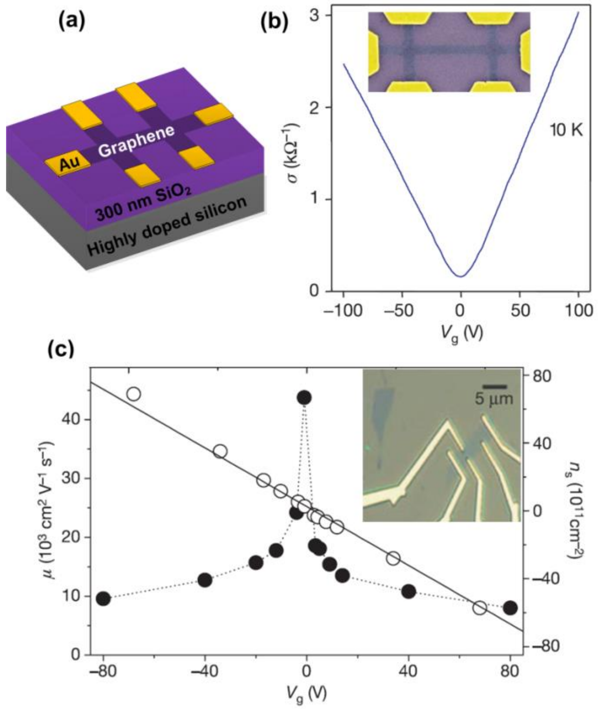

Figure 2.4 : (a) Schematic of the sample structure used in the initial work on electric field effect in graphene films. (b) Sheet conductance as a function of back-gate voltage for a micro-mechanically exfoliated monolayer graphene flake at T=10K. The slopes reflect a field effect carrier mobility of around 15,000 cm^2/Vs. Reprinted[2]. (c) Hall measurements of carrier density and Hall mobility as a function of back-gate voltage at T=1.7K. Reprinted[3]

In this case the gate capacitance is given simply as the capacitance of an ideal plate capacitor with a dielectric medium of dielectric constant ε_r, $C = \frac{\varepsilon_0 \varepsilon_r}{t}$, resulting

$$|n_s| = \frac{\varepsilon_0 \varepsilon_r}{t \cdot e} V_g , \qquad (2.8)$$

where ε_0 is the vacuum permittivity and t is the thickness of gate dielectric. Figure 2.5(a) and (b) shows plots of the approximate and full expressions for the sheet carrier density in electrically gated graphene on 5 Å and 50 nm SiO_2, respectively, illustrating that the quantum capacitance becomes increasingly important for very thin dielectric layers.

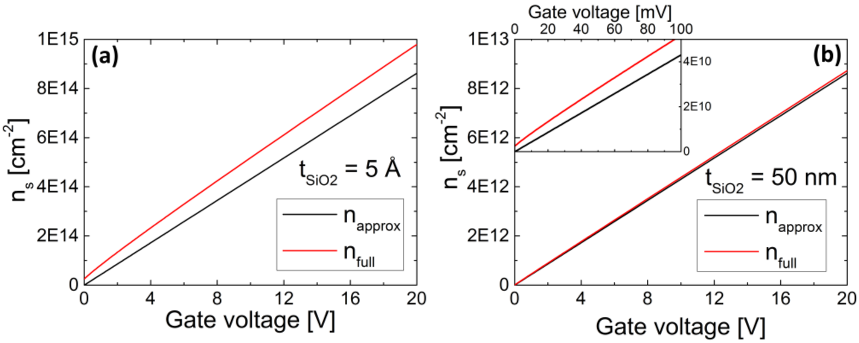

Figure 2.5 : Sheet carrier density calculated from the full expression in equation (2.7) (red lines) and approximate expression where the quantum capacitance, expressed in the second term on the right-hand-side is neglected (black lines), for (a) 5 Å SiO_2 gate dielectric and (b) 50 nm SiO_2 gate dielectric.

For 300 nm SiO_2 the proportionality factor $\varepsilon_0 \varepsilon_r / t \cdot e$ is approximately $7.2 \cdot 10^{10}\,\mathrm{cm}^{-2}\mathrm{V}^{-1}$. The assumption of a voltage-independent capacitance is valid for highly doped back-gate electrodes where the depletion width is negligible.

The observed linear dependence of sheet conductance on gate bias was treated under the framework of a diffusive Drude-type transport regime where sheet conductance, σ_s, and carrier density, n_s, can be related as

$$\sigma_s = e \mu_{FE} n_s = \frac{\mu_{FE} \varepsilon_0 \varepsilon_r}{t} V_g , \qquad (2.9)$$

and the field effect mobility found as

$$\mu_{FE} = \frac{t}{\varepsilon_0 \varepsilon_r}\frac{\sigma_s}{V_g}. \tag{2.10}$$

It should be noted that this relation only holds true sufficiently far away from the charge-neutrality point where a majority carrier density is well-defined[19]. This treatment led to extraction of carrier mobilities on the order of 10.000-15.000 cm^2/Vs[1–3], which agrees with Hall mobility measurements, as shown in Figure 2.4(c).

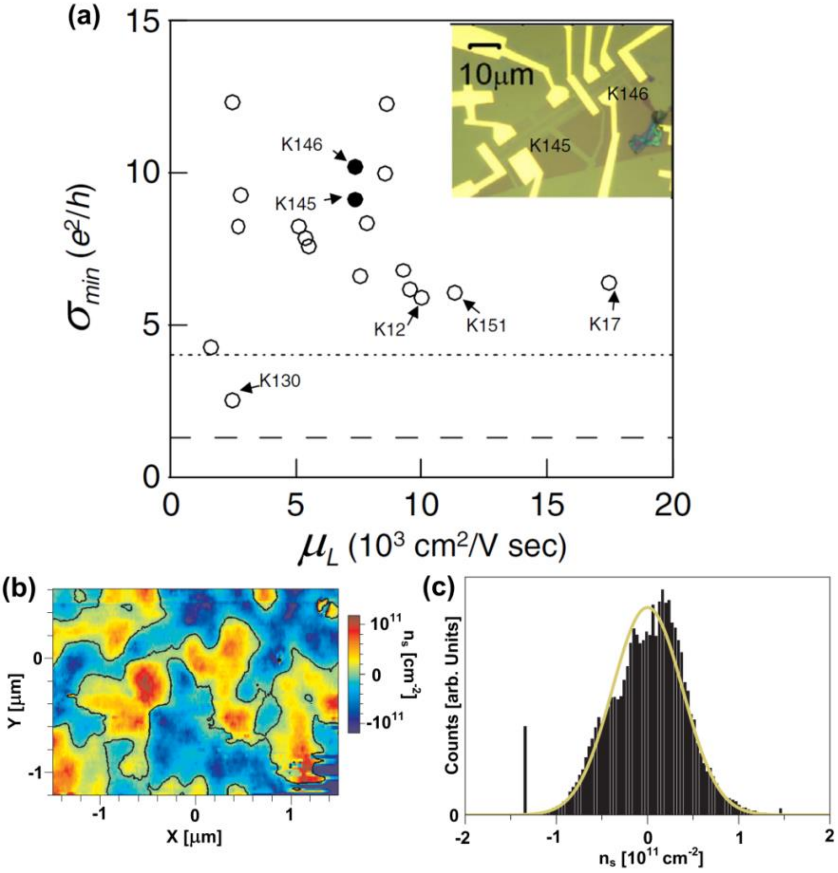

Figure 2.6 : (a) The minimum conductivity and metallic-regime-mobility (mL) for 19 different graphene devices measured at 1.6 K. Filled symbols indicate two devices made from the same graphene flake, as shown in the inset. Reprinted[32] (b) Colour map of the spatial carrier density variations in a graphene flake, extracted from surface potential measurements. The blue regions correspond to holes and the red regions to electrons. Reprinted[33]. (c) Histogram of the density fluctuations in (b). Reprinted[33]

The band structure of graphene predicts a vanishing free carrier density when the Fermi level is tuned to the charge neutrality point, which would normally be expected to result in a vanishing conductivity. For graphene, however, a minimum conductivity has been observed in the region between hole-like and electron-like conduction[2]. Several theoretical studies[25–31] have offered explanations as well as suggested values for a universal minimum conductivity in graphene. However, as shown in Figure 2.6(a), experimental evidence points to a finite but non-universal minimum conductivity that depends on the disorder and charged impurity doping, found to also be reflected in the scattering time and carrier mobility, of the specific graphene sample[32]. It is believed that the non-universal minimum conductivity should be attributed to the appearance of a type of percolative transport in an electron-hole puddle landscape near the charge-neutrality point[34,35], with a number of possible causes including nanoscopic disorder, fluctuations in substrate- and residue-induced doping as well as structural distortions such as e.g. nanoscopic ripples[32–34,36]. This notion is supported by experimental results obtained by scanning single-electron transistor microscopy[33], shown in Figure 2.6(b) and (c), where nanoscopic carrier density fluctuations on the order of $2 \cdot 10^{11}\,\text{cm}^{-2}$ was found in the limit of vanishing average carrier density.

2.4 High mobility monolayer crystals and the scattering mechanisms in graphene

Pronounced de-localization of graphene charge carriers[19], weak electron-phonon interactions[21] and high attainable graphene crystal quality[1,15,37] give rise to exceptionally long carrier scattering times of up to 1.5 ps measured in experiments[14,21,32].

This has resulted in extremely high experimentally validated carrier mobilities even at high carrier concentrations. As shown in Figure 2.4(b) and (c), electric field-effect and Hall mobility measurements on graphene resting on SiO_2 substrates has produced carrier mobility values of up to 15,000 cm^2/Vs[2,3] at 10K and 1.7K, respectively, with little dependence on carrier density and temperature up to 100K. Meanwhile, mobilities as high as 500,000 cm^2/Vs and $>10^6$ cm^2/Vs have been reported for room temperature graphene on hexagonal boron nitride substrates[14] and ultra-clean suspended graphene at T=10 K[38], respectively. In terms of carrier mobility, graphene thus outperforms silicon based devices with a factor of between 10 and

~600. Significantly higher carrier mobilities have been observed in GaAs 2D electron gases (2DEG) at cryogenic temperatures, however, as shown in Figure 2.7 these structures show much lower mobilities at room temperature[39], due to carrier dynamics mainly limited by phonon-interactions.

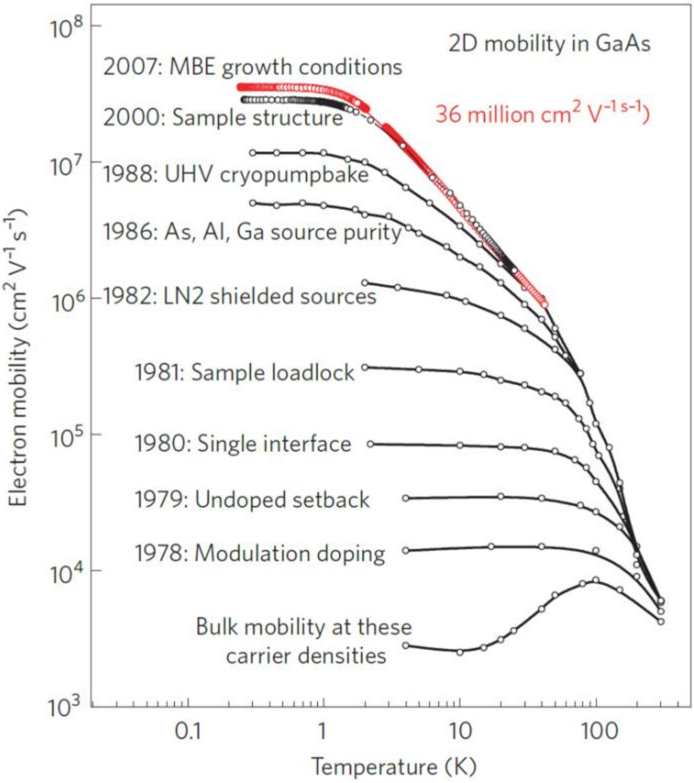

Figure 2.7 : The mobility progress achieved at Bell Labs for GaAs 2DEGs over the last three decades, leading up to the present mobility record of 36.000.000 cm^2/Vs. The curve labelled 'bulk' is for GaAs single crystal doped with the same concentration of electrons as the 2DEGs. MBE: molecular-beam epitaxy; LN2: liquid nitrogen; 'undoped setback': and undoped layer prior to the modulation doping to further separate the ionized impurities from the 2DEG. Reprinted[39].

The high mobilities and long carrier scattering times observed in graphene experiments are quite remarkable testaments to the de-localization and weak interaction of Dirac Fermions as well as to a high graphene crystal quality[1–3,16,37,40]. This is perhaps best appreciated by considering that in a material with a Fermi velocity as high as $v_F = 10^6\,\mathrm{m/s}$, the observed scattering times correspond to ballistic transport across mean free paths, $l = v_F \tau$, upwards of 1.5 μm at room temperature in a 2D electron gas which is at most separated from material interfaces by a few Å[1,14].

Although the carrier scattering mechanisms in graphene include carrier-carrier and carrier-phonon collisions, recent theoretical[18,19,34,35,41] and experimental work[32,36] indicates that diffusive carrier transport is limited by short-ranged scattering on neutral crystal defects and long-range scattering on extrinsic charged impurities, giving rise to two qualitative different behaviors in transport experiments.

Charge transport dominated by short-ranged scattering, with a $\tau \propto 1/\sqrt{n}$ dependence of the momentum-averaged carrier scattering time, τ, predicted from Boltzmann transport theory[19,34,35], is expected to result in a density-independent conductivity[18,19,21,34,35,42] since

$$\sigma = \frac{e^2 v_F}{\hbar\sqrt{\pi}}\sqrt{n}\tau, \tag{2.11}$$

which is also obtained for graphene in the framework of Boltzmann transport theory[19,34,35,42]. In contrast, graphene carrier transport dominated by long-range scattering on charged impurities yields a $\tau \propto \sqrt{n}$ dependence[18,19,34,35], resulting in conductance that depends linearly on carrier density as expressed by equation (2.11)[18,19,34,35], in agreement with experimental results. This also provides a relation between carrier mobility and carrier scattering time within the regime of long-range impurity scattering. Since $\sigma = en\mu$ we have

$$\mu = \frac{ev_F}{\hbar\sqrt{\pi}}\frac{\tau}{\sqrt{n}}. \tag{2.12}$$

Short-range scattering is expected to have significance only when charged impurities, with density n_i, are effectively screened in the high-density-limit when $n \gg n_i$[19,34,35]. The influence of short-range scattering is thus expected to be observable primarily in ultra-clean samples where n_i is small.

As shown in Figure 2.8(a), (b) and (c), recent transport experiments on very clean graphene samples have shown sub-linear $\sigma(V_g)$ consistent with transport where both short-range and long-range scattering have significant contributions[21,32,36]. In experiments where potassium ions, acting as charged impurities, were deposited in-situ on a graphene flake in ultra-high vacuum

(UHV), a transition from sub-linear dependence to linear dependence was observed, consistent with transition to carrier transport dominated purely by long-range charged impurity scattering[36].

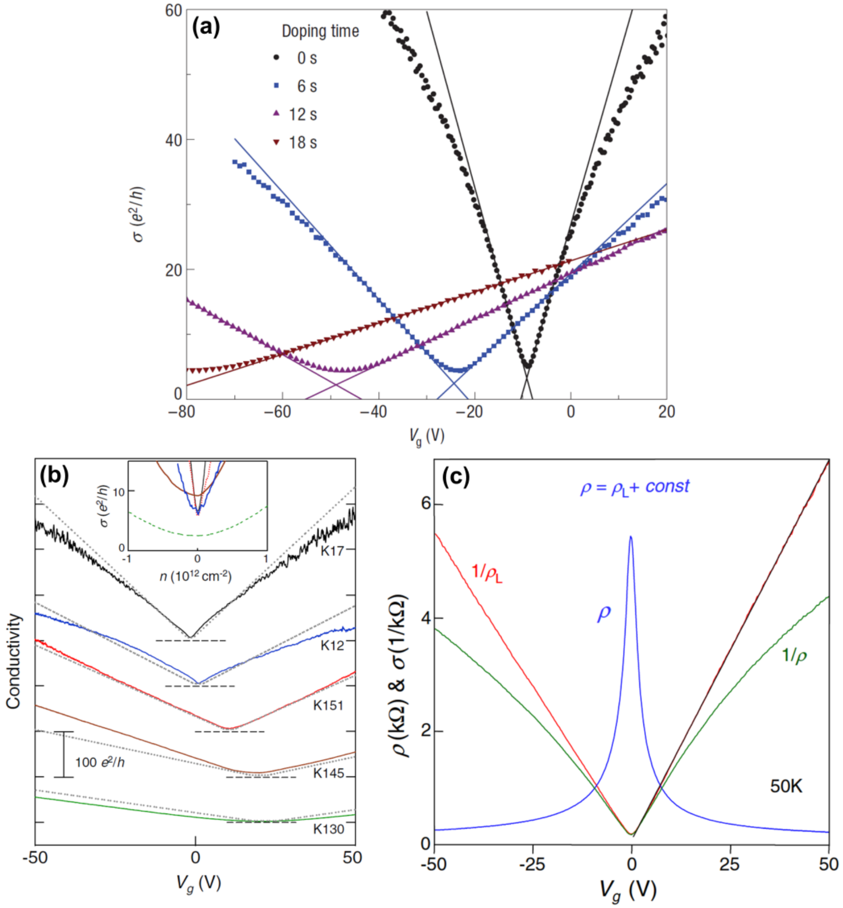

Figure 2.8 : (a) The conductivity vs. gate voltage for a pristine graphene film (black) and three different potassium doping concentrations (blue, purple, red) taken at 20K in ultra high vacuum. Reprinted[36] (b)The conductivity vs. gate voltage of five different graphene samples with different levels of disorder. For clarity, the curves are vertically displaced. The horizontal dashed lines indicate the zero conductance for each curve. Dotted curves are fits to a Boltzmann transport model for charged impurity scattering, taking into account the effect of impurity density on the slope, minimum conductivity position and width as well as minimum conductivity value. The inset shows a detailed view of the density-dependent conductivity near the CNP. Reprinted[32]. (c) Resistivity r (blue curve) and conductivity s=1/r (green curve) as a function of gate voltage. When a density-independent resistivity contribution from short-ranged scattering is subtracted, the conductivity due to long-range charged impurity scattering, linear with V_g, is recovered. Reprinted[21].

Based on Boltzmann theory for graphene transport dominated by long-range charged impurity scattering a semi-classical, Drude-type expression for the frequency-dependent conductivity can thus be constructed[18,34,41–44]:

$$\tilde{\sigma}(\omega)=\frac{\sigma_{DC}}{1-i\omega\tau}, \tag{2.13}$$

where $\sigma_{DC}=\frac{e^2 v_F}{\hbar\sqrt{\pi}}\sqrt{n}\tau$. It should be noted that τ in this expression is the carrier density-dependent scattering time, expected to scale with $\sqrt{n}$. The basics of the classical Drude model are explained in the following section.

2.5 The Drude model

The Drude model is a classical model for the transport dynamics of free massive charge carriers under influence of an electric field, **E**, in solid state systems in the diffusive regime. In its classical formulation presented here, some aspects of the model, such as e.g. the notion of a finite carrier mass, does not apply directly for description of the massless Dirac fermions in graphene. However, graphene charge carrier dynamics have been shown to be phenomenologically well described by the Drude form, and it may serve as a good basis for understanding the concepts of diffusive carrier transport in graphene, limited by random scattering events.

The Drude model considers the kinetics of the free charge carriers as analogous to that of molecules in a gas, by describing the system as comprised of completely free and independent carriers moving ballistically between randomly occurring elastic scattering events. A basic assumption of the model is that a collision results in complete randomization of the carrier momentum and thermalization with the surroundings, and that the occurrence of collisions is described by an average, characteristic rate, $\Gamma = 1/\tau$, where τ is the average time between collisions. The average equation of motion of charge carriers can be deduced by considering the first time-derivative of carrier momentum, $\frac{\partial\mathbf{p}}{\partial t}=\frac{\mathbf{p}(t+dt)-\mathbf{p}(t)}{dt}$. According to the model assumptions there is a $P_C=dt/\tau$ chance of collision, resulting in an average momentum $\mathbf{p}_C(t+dt)=0$, while there is a $P_{NC}=1-dt/\tau$

chance that no collision will occur, resulting in the momentum evolving unhindered as $\mathbf{p}_{NC}\left(t+dt\right)=\mathbf{p}\left(t\right)+\mathbf{F}\left(t\right)dt$. The new average momentum is thus

$$\begin{aligned}\mathbf{p}\left(t+dt\right)&=P_C\cdot\mathbf{p}_C\left(t+dt\right)+P_{NC}\cdot\mathbf{p}_{NC}\left(t+dt\right)\\&=\left(1-\frac{dt}{\tau}\right)\left[\mathbf{p}\left(t\right)+\mathbf{F}\left(t\right)dt\right],\end{aligned}\tag{2.14}$$

which enables evaluation of the first time-derivative of momentum, expressing the equation of motion averaged over charge carriers

$$\frac{d\mathbf{p}}{dt}=\lim_{dt\to 0}\frac{\mathbf{p}\left(t+dt\right)-\mathbf{p}\left(t\right)}{dt}=-\frac{\mathbf{p}\left(t\right)}{\tau}+\mathbf{F}\left(t\right).\tag{2.15}$$

This may analogously be written as

$$m^*\frac{\partial\mathbf{v}}{dt}=-\frac{m^*}{\tau}\mathbf{v}\left(t\right)-e\mathbf{E}\left(t\right)\tag{2.16}$$

where m* is the effective mass of charge carriers, when moving between collisions, *e* is the electronic charge, and **v** is the velocity of charge carriers. The desired solution for a response to an applied electric field with frequency *ω*, $Re\left[\mathbf{E}(t)\right]=Re\left[\mathbf{E}\left(\omega\right)e^{-i\omega t}\right]$, is of the form $Re\left[\mathbf{v}(t)\right]=Re\left[\mathbf{v}\left(\omega\right)e^{-i\omega t}\right]$. Inserting **E**(*t*) and **v**(*t*) in equation (2.16) yields

$$\left(-i\omega\right)\mathbf{v}\left(\omega\right)=-\mathbf{v}\left(\omega\right)\frac{m^*}{\tau}-e\mathbf{E}\left(\omega\right),\tag{2.17}$$

which can be rewritten as

$$\frac{\mathbf{v}\left(\omega\right)}{\mathbf{E}\left(\omega\right)}=\frac{-e\tau/m^*}{1-i\omega\tau},\tag{2.18}$$

By using the definition $\tilde{\sigma}=\frac{\mathbf{J}\left(\omega\right)}{\mathbf{E}\left(\omega\right)}=\frac{-en\mathbf{v}\left(\omega\right)}{\mathbf{E}\left(\omega\right)}$, we arrive at the complex, frequency-dependent conductivity

$$\tilde{\sigma}(\omega) = \frac{ne^2\tau/m^*}{1 - i\omega\tau} = \frac{\sigma_{DC}}{1 - i\omega\tau}, \tag{2.19}$$

where $\sigma_{DC} = ne^2\tau/m^*$ is the conductivity at $\omega = 0$. Explicitly separated in real and imaginary parts, it becomes

$$\sigma_{real}(\omega) = \sigma_{DC}\frac{1}{1 + (\omega\tau)^2} \tag{2.20}$$

$$\sigma_{imag}(\omega) = \sigma_{DC}\frac{\omega\tau}{1 + (\omega\tau)^2} \tag{2.21}$$

In a steady-state situation, where $dv/dt = 0$, equation (2.16) reduces to

$$\mu = \frac{\mathbf{v}}{\mathbf{E}} = \frac{e\tau}{m^*}, \tag{2.22}$$

defining the carrier mobility, μ, which is the ratio of the average drift velocity of the carrier distribution to the electric field. Combined with the expression for σ_{DC}, the well-known relation $\sigma_{DC} = en\mu$ is obtained.

2.6 Defects in large-scale graphene

Though initially fabricated by micro-mechanical exfoliation of graphite, which is a labour-intensive process yielding small quantities of graphene flakes of typically 10-100 μm lateral dimensions[1], a multitude of techniques for production of graphene on a large scale are now available. Although the performance gap is rapidly shrinking[45,46], graphene produced in large scale methods so far provides electronic properties that are highly varying and in most cases inferior to that of mechanically exfoliated graphene. In the following, short descriptions are given of the most widely applied methods for large-scale graphene production, to provide a qualitative understanding of the type of defects expected to degrade the electronic properties of large-area graphene compared to its mechanically exfoliated counterpart as well as a qualitative understanding of their impact on electronic properties.

The most common large-scale fabrication techniques include bulk production using liquid-phase exfoliation of graphite or graphite oxide[47–50] and large-area synthesis by epitaxial growth from high temperature sublimation of silicon from silicon-carbide (SiC) surfaces[51–53] as well as chemical growth by catalyzed chemical vapor deposition[54,55]. In principle there are no fundamental limitations on the size of graphene films that can be obtained from these methods, and films with dimensions of several to tens of inches have already been demonstrated by liquid-phase exfoliaton[56] and CVD processing[57], respectively. However, the currently available size of SiC substrates means that the epitaxial growth method is in practice limited to 4 inch wafer sizes.

2.6.1 Liquid-phase exfoliation

In liquid-phase exfoliation, large-area films are obtained from graphene[47,50] or reduced graphene oxide[48] (r-GO) flakes dispersed in a liquid solution, by e.g. spin-coating, spray-coating or Langmuir-blodgett methods. A slurry of few-layer flakes is typically obtained by sonication of graphite or graphite oxide in a solvent or surfactant with suitable surface energy. By subsequent centrifugation[47], and an added chemical reduction step in the case of graphite oxide[48], a dispersion of primarily few-layer graphene or r-GO flakes can be obtained. The average lateral flake dimensions obtained in films prepared from this technique is typically on the order of few μm, as graphite or graphite oxide crystallites are known to be torn during the sonication procedure.

2.6.2 Epitaxial growth on SiC

Epitaxial growth of graphene from SiC substrates[51–53] is based on the formation of the graphene crystal structure on the surface of a SiC substrate by thermal sublimation of silicon and decomposition of the surface at temperatures typically in the range 1200-1800^o C. Epitaxial graphene growth in inert Argon atmosphere has been shown to allow higher growth temperatures, resulting in larger homogeneous graphene flakes of up to few micrometer in width and hundreds of micrometer in length, primarily limited by terrace steps in the surface morphology of the starting SiC substrate[52]. Growth of multilayer graphene films on the SiC(0001) C-face does however produce much larger continuous and uniform regions[51,58]. Graphene layers grown by thermal decomposition of SiC surfaces show some chemical interaction with the underlying substrate, however, quasi-isolated graphene layers with electronic properties similar to that of isolated graphene monolayers are observed in parts of multi-layer structures separated from the substrate by a few graphite inter-layer distances[51].

2.6.3 Chemical vapor deposition on metal catalysts

The chemical vapor deposition (CVD) of graphene films onto metal substrates[54,59] rely on the catalyzed decomposition of carbon pre-cursors in a gaseous phase, often in the form of CH_4 or C_2H_4, and their structuring into the graphene honeycomb crystal structure. In particular, Ni[59] and Cu[54] have been demonstrated as suitable catalytic growth substrates, yielding both monolayer and few-layer large-area graphene films. The catalytic growth is typically carried out at low pressures and temperatures close to 1000^{o} C[54,59], yielding poly-crystalline monolayer or multi-layer graphene films with grain sizes on the order of 10 μm across[60]. The poly crystallinity of deposited films is usually attributed to growth proceeding from a high density of nucleation sites or discontinuous growth across metal substrate grain boundaries[60–63]. The deposited graphene films can be transferred to insulating substrates, appropriate for electronic utilization, by a number of techniques typically involving sacrificial etching of the metal catalyst substrate[55]. Growth and transfer of 30-inch CVD graphene films have been demonstrated, as well as their subsequent use as transparent electrode for touch-screens[57].

2.6.4 Extended defects in large-area graphene

Common for the above-mentioned large-scale production techniques is that they all produce graphene with more defects than micro-mechanically exfoliated graphene, resulting in a generally lower and highly varying electronic quality. Imperfect growth in epitaxially grown and chemical vapour deposited graphene as well as incomplete reduction[47,50] subsequent to graphite oxidation in liquid-phase exfoliated graphene is likely to lead to an increased density of crystal defects.

In additions to this, it is expected that flake and grain boundaries in the poly-crystalline graphene films can form significant extended electronic barriers[64], which in particular are expected to degrade long-range transport[62]. In addition to degrading the DC conductivity of the graphene films, the existence of such extended defects can lead to perturbation of the characteristic form of the frequency-dependent conductivity, by causing preferential back-scattering of charge carriers. In AC transport measurement, such as a THz-TDS investigation, the probing length scale in a diffusive regime is defined by the frequency as $L=\sqrt{D/\left(2\pi f\right)}$, where D is the diffusion constant and f is the frequency. This can be thought of as the distance that a charge carrier moves within one half period of an oscillating electric field. Back-scattering by defects on a characteristic length scale will therefore primarily affect the conductivity response at lower frequencies corresponding to a probing length that is larger than the characteristic defect length scale. Put differently, a charge carrier cannot respond as effectively to the applied field if it is confined within the probing length scale. Despite predictions of de-localization and suppressed back-scattering at electronic barriers, due to Klein tunneling of chiral, quasi-relativistic graphene charge carriers[18], we present observations of pronounced signatures of preferential back-scattering in CVD graphene in our experimental studies in chapter 4.

In the following section, the consequences for the frequency dependent conductivity in the THz range of such extended defects and their preferential back-scattering of charge carriers are considered in the framework of the Drude-Smith model.

2.7 The Drude-Smith Model

The Drude-smith model is a classical model, developed by N.V. Smith, that aims to incorporate the phenomenon of preferential carrier back-scattering, or persistence of carrier velocity in scattering events, within a diffusive transport picture similar to the Drude framework[65]. It was developed with the goal of reproducing the conductivity features of a range of disordered conductive materials that could not be accurately described by the Drude model, such as quasi-crystals[65,66], percolative systems[67], and nanocrystalline systems[68–71]. Such materials show a suppression in the low frequency $\sigma_{real}(\omega)$, rising to a peak at non-zero frequency, accompanied by a $\sigma_{imag}(\omega)$ that can go negative in the low frequency range.

To account for back-scattering the Drude-Smith model parts with one of the fundamental assumptions of the Drude model, stating that a carrier scattering event results in complete momentum randomization. This is necessary, as back-scattering specifically implies that the carrier momentum, **k** is reversed to **–k**. Put differently, a key concept in the Drude-Smith model is the introduction of a memory effect that allows the momentum of carriers prior to a scattering event to influence the momentum subsequent to a scattering event.

N.V. Smith introduced this memory effect on basis of the impulse response formalism, where the frequency dependent conductivity is found as the Fourier transform of the impulse current response function. He expressed the current response function using Poisson statistics as

$$j(t)\,/\,j(0)=\mathrm{e}^{-t/\tau}\left[1+\sum_{n=1}^{\infty}c_n\frac{\left(t/\tau\right)^n}{n!}\right], \tag{2.23}$$

where c_n is the fraction of the carrier momentum retained after the n*th* scattering event. This should be viewed in contrast to the corresponding current impulse response function for the Drude model, which is a single exponential decay. The Fourier transform of equation (2.23) leads to the Drude-Smith model for frequency dependent conductivity:

$$\tilde{\sigma}\left(\omega\right)=\frac{W_D}{1-i\omega\tau}\left[1+\sum_{n=1}^{\infty}\frac{c_n}{\left(1-i\omega\tau\right)^n}\right], \tag{2.24}$$

where $W_D=ne^2\tau/m^*$ is the Drude-weight. Normally, persistence of velocity is only considered for the first collision subsequent to carrier excitation, corresponding to inclusion of only the first term in the sum in equations (2.23) and(2.24). This has the meaning that only the first scattering event deviates from the regular isotropic Drude scattering mechanism, and momentum memory thus goes only as far back as prior to the last collision experienced by the charge carrier. By inclusion of only the first term in the sum, equation (2.24) can be written explicitly in real and imaginary parts as

$$\sigma_{real}\left(\omega\right)=\frac{W_D}{\left(1+\omega^2\tau^2\right)^2}\left[1+(\omega\tau)^2+c\left(1-\omega^2\tau^2\right)\right] \tag{2.25}$$

$$\sigma_{imag}\left(\omega\right)=\frac{W_D\omega\tau}{\left(1+\omega^2\tau^2\right)^2}\left[1+(\omega\tau)^2+2c\right] \tag{2.26}$$

where c_1 is now denoted c. Here, only values of c ranging from 0 to -1 are considered, as these correspond to the situation where velocity is predominantly or fully negated in scattering events, therefore reflecting back-scattering of carriers.Figure 2.9 shows the real and imaginary parts of the Drude-Smith conductivity given in equations (2.25) and (2.26) normalized to the Drude weight W_D for $\tau = 50$ fs and the back-scattering parameter c ranging from 0 to -1.

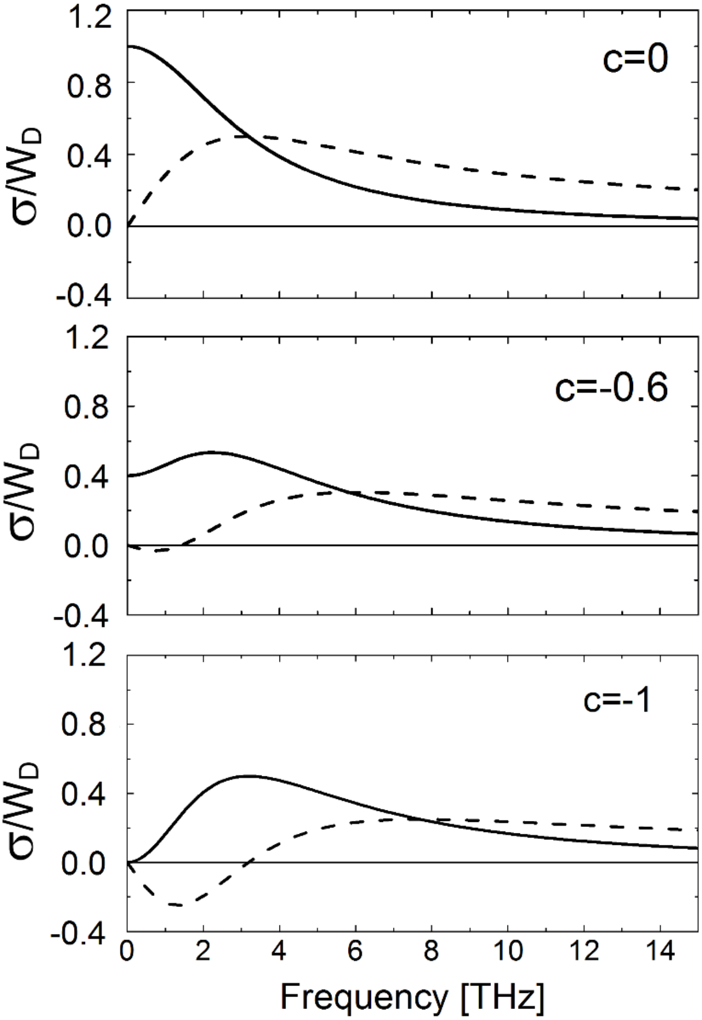

Figure 2.9 : Drude-Smith conductivity normalized to the Drude weight for scattering time $\tau = 50$ fs and back-scattering parameter c ranging from 0 til -1. Full lines are the real part of the conductivity and dashed lines are the imaginary part of the conductivity. Based on equations (2.25) and (2.26)

As seen from the top graph, a simple Drude response is retrieved when the backscattering parameter $c = 0$, corresponding to complete randomization of the momentum at scattering events. When c goes negative, a suppression of the real and imaginary parts of the conductivity takes place for low frequencies, where the imaginary part also can go negative for c values lower than -0.5. A negative imaginary conductivity reflects a capacitive response, consistent with an intuitive picture of disordered conductors where conducting regions are separated by (semi-)insulating barriers. In the limit of c = -1, the DC conductivity is completely suppressed, reflecting an insulator-like response, similar to that obtained in a Lorentz-oscillator model.

A perhaps more intuitive view of the modeling of carrier transport within the Drude-Smith framework may be offered by examining the truncated impulse current response function in equation (2.23) in more detail.

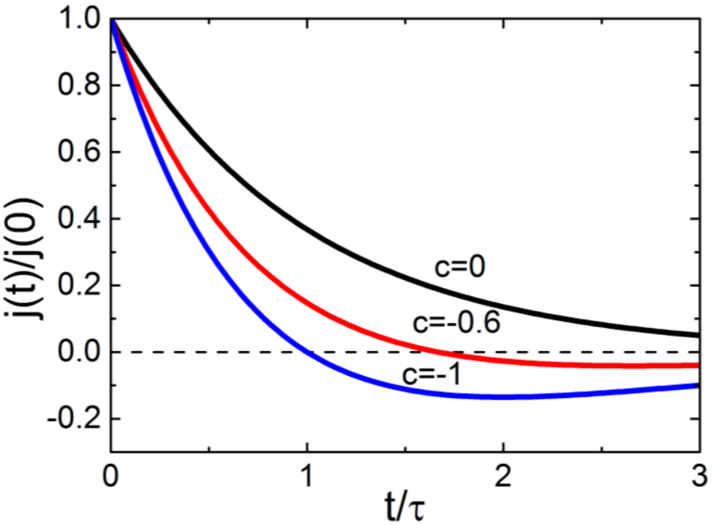

Figure 2.10 : A direct impact of the phenomenological inclusion of back-scattering in the Drude-Smith model can be seen in the impulse current response function, here plotted for three different values of *c*. In the Drude-case (*c*=0) the current falls monotonically to zero as an exponential decay, while the current actually goes negative for negative values of c, directly reflecting back-scattering. Reprinted[65]

In Figure 2.10 the truncated impulse current response function is plotted for c-values of 0, -0.5 and -1. In the Drude-case when c = 0, the current drops monotonically to zero expectedly as an exponential decay. For negative c-values, however, the net current goes negative before relaxing to zero, reflecting that charge carriers reverse their movement direction due to back-scattering.

3 Terahertz time-domain conductance spectroscopy

Since the first demonstrations of Terahertz time-domain spectroscopy(THz-TDS) in the late 1980's [72,73], the technique has evolved into an entire scientific research field of its own, spurred by the unique access it provides for coherent probing of low-energy electromagnetic excitations in matter. The terahertz frequency range, sometimes also referred to as the "Terahertz gap" due to a historical lack of efficient sources and detectors, is typically defined as the span from 0.1 THz to 20 THz.

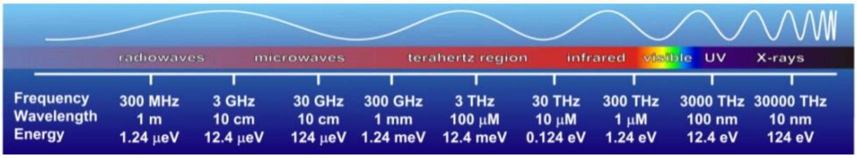
radiowaves
microwaves
terahertz region
infrared
visible
UV
X-rays
Frequency
Wavelength
Energy
300 MHz
1 m
1.24 μeV
3 GHz
10 cm
12.4 μeV
30 GHz
10 cm
124 μeV
300 GHz
1 mm
1.24 meV
3 THz
100 μM
12.4 meV
30 THz
10 μM
0.124 eV
300 THz
1 μM
1.24 eV
3000 THz
100 nm
12.4 eV
30000 THz
10 nm
124 eV

Figure 3.1: The electromagnetic spectrum. The THz frequency region, or "THz gap", is situated between microwaves and infrared regions.

On the lower frequency side of this range, electronics-based microwave sources and detectors have been readily available for several decades, and on the upper side of the THz frequency range, infrared optical sources and detectors provided a well-developed technology base. Until the appearance of efficient and convenient table-top sources around 2 decades ago, spectroscopic studies in the THz gap had to resort to radiation sources such as thermal or backward-wave oscillator sources[74] or extensive free-electron lasers[75], that were either weaker or much less convenient to use. Today, highly sensitive spectroscopy at THz frequencies is obtainable in compact systems through coherent generation and detection of sub-picosecond, single-cycle, free-space propagating, electromagnetic pulses in photoconductive switches(PCS)[76,77] or non-linear media[78–85].

THz-TDS thus provides experimental access to light-matter interactions in a wide range of low photon energies from about 0.41 meV (0.1 THz) to 82 meV (20 THz), which is the relevant range for a large number of physical phenomena such as vibrational and rotational states of large molecules[86], the superconducting energy gap[87], exciton transitions[88–90], as well as optical and acoustic phonon modes[91], just to name a few. THz radiation is, however, also perfectly suited for studying free charge carrier dynamics in semiconductor solid-state systems[68,92–94] because the characteristic frequencies of free charge carrier conduction dynamics often fall within the THz range. In this thesis THz-TDS based on generation and detection in PCS as well as in laser-induced air plasmas[85] is applied with the purpose of studying free charge carrier dynamics in graphene in the frequency ranges from 0.15-1.5 THz and 1-15 THz, respectively. In the following sections the experimental THz-TDS setups are described along with descriptions of the methodology for extraction of the complex, frequency-dependent sheet conductance of graphene films from THz-TDS transmission data.

3.1 Picometrix T-ray 4000 fiber-coupled terahertz time-domain spectrometer & imaging system

The T-ray™ 4000 from Picometrix© is a commercial fiber-coupled THz-TDS relying on InGaAs photoconductive switches (PCS) for generation and detection of ultrashort THz pulse transients. It incorporates a fs fiberlaser, beam splitter, a fast-scanning delay line, a long range delay line, dispersion compensation optics, 5m optical fiber links, compact THz emitter- and detector units with PCS, Si substrate lenses and dielectric lenses, and readout electronics in a single 19U rack-mountable box, as shown in Figure 3.2, with the system controlled from a connected laptop computer. A schematic of the components in the system is shown in Figure 3.2.

Formation of ultra-short current transients through acceleration of photo generated carriers in PCS’es is one of the most widely used techniques for generation and detection of terahertz radiation today. The applied concept of using ultrashort optical pulses to control acceleration of charge carriers in semiconductor materials on a sub-picosecond time scale was first introduced in 1975 by D. H. Auston [95]. In 1988 the technique was extended by Ch. Fattinger and D. Grischkowsky for generation and subsequent detection of

THz electromagnetic pulses following 2 cm of free-space propagation [96]. 24 years later, in what can be seen as a remarkable testament to the importance of this pioneering work towards establishing a solid platform for THz pulse generation and detection, a free-space THz pulse, generated and detected in PCS, was propagated over 170 meters by Grischkowsky and co-workers[97].

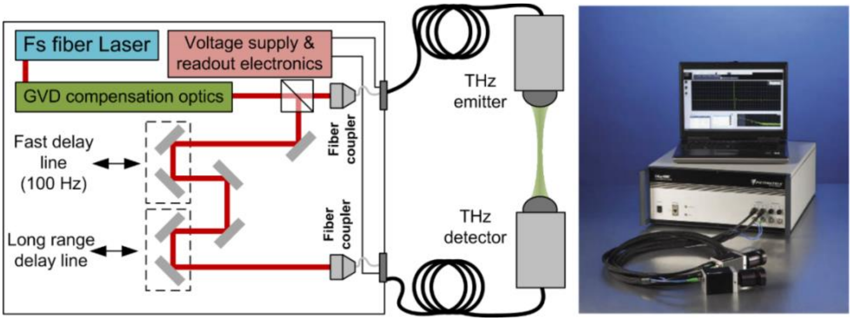

Figure 3.2: Schematic of the components in the Picometrix© T-ray™ commercial fiber-coupled terahertz time-domain spectrometer. Alongside is shown a photograph of the THz spectrometer along with a laptop running the control software (www.picometrix.com).

A PCS is an electrical switch controlled by an optical signal, based on photoconductivity. It consists of two metallic electrodes separated by a gap deposited on a photo-active semiconductor material of high resistivity, as sketched in Figure 3.3(a). Typically a substrate lens made from a material with refractive index close to that of the photoconductive PCS substrate, such as high resistivity silicon (HR-Si), is used in combination with the PCS, as shown in Figure 3.3(b), to collect and collimate the highly diverging THz radiation emerging from the sub-wavelength hertzian dipole point source.

To efficiently excite sub-picosecond current transients, several material parameters are of crucial importance for the photoconductive substrate in the PCS. A suitable semiconductor material possesses a high intrinsic resistivity, a short free carrier lifetime, a high breakdown field and high carrier mobility. Low temperature grown GaAs (LT-GaAs) and related III-V compound semiconductors, such as low temperature InGaAs (LT-InGaAs), are some of the most frequently chosen materials for the purpose, particularly due to high intrinsic carrier mobilities combined with carrier lifetimes down to 200 fs facilitated by carrier trapping and non-radiative recombination at defects incorporated during crystal growth[98]. A wide range of other semiconductor materials (e.g. radiation damaged silicon-on-sapphire, indium phosphide, and chromium-doped Si-GaAs[98]) have also been shown to work well.

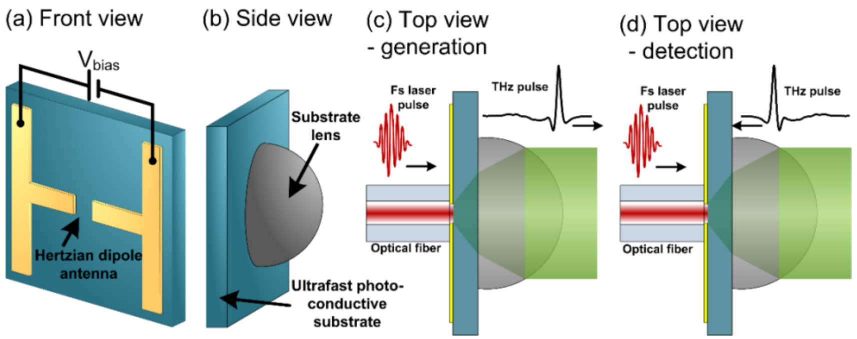
(a) Front view
(b) Side view
(c) Top view
- generation
(d) Top view
- detection
V_{bias}
Hertzian dipole antenna
Substrate lens
Ultrafast photo-conductive substrate
Fs laser pulse
THz pulse
Optical fiber
Fs laser pulse
THz pulse
Optical fiber

Figure 3.3: Schematic layout of traditional photoconductive switches. (a) Front view of a PCS showing the metallic electrode and photoconductive gap forming the Hertzian dipole antenna responsible for THz emission. (b) Side view showing the HR-Si substrate lens used to collect and collimate the highly diverging THz radiation emerging from the Hertzian dipole point-source. (c) Top view showing the configurational scheme for THz generation in a PCS. (d) Top view showing the coniguratonal scheme for THz detection in a PCS.

When a PCS is utilized for generation of THz pulses a bias voltage, V_{bias}, is applied across the dipole gap as indicated in Figure 3.3(a). The dipole gap is then short-circuited on an ultra-short timescale by illuminating the gap with a fs optical laser pulse, as indicated in Figure 3.3(c). This creates a dense, electrically conducting electron-hole gas in the gap region with a lifetime determined by the carrier trapping time, τ_t, of the semiconductor material. The photo excited free electrons and holes are accelerated by the electric field in the gap, $\mathbf{E}_{gap}(t)$, which is a superposition of the applied bias field and a time-dependent opposing field created by the separation of positive (photo-generated holes) and negative (photo-generated electrons) charges. This results in a current transient described by the relations

$$\mathbf{J}(t) = -en\mathbf{v}(t) \tag{3.1}$$

$$\frac{dn}{dt} = -\frac{n}{\tau_t} + G(t) \tag{3.2}$$

$$\frac{d\mathbf{v}}{dt} = -\frac{\mathbf{v}(t)}{\tau_s} + \frac{e}{m^*}\mathbf{E}_{gap}(t) \tag{3.3}$$

$$\mathbf{E}_{gap}(t) = \mathbf{E}_{bias} + \frac{\mathbf{P}_{sc}(t)}{\eta\varepsilon} \tag{3.4}$$

$$\frac{d\mathbf{P}_{sc}}{dt} = -\frac{\mathbf{P}_{sc}}{\tau_r} + \mathbf{J}(t) \tag{3.5}$$

where e is the electronic charge, $\mathbf{v}(t)$ is the carrier velocity, n is the density of free carriers, $G(t)$ describes the photo-generation of free carriers, τ_s is the momentum relaxation scattering time, m^* is the effective carrier mass, $\mathbf{E}_{bias}$ is the electric field due to an applied bias voltage, $\mathbf{P}_{sc}(t)$ is the time-dependent polarization due to space-charge region created by the separation of positive (photo-generated holes) and negative (photo-generated electrons) charges, ε is the permittivity of the substrate, η is a geometrical factor, and τ_r is the carrier recombination time. The electromagnetic radiation emitted due to the resulting current transient can be described self-consistently on basis of Maxwell's equations[99]

$$\nabla \times \mathbf{E}_{THz}(t) = -\mu \frac{\partial \mathbf{H}_{THz}(t)}{\partial t} \tag{3.6}$$

$$\nabla \times \mathbf{H}_{THz}(t) = \mathbf{J}(t) + \frac{\partial \varepsilon(t) \mathbf{E}_{THz}(t)}{\partial t} \tag{3.7}$$

where $\mathbf{E}_{THz}(t)$ is the radiated electrical field, $\mathbf{H}_{THz}(t)$ is the radiated magnetic field and μ is the permeability of the substrate.

When a PCS is used for detection of THz pulses, the bias voltage source shown in Figure 3.3(a) is replaced by a current detection across the gap. In the PCS detection scheme the electric field of the THz pulse acts as a transient bias on any free carriers, inducing a current transient proportional to the THz electric field, of which the time-integrated value can be measured as a quasi-DC signal by means of electronic readout. Relying on the short free carrier lifetime of a PCS substrate which is much shorter than the THz pulse, time-gating the presence of free carriers in the PCS gap on an ultra-short timescale by photo-excitation with fs laser pulses, as indicated in Figure 3.3(d), facilitates time-resolved measurement of the THz electric field. The photocurrent, $J_{measured}$, across the PCS gap is given by the convolution of the transient surface photoconductivity, $\sigma_{s,photo}(t)$, and the THz electric field profile[98]

$$J_{measured} = \int_{-\infty}^{t} \sigma_{s,photo}(t - t') E_{THz}(t') dt' \tag{3.8}$$

$$\sigma_{s,photo}(t)=\frac{e(1-R_{opt})}{\hbar\omega}\int_{-\infty}^{t} I_{opt}\left(t''\right)\mu(t,t'')n\mu(t,t'')dt'' \qquad (3.9)$$

where R_{opt} is the optical reflectivity, I_{opt} is the optical intensity, $\mu(t,t'')$ is the mobility at time t of a free carrier generated at time t'', and $n(t,t'')$ is the population at time t of free carriers generated at time t''. From the Fourier transform of the photocurrent it follows that the detection is filtered according to the dynamics of $\sigma_{s,photo}(t)$:

$$\tilde{J}_{measured}(\nu)=\tilde{\sigma}_{s,photo}(\nu)\tilde{E}_{THz}(\nu) \qquad (3.10)$$

The transient surface photoconductivity of a detector system with a carrier lifetime τ = 500 fs, a momentum relaxation time τ_s = 30 fs and an optical pulse width of 132.8 fs Full width half maximum (FWHM) is shown in Figure 3.4(a). The finite impulse response of the detector system sets an upper frequency limit on the detection bandwidth, as it is evident from the Fourier transform in Figure 3.4(b). In addition, the detector response at low frequencies is reduced due to diffraction effects in the THz focus onto the PCS surface. Since the lower frequencies of the THz pulse are focused to larger spots, the corresponding field strengths at the PCS gap position are lower, resulting in reduced responsivity[98]. This diffraction effect is included in the detector response function shown as a dashed line in Figure 3.4(b).

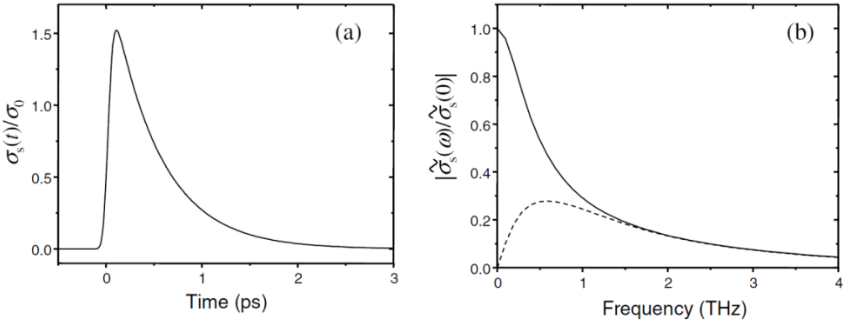

Figure 3.4: Transient sheet photoconductivity of a detector system with τ_c=500 fs, τ_s=30 fs and an optical pulse FWHM of 132.8 fs. (a) time-domain representation (b) frequency-domain representation. The dashed line indicates the response function of the detector when diffraction effects are included. Reprinted[98]

The Picometrix© T-ray™ 4000 system provides a spectroscopic bandwidth of 0.1-2.2 THz with a peak signal-to-noise ratio in amplitude of up to around 7000, when used with 22mm thick, poly-ethylene lenses with a working distance of 25.4mm, such as that used for the work presented in this thesis (see Figure 3.5).

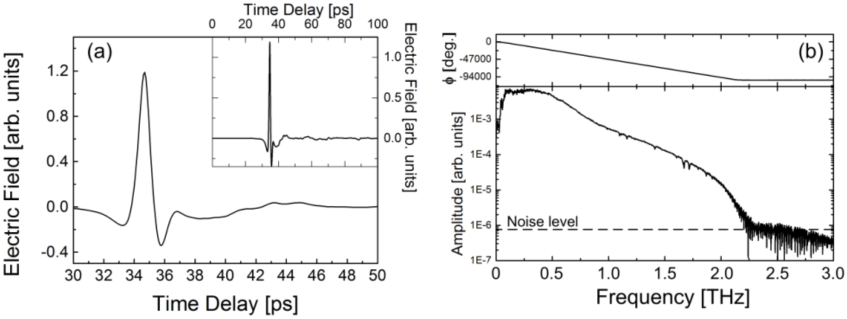

Figure 3.5: (a) Terahertz time-domain waveform recorded with the Picometrx© T-ray™ 4000 system using 22mm thick aspheric poly-ethylene lenses with a working distance of 25.4 mm. (b) Fourier transform of the THz transient in (a).

The frequency-dependent full-width-at-half-maximum (FWHM) of the focused THz beam in this configuration was assessed by scanning the beam across a straight edge of a macroscopically highly uniformly conducting CVD graphene film deposited on a high resistivity silicon substrate at normal incidence. The FWHM was evaluated by monitoring the change in transmitted THz power in 100 GHz frequency-intervals, when scanning across the edge. As shown in Figure 3.6(a) the FWHM was found to change from roughly 1.5 mm to 0.3 mm in the range from 0.25-1.6 THz.

As it is also evident from Figure 3.6(a), the resolution of the THz-TDS imaging setup is close to the Abbe diffraction limit of $\frac{\lambda}{2 \cdot NA}$, where the numerical aperture is defined by

$$\begin{aligned} NA = \sin\theta &= \sin\left[\tan^{-1}\left(L_f \big/ R_{lens}\right)\right] \\ &= \sin\left[\tan^{-1}\left(25.4\text{mm} \big/ 19\text{mm}\right)\right] = 0.801 \end{aligned} \tag{3.11}$$

Due to the fast scanning delay line, data is recorded at a rate of 100 waveforms/second in a scanning window of 320 ps with 78 fs temporal resolution, translating into a frequency resolution of around 3 GHz.

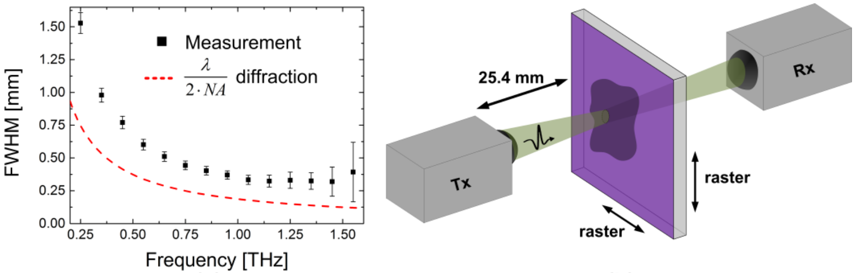

(a) (b)

Figure 3.6: (a) FWHM as a function of frequency for the Picometrix© T-ray™ 4000 system using aspheric poly-ethylene with a working distance of 25.4 mm. Data is obtained by scanning the focused THz beam across the edge of a very straight and highly uniform CVD graphene film. (b) THz image formation in the Picometrix© T-ray™ 4000 is carried out by raster scanning the sample in the focal plane between THz emitter and detector equipped with aspheric poly-ethylene lenses with working distance of 25.4mm. Full THz time-domain waveforms are recorded in each pixel of an image.

The T-ray™ 4000 system is coupled with an imaging system, comprising a 2D precision scanning stage controlled by the T-ray™ 4000 system, which facilitates terahertz time-domain spectroscopic raster imaging. In the work presented in this thesis, spectroscopic images of CVD graphene films were acquired by placing samples on the 2D scanning stage in the focal plane between a stationary THz emitter and a stationary THz detector equipped with aspheric poly-ethylene lenses with a working distance of 25.4 mm, as it is shown in Figure 3.6(b).

3.2 *Ultra-broadband terahertz time-domain spectroscopy based on THz air photonics*

While the bandwidth of conventional THz-TDS systems is typically limited to a few THz, generation and detection of THz transients utilizing non-linearities in gases exposed to intense laser fields[84,100–103] have been shown to provide bandwidths up to 200 THz and 150 THz[104] for generation and detection respectively, due to far fewer fundamental constraints on the bandwidth of the process.

The bandwidth limitation of conventional THz-TDS systems originates primarily from the carrier dynamics in PCS semiconductor materials and from phase-mismatch between generation/detection laser light and THz radiation in non-linear crystals, often caused by material resonances.

Because dry air as well as nitrogen provides close to perfect phase-matching across the entire electromagnetic spectrum and do not exhibit any absorption resonances, THz-TDS based on generation and detection in air - coined 'THz wave air photonics'[85] – provide spectroscopic bandwidths that to a first order is only limited by the fs laser pulse bandwidth. In addition the acquired waveforms do not suffer from reflections in the detection media, which work to limit the spectral resolution of other techniques. THz wave air photonics is applied in this thesis to obtain usable bandwidth from 1-30 THz in free space THz-TDS experiments.

3.2.1 THz pulse generation in a two-color laser-induced air plasma

In recent years it has been shown that efficient free space THz transient generation can be obtained from the formation of ultra-short laser induced air plasma, by focusing of fs laser pulses with their second harmonic[100,102,105] (SH). While a detailed understanding of the THz generation process requires consideration of the electron trajectories[106,107] and transient micro-currents[108,109] in the two-color air plasma as well as the influence of its finite length on phase-matching between the fundamental and second-harmonic beams[110–113], an approximation is offered by a four-wave mixing description[85,100,114] in the non-linear two-color air plasma environment

$$E_{THz} \propto \chi^{(3)} E_{2\omega} E_{\omega}^{*} E_{\omega}^{*} \tag{3.12}$$

where two fundamental photons, E_{ω}^{*}, are mixed with a SH photon, $E_{2\omega}$, through the non-linear third-order susceptibility, $\chi^{(3)}$, of the air plasma to produce a THz photon. In terms of dependence on optical power the THz field can thus be written as

$$E_{THz} \propto \chi^{(3)} \sqrt{I_{2\omega}} I_{\omega} \cos(\varphi) \tag{3.13}$$

where φ explicitly denotes the relative phase between fundamental and SH wavelengths. Xie et al. showed that THz generation was most efficient when fundamental, SH, and THz photons are all polarized along the same axis, corresponding to the $\chi^{(3)}_{xxxx}$ term of the third-order susceptibility[102].

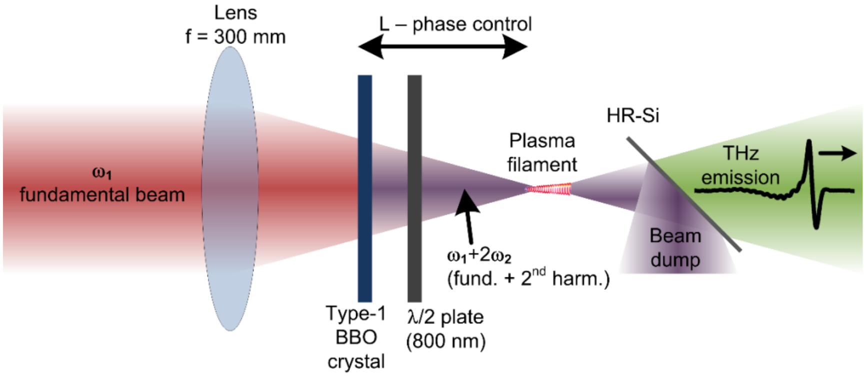

Figure 3.7: Schematic of experimental setup for generation of free-space THz transients from a two-color laser induced air plasma.

The utilized implementation of THz generation from a two-color laser-induced air plasma is shown in Figure 3.7. A 100 µm thick type-1 β-barium borate(BBO) crystal, used to generate λ = 400 nm SH of the fundamental λ = 800 nm pulses, is placed a distance L after a lens focusing the beam to form a plasma filament at a distance of 300 mm. By adjusting the position of the BBO crystal relative to the focus point, the relative phase between the fundamental and SH at the position of the air plasma is adjusted according to[105]

$$\Delta\varphi = \frac{\omega}{c}\left(2n_{2\omega} - n_{\omega}\right)\Delta L \tag{3.14}$$

The type-1 BBO crystal is placed such that the e axis of the crystal is perpendicular to the polarization of the fundamental beam in order to maximize the 800nm to 400 nm conversion efficiency. This results in generation of 400 nm pulses with a polarization that is perpendicular to that of the fundamental 800 nm pulses. After the BBO crystal a zero-order half-wave plate for 800 nm is therefore used to rotate the polarization of the fundamental beam by 90^{o}, matching the polarization of fundamental and SH beams for efficient generation of THz radiation in the air plasma. Finally a high resistivity silicon wafer is used to block residual 800 nm and 400 nm light.

3.2.2 Air-biased coherent detection of THz pulses

Quasi-coherent detection of THz pulses using the third order non-linearity in ambient air was first reported by Dai et al. in 2006[103]. This work was later extended to a fully coherent heterodyne THz pulse detection technique in air biased by an applied AC electric field[115]. This technique, which is outlined in Figure 3.8, allows measurement of THz transients by recording the THz-induced SH-generation (SHG) from an 800nm probe beam. It is based on the interaction between the fundamental laser field, E_{800nm}, and the THz field, E_{THz}, in the presence of an externally applied, oscillating electric field, E_{bias}.

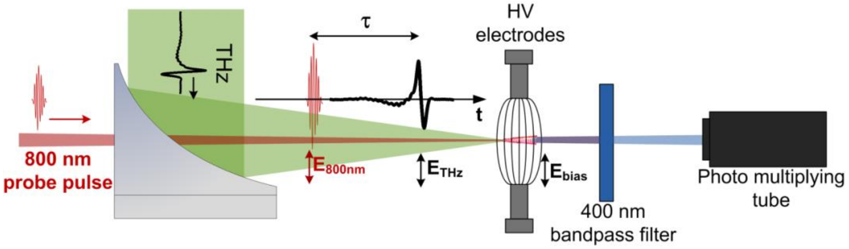

Figure 3.8: Schematic of experimental setup for air-biased coherent detection of THz transients.

Within the picture of four-wave mixing the creation of a SH optical field (2ω) due to focusing of the fundamental probe pulse (ω) and the THz pulse without application of an AC electrical bias can be described:

$$E_{2\omega}^{THz} \propto \chi^{(3)} E_{THz} E_{\omega} E_{\omega} \tag{3.15}$$

This process, however, results in a THz-induced SH intensity which is proportional to THz intensity, as $I_{2\omega} \propto I_{THz}$, and will therefore not allow coherent detection of THz pulses. By introducing the external AC bias at the focus point, as shown in Figure 3.8, generation of a local oscillator SH field with amplitude, $E_{2\omega}^{LO} \propto \chi^{(3)} I_{\omega} E_{bias}$, occurs through four wave mixing of fundamental and AC bias fields. $E_{2\omega}^{LO}$ can now mix with the THz-induced SH, $E_{2\omega}^{THz}$, producing a total SH intensity of the form

$$\begin{aligned} I_{2\omega} \propto \left\langle \left(E_{2\omega}\right)^2 \right\rangle &= \left\langle \left(E_{2\omega}^{THz} + E_{2\omega}^{LO}\right)^2 \right\rangle \\ &= \left\langle \left(E_{2\omega}^{THz}\right)^2 \right\rangle + \left\langle \left(E_{2\omega}^{LO}\right)^2 \right\rangle + 2\left\langle E_{2\omega}^{THz} E_{2\omega}^{LO} \right\rangle \end{aligned} \tag{3.16}$$

If the polarity of E_{bias} is controlled such that the carrier envelope phase between $E_{2\omega}^{THz}$ and $E_{2\omega}^{LO}$ is either 0° or 180°, (the external field changes direction with every other THz pulse) the cross term has a fixed value, and the SH intensity can be written as

$$I_{2\omega} \propto \left(\chi^{(3)} I_{\omega}\right)^2 \left[\left(E_{THz}\right)^2 + \left(E_{bias}\right)^2 \pm 2E_{bias}E_{THz}\right] \tag{3.17}$$

where the sign of the cross term is determined by the polarity of E_{bias}. The cross term can easily be isolated by performing a lock-in detection at the oscillation frequency of the AC bias field. The second harmonic intensity measured by the lock-in amplifier in such a scheme is given by

$$I_{2\omega} \propto 4\left(\chi^{(3)} I_{\omega}\right)^2 E_{bias}E_{THz} \tag{3.18}$$

Based on this scheme the THz waveform can be mapped in time by changing the THz-probe time-delay, τ, shown in Figure 3.8.

3.2.3 THz air photonics spectrometer

The terahertz air photonics time-domain spectrometer used in this thesis is based on the methods for THz generation and detection in air outlined in the previous sections. The setup, shown in Figure 3.9, is based on fs, near infrared pulses from a Spectra-physics Spitfire Pro Ti:sapphire regerative amplifier system providing 35 fs laser pulses at a center wavelength of 800 nm with 1.5 mJ pulse energy.

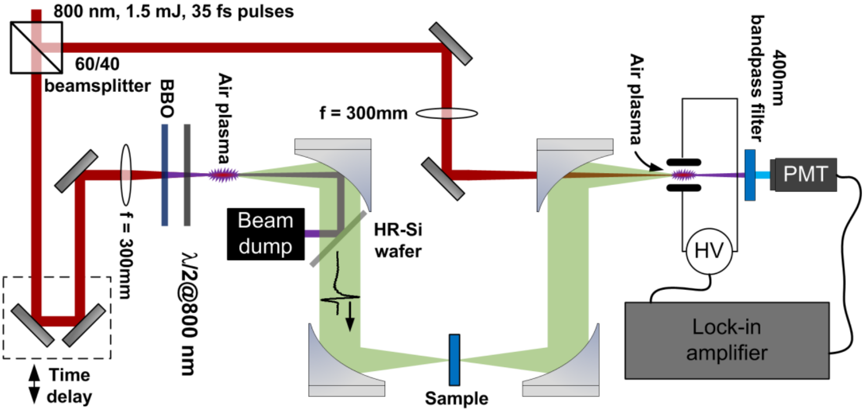
800 nm, 1.5 mJ, 35 fs pulses
60/40 beamsplitter
BBO
Air plasma
f = 300mm
f = 300mm
λ/2@800 nm
Beam dump
HR-Si wafer
Time delay
Sample
Air plasma
400nm bandpass filter
PMT
HV
Lock-in amplifier

Figure 3.9: Schematic of experimental setup for ultra-broadband THz-TDS by two-color plasma THz generation and air-biased coherent detection.

The laser beam is first split by a beam splitter into two parts for generation and detection of THz pulses. To facilitate temporal mapping of THz waveforms, the time delay between THz and detection pulses is controlled using a computer-controlled delay stage in the generation laser beam path. The generation laser beam is focused using a 300 mm focal lenth lens along with its SH beam, generated in a type-1 BBO crystal, to form plasma filamentation from which THz pulses are emitted. Before reaching the focus, the polarization of the fundamental beam is rotated by 90° by a zero-order half wave plate to match the polarization of the SH beam. Off-axis parabolic mirrors are used to collimate and focus the emitted THz radiation at sample and detection positions. After collimation by the first off-axis parabolic mirror, a 2 mm thick high resistivity silicon wafer is used to filter residual laser light from the THz generation process. The detection laser beam is focused through a hole in the last off-axis parabolic mirror onto the detection position using a 300 mm focal length lens. Here, the detection beam forms a plasma filament between two high voltage copper electrodes with approximately 3 mm separation. The entire THz optical path is placed inside a box purged with dry nitrogen. A 500 Hz square voltage signal with 6 kV amplitude, synchronized to the laser pulse train such that the polarity of the electric bias field changes sign with every other THz pulse, is applied across the copper electrodes. Finally the intensity of the THz-induced SH light, produced through mixing of detection light, THz light and bias field, is measured using a photomultiplier tube and a lock-in amplifier synchronized to the oscillation frequency of the high voltage bias field.

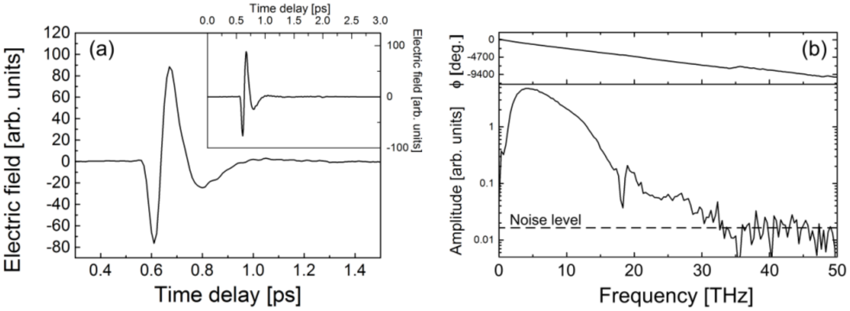

Figure 3.10: THz waveforms recorded in the THz air photonics spectrometer provide bandwidth from 1 to up to 30 THz. (a) time-domain THz waveform recorded with a temporal resolution of 10 fs. Inset shows the full temporal trace from 0 to 3 ps (b) Fourier transform of the temporal waveform in (a) shows bandwidth from approximately 1-30 THz

THz waveforms with bandwidth from 1 to up to 30 THz can be recorded in the system as shown in Figure 3.10. The dip in the amplitude spectrum in Figure 3.10(b) at 18.6 THz is an absorption band due to the coupling of transverse acoustic (4.5 THz) and transverse optical (14.1 THz) phonon modes in Si at the X point[116,117].

3.2.4 Spectra-physics Spitfire Pro Ti:Sapphire regenerative amplifier system

The Spectra-physics Spitfire Pro is a Ti:Sapphire regenerative amplifier system providing fs laser pulses for THz air photonics spectroscopy. A regenerative amplifier system produces high-power ultra-short laser pulses by multiple passes of ultra-short seed pulses along with high-power pump pulses in a gain medium inside a resonator cavity.

As indicated in Figure 3.11, the amplifier system consists of four main parts. Two of these parts are the ‘Millennia Pro’ diode-pumped frequency doubled solid-state pump laser delivering 4.2 W CW power and the ‘Tsunami’ Ti:Sapphire oscillator, which provides seed pulses with a duration of 25 fs, bandwidth of 60 nm, pulse energy of approximately 5 nJ at a center wavelength of 800 nm and a repetition rate of 76 MHz.

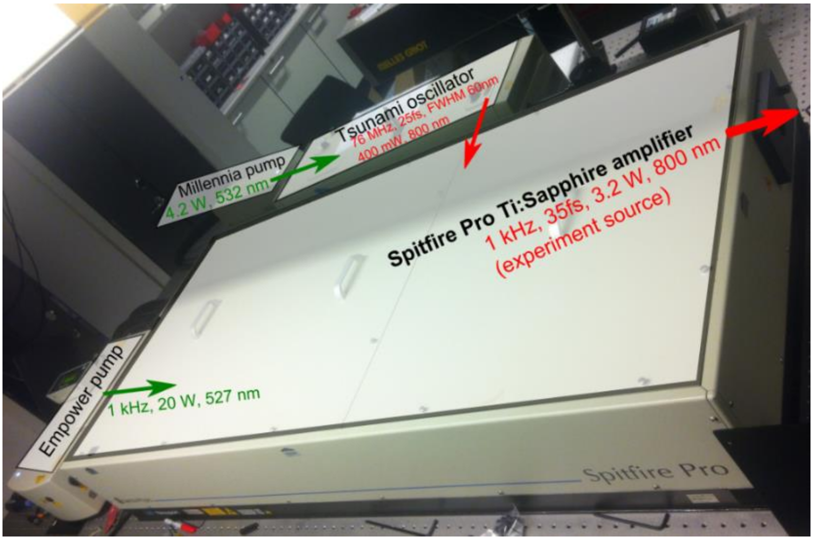
Millennia pump
4.2 W, 532 nm
Tsunami oscillator
76 MHz, 25fs, FWHM 60nm
400 mW, 800 nm
Spitfire Pro Ti:Sapphire amplifier
1 kHz, 35fs, 3.2 W, 800 nm
(experiment source)
Empower pump
1 kHz, 20 W, 527 nm
Spitfire Pro

Figure 3.11: Spitfire Pro Ti:Sapphire regenerative amplifier system from Spectra-physics. Reprinted[118]

The third part of the amplifier system is the ‘Empower’ pump laser which is a diode-pumped, Q-switched Neodymium-doped yttrium lithium fluoride (Nd:YLF) laser delivering frequency-doubled pump pulses with ns duration, 20 mJ pulses energy at $\lambda = 527$ nm and a repetition rate of 1 kHz. The fourth part is the ‘Spitfire Pro’ regenerative amplifier comprising pulse stretching and compression optics, Ti:Sapphire gain crystal and gain resonator, as well as Pockel-cell-based optical switches for picking of synchronized seed and pump pulses and for controlling the number of round-trips in the gain resonator.

The ultra-short pulsed, high-power output from the Spitfire Pro is achieved by amplifying the short seed pulses from the Tsunami by multiple passes through a Ti:Sapphire gain crystal in a resonator cavity pumped by 20 mJ, ns pulses from the Empower pump laser. To avoid non-linear pulse distortion and damage to the gain crystal the seed pulses are temporally stretched by chirping to ns duration using a grating pair prior to insertion in the gain cavity. A Pockel-cell-based optical switch is then used to pick out seed pulses that are synchronized with the 1 kHz pump pulses for insertion into the gain cavity. In the gain cavity the stretched 5 nJ seed pulses are amplified to 3.8 mJ pulse energy by multiple passes in the gain crystal. The number of roundtrips in the gain cavity is actively controlled using a second Pockel-cell-based optical switch. Finally, the pulses are temporally compressed to 35 fs duration in a grating pair. The result is an output of pulses with 35 fs duration, 3.2 mJ energy at 800 nm center wavelength and 1 kHz repetition rate.

3.3 Fresnel equations & THz thin film conductance

The frequency-dependent, complex conductance of conducting thin films, such as graphene, on dielectric substrates can in general be extracted directly from THz-TDS measurements. The physical picture of THz-TDS on conducting thin films is based on interaction between the THz pulse and the free carriers in the film. The THz electric field accelerates carriers, which subsequently scatter and dissipate energy gained from the THz pulse. This energy transfer from the THz electromagnetic wave to the free carriers causes a decrease in the THz field amplitude. The interaction of the THz field with the free carriers may also result in a phase shift of the THz wave caused by a phase delay of the free carrier movement relative to the driving THz field.

To quantify the amplitude decrease and phase delay associated with the response of the conducting thin film, both a reference waveform $E_{ref}(t)$, recorded for transmission through the bare dielectric substrate, and a sample waveform $E_{sam}(t)$, recorded for transmission through the conducting thin film and dielectric substrate, are obtained as indicated in Figure 3.12. The thin film response is isolated in the complex-valued transmission function,

$\tilde{T}_{film}(\omega)$, as the sample Fourier transform, $\tilde{E}_{sam}(\omega)$, divided by the reference Fourier transform, $\tilde{E}_{ref}(\omega)$.

$$\tilde{T}_{film}(\omega) = \frac{\tilde{E}_{sam}(\omega)}{\tilde{E}_{ref}(\omega)} \tag{3.19}$$

$\tilde{T}_{film}(\omega)$ has a direct relation to the complex sheet conductance $\tilde{\sigma}_s(\omega)$ of the thin film, which can be found by considering the expressions for $\tilde{E}_{ref}(\omega)$ and $\tilde{E}_{sam}(\omega)$. When electromagnetic radiation is incident on a bulk medium, it is subject to reflection and transmission at the interfaces of the medium, where changes in amplitude and phase are described by the Fresnel coefficients for transmission, $\tilde{t}$, and reflection, $\tilde{r}$, such that

$$\tilde{E}_t(\omega) = \tilde{t}\tilde{E}_{in}(\omega) \tag{3.20}$$

$$\tilde{E}_r(\omega) = \tilde{r}\tilde{E}_{in}(\omega) \tag{3.21}$$

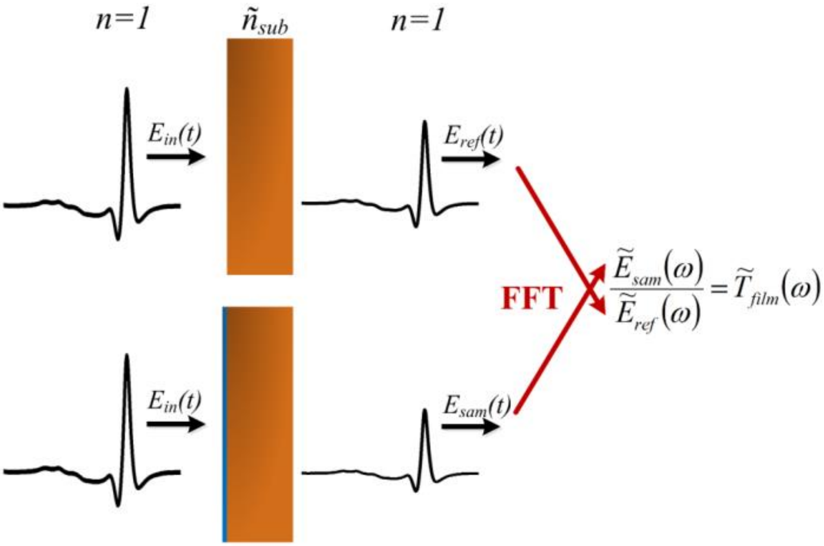
$n=1$
$\tilde{n}_{sub}$
$n=1$
$E_{in}(t)$
$E_{ref}(t)$
FFT
$\frac{\tilde{E}_{sam}(\omega)}{\tilde{E}_{ref}(\omega)} = \tilde{T}_{film}(\omega)$
$E_{in}(t)$
$E_{sam}(t)$

Figure 3.12: The THz response of the conducting thin film is isolated in the complex-valued transmission function, T_{film}, as the sample Fourier transform divided by the reference Fourier transform.

In addition, when passing through a distance ΔL in an absorptive, and dispersive medium characterized by a complex $\tilde{n}$, the radiation is subject to an additional propagation factor of

$$P = e^{i\frac{\omega}{c}\tilde{n}\Delta L} \tag{3.22}$$

For an optically thick medium, where $n_{sub}\Delta L \gg \lambda$ and Fabry-perot effects can be neglected, $\tilde{T}_{film}(\omega)$ can therefore be related to transmission, reflection and propagation factors for the sample and reference case, for each of the temporally separated echoes, created from internal reflection in the bulk substrate, as shown in Figure 3.13.

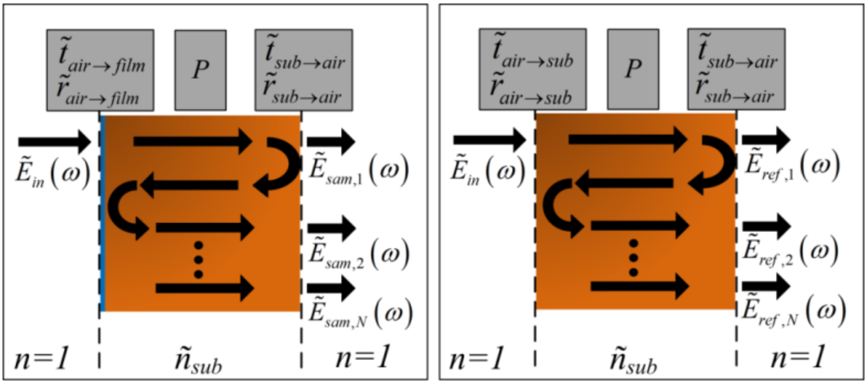
$\tilde{t}_{air\to film}$
$\tilde{r}_{air\to film}$
P
$\tilde{t}_{sub\to air}$
$\tilde{r}_{sub\to air}$
$\tilde{E}_{in}(\omega)$
$\tilde{E}_{sam,1}(\omega)$
$\tilde{E}_{sam,2}(\omega)$
$\tilde{E}_{sam,N}(\omega)$
$n=1$
$\tilde{n}_{sub}$
$n=1$
$\tilde{t}_{air\to sub}$
$\tilde{r}_{air\to sub}$
P
$\tilde{t}_{sub\to air}$
$\tilde{r}_{sub\to air}$
$\tilde{E}_{in}(\omega)$
$\tilde{E}_{ref,1}(\omega)$
$\tilde{E}_{ref,2}(\omega)$
$\tilde{E}_{ref,N}(\omega)$
$n=1$
$\tilde{n}_{sub}$
$n=1$

Figure 3.13: The transmitted THz field are given by a combination of transmission, reflection and propagation coefficients for each of the temporally separated echoes, caused by multiple internal reflections.

Formulated explicitly for the directly transmitted waveform as well as the 1st and 2nd echoes, the transmission functions become

$$\tilde{T}_{film,1}(\omega) = \frac{\tilde{E}_{sam,1}(\omega)}{\tilde{E}_{ref,1}(\omega)} = \frac{\tilde{t}_{air\to film\to sub}\tilde{P}\tilde{t}_{sub\to air}}{\tilde{t}_{air\to sub}\tilde{P}\tilde{t}_{sub\to air}} = \frac{\tilde{t}_{air\to film\to sub}}{\tilde{t}_{air\to sub}} \tag{3.23}$$

$$\begin{aligned} \tilde{T}_{film,2}(\omega) &= \frac{\tilde{E}_{sam,2}(\omega)}{\tilde{E}_{ref,2}(\omega)} = \frac{\tilde{t}_{air\to film\to sub}\tilde{P}^3\tilde{r}_{sub\to air}\tilde{r}_{sub\to film\to air}\tilde{t}_{sub\to air}}{\tilde{t}_{air\to sub}\tilde{P}^3\tilde{r}_{sub\to air}{}^2\tilde{t}_{sub\to air}} \\ &= \frac{\tilde{t}_{air\to film\to sub}\tilde{r}_{sub\to film\to air}}{\tilde{t}_{air\to sub}\tilde{r}_{sub\to air}} \end{aligned} \tag{3.24}$$

$$\tilde{T}_{film,3}(\omega)=\frac{\tilde{E}_{sam,3}(\omega)}{\tilde{E}_{ref,3}(\omega)}=\frac{\tilde{t}_{air\rightarrow film\rightarrow sub}\tilde{P}^5\tilde{r}_{sub\rightarrow air}{}^2\tilde{r}_{sub\rightarrow film\rightarrow air}{}^2\tilde{t}_{sub\rightarrow air}}{\tilde{t}_{air\rightarrow sub}\tilde{P}^5\tilde{r}_{sub\rightarrow air}{}^4\tilde{t}_{sub\rightarrow air}}$$
$$=\frac{\tilde{t}_{air\rightarrow film\rightarrow sub}\tilde{r}_{sub\rightarrow film\rightarrow air}{}^2}{\tilde{t}_{air\rightarrow sub}\tilde{r}_{sub\rightarrow air}{}^2} \qquad (3.25)$$

For boundaries formed between air (n = 1) and bulk, continuous media $\tilde{t}$ and $\tilde{r}$ are given for normal incidence in Table 2.

Interface	**Transmission**	**Reflection**
air →substrate	$\tilde{t}_{air\rightarrow sub}=\frac{2}{1+\tilde{n}_{sub}}$	$\tilde{r}_{air\rightarrow sub}=\frac{1-\tilde{n}_{sub}}{1+\tilde{n}_{sub}}$
substrate → air	$\tilde{t}_{sub\rightarrow air}=\frac{2\tilde{n}_{sub}}{1+\tilde{n}_{sub}}$	$\tilde{r}_{sub\rightarrow air}=\frac{\tilde{n}_{sub}-1}{\tilde{n}_{sub}+1}$

Table 2: Transmission and reflection coefficients at normal incidence for boundaries formed between air and a bulk, continuous medium.

The transmission and reflection of electromagnetic radiation at a boundary between air and a bulk, continuous medium are altered by the presence of a thin film with sheet conductance $\tilde{\sigma}_s(\omega)$. The influence of a conducting thin film is described by the Tinkham equation[119], which states the plane wave transmission and reflection through a thin ($t_{film} \ll \lambda/n_{film}$) conducting film with sheet conductance $\tilde{\sigma}_s(\omega)$ on a bulk substrate with refractive index $\tilde{n}_{subs}(\omega)$. The condition that $t_{film} \ll \lambda/n_{film}$, which can also be formulated as $n_{film}\omega t_{film}/c \ll 1$, ensures that any internal reflections within the thin film can be averaged over and neglected. For metal films this limit is approached even for film thicknesses on the order of several tens of nm, due to their extremely high THz refractive index ($n_{Au,THz}$ ~ 1000). As graphene is a monolayer atomic film with a thickness of maximum a few Å, however, the Tinkham equation is a reliable approximation for the THz response of the 2-dimensional material. For transmission at the air/thin-film/substrate interface and reflection at the substrate/thin-film/air interface the coefficients are given by[120,121]

$$\tilde{t}_{air\rightarrow film\rightarrow sub}\left(\omega\right)=\frac{2}{1+\tilde{n}_{sub}+Z_0\tilde{\sigma}_s\left(\omega\right)} \tag{3.26}$$

$$\tilde{r}_{sub\rightarrow film\rightarrow air}\left(\omega\right)=\frac{\tilde{n}_{sub}-1-Z_0\tilde{\sigma}_s\left(\omega\right)}{\tilde{n}_{sub}+1+Z_0\tilde{\sigma}_s\left(\omega\right)}, \tag{3.27}$$

where Z_0 = 377 Ω is the vacuum impedance. Combining equations (3.23), (3.24), (3.25), (3.26), (3.27) and expressions in Table 2, the relation between thin film sheet conductance, $\tilde{\sigma}_s\left(\omega\right)$, and complex transmission function, $\tilde{T}_{film}(\omega)$, can be explicitly written for the directly transmitted THz fields as well as the 1st echo as

$$\tilde{T}_{film,1}\left(\omega\right)=\frac{\tilde{E}_{sam,1}\left(\omega\right)}{\tilde{E}_{ref,1}\left(\omega\right)}=\frac{1+\tilde{n}_{sub}}{1+\tilde{n}_{sub}+Z_0\tilde{\sigma}_s\left(\omega\right)} \tag{3.28}$$

$$\tilde{T}_{film,2}\left(\omega\right)=\frac{\tilde{E}_{sam,2}\left(\omega\right)}{\tilde{E}_{ref,2}\left(\omega\right)}=\frac{\left(\tilde{n}_{sub}-1-Z_0\tilde{\sigma}_s\left(\omega\right)\right)\left(1+\tilde{n}_{sub}\right)^2}{\left(1+\tilde{n}_{sub}+Z_0\tilde{\sigma}_s\left(\omega\right)\right)^2\left(\tilde{n}_{sub}-1\right)}. \tag{3.29}$$

This results in analytical expressions for the thin film sheet conductance

$$\tilde{\sigma}_{s,1}\left(\omega\right)=\frac{1}{Z_0}\frac{\tilde{n}_A}{\tilde{T}_{film}\left(\omega\right)}-\tilde{n}_A \tag{3.30}$$

$$\tilde{\sigma}_{s,2}\left(\omega\right)=\frac{\pm\tilde{n}_A\sqrt{\tilde{n}_A{}^2+4\tilde{n}_A\tilde{n}_B\tilde{T}_{film}\left(\omega\right)}-\tilde{n}_A{}^2-2\tilde{n}_A\tilde{n}_B{}^2\tilde{T}_{film}\left(\omega\right)}{2\tilde{n}_B Z_0\tilde{T}_{film}\left(\omega\right)}, \tag{3.31}$$

where $\tilde{n}_A=\tilde{n}_{sub}+1$ and $\tilde{n}_B=\tilde{n}_{sub}-1$.

4 Study 1: Broadband terahertz time-domain conductance spectroscopy and imaging of graphene films

Atomically thin graphene films show a very pronounced THz response. As seen in the measurements in Figure 4.1, just a single graphene layer of carbon atoms is enough to reduce the amplitude of a transmitted THz pulse by up to 20%. Similar observations have been made in several other studies [44,122–125]. This large response is a product of the extraordinarily high sheet conductance of graphene layers, facilitated by very high attainable carrier mobilities (up to 500.000 cm^2/Vs on hexagonal Boron nitride substrates) and sheet carrier densities (up to around 10^{13} cm^{-2}).

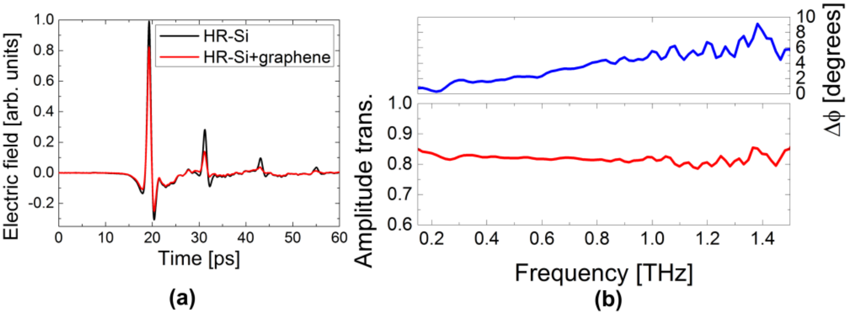

Figure 4.1: Monolayer graphene films exhibit an extraordinarily large THz response due to an exceptionally high conductance. A single atomic layer of CVD graphene is sufficient to reduce the amplitude of transmitted THz pulses by up to 20% as shown for (a) time-domain, and (b) frequency-domain.

Several Fourier transform infrared spectroscopy (FTIR)[44,122,123,126,127]and THz-TDS[124,127] investigations have shown that the frequency dependent optical absorption at THz to mid-infrared frequencies generally follows a Drude model. These observations agree with THz-TDS measurements on epitaxial[122,123] and CVD[121,125,128,129] graphene that has shown spectrally predominantly flat THz responses in the range from 0.15-2.0 THz, consistent with a Drude conductance response and carrier scattering rates that are significantly higher than the measurable frequencies ($\Gamma \gg 2\pi f$). As will be shown later in this chapter, however, a seemingly spectrally flat conductance at low THz frequencies can also reflect non-Drude behavior such as e.g. Drude-smith.

In consistency with most theoretical work on graphene, prior studies indicate that the electrodynamic response of graphene in the THz range at low field strengths (< 1 kV/cm) is dominated by intraband processes reflecting the AC electrical conduction properties of the film.

In this chapter the THz response of graphene grown by CVD on single-crystalline (S-C) Cu (111) as well as poly-crystalline (poly-C) Cu foil is characterized from 0.15-1.5 by THz-TDS THz based on generation and detection in photoconductive switches and from 1-15 THz by THz-TDS based on THz wave air photonics. We show that both amplitude and phase of the THz response is in one case well described by a Drude model and in the other case by a Drude-Smith model for intraband conductivity. Despite of the qualitative difference between THz conductance properties of the two films, these observations testify that the carrier transport in both films is diffusive in nature. By comparison to micro four-point probe measurements we experimentally confirm that the conductance measured by THz-TDS in the low frequency limit ($\Gamma \gg 2\pi f$) of the Drude spectrum for an electrically continuous graphene film reflects the graphene DC conductance. This observation opens up the possibility of utilization of THz-TDS as rapid, quantitative and contact-free metrology tool for mapping of the nanoscopic conductance of large-area graphene, suitable for in-line electrical characterization in industrial settings. Finally, a demonstration of wafer-scale graphene conductance mapping is presented using terahertz time-domain spectroscopic imaging of CVD graphene.

4.1 Complex conductance of CVD graphene at 0.15 to 1.5 THz

Large-area graphene films synthesized by catalytic CVD on single-crystalline Cu (111) as well as poly-crystalline Cu foil are investigated by broadband THz-TDS.

In one case, a single-crystalline Cu (111) catalytic growth substrate is in one case used to promote formation of higher quality graphene with fewer defects. While graphene growth can proceed across copper grain boundaries[62], several groups report that the quality of graphene depends strongly on the crystal facet of copper, with the Cu(111) leading to the highest quality of graphene[130–132]. Ruoff and coworkers[46] showed that annealing copper films deposited onto silicon oxide in a reducing atmosphere prior to graphene growth can align majorities of the film to the (111) direction, leading to overall higher quality of graphene growth. The graphene film was grown by Chemical Vapor Deposition (CVD) in an Aixtron Black Magic vertical cold wall CVD chamber on a one-side polished 10 x 10 x 1 mm single crystal Cu(111) (MTI Corporation, uncertainty 2°) with purity higher than 99.9999%. The sample was initially annealed for 3 hours at 1040°C in a mixed H_2 (1000 sccm)/Ar (200 sccm) atmosphere at 2.8 mbar. After this initial step, the pressure was reduced to 1 mbar by decreasing the hydrogen flow (to 300 sccm), while the temperature was kept constant at 1040°C. The graphene was then grown by introducing methane precursor (2 sccm) for 10 minutes. Finally, the sample was cooled down to room temperature with Ar flow (1000 sccm). The grown graphene film was transferred to a HR-Si substrate on which a 300 nm silicon dioxide film was grown by dry thermal oxidation using a polymer-assisted 3-electrode electrochemical transfer technique with a fixed working potential of $-0.4\ \mathrm{V}$ facilitating transfer of the graphene film while preserving the valuable single-crystalline Cu substrate (see ref iv, List of Publications). This results in the sample structure shown in Figure 4.2(a). An optical microscopy image of the transferred graphene film is shown in Figure 4.2(b).

For comparison, a graphene film grown on a poly-crystalline Cu foil catalytic substrate was investigated. This graphene film was grown in a vertical furnace, where the copper foil was first annealed in hydrogen at a temperature of 1025 °C and pressure of 0.133 mbar. The growth time was approximately 25 min during which the system was maintained at a pressure of 2 mbar and temperature of 1025 °C with a methane flow of 2 standard cubic centimeters per minute (sccm) and a hydrogen flow of 0.5 sccm, similar to previously reported conditions for monolayer graphene growth[24,55]. The grown graphene film was then transferred to a high resistivity silicon wafer by slow etching of the copper foil in a solution of 0.1 M ammonium persulfate ($(NH_4)_2S_2O_8$) with a thin supporting polymethylmethacrylate (PMMA) layer. The PMMA was subsequently removed in acetone. The structure of this sample is thus also represented by Figure 4.2(a). Figure 4.2(c) shows an optical microscopy image of the graphene film.

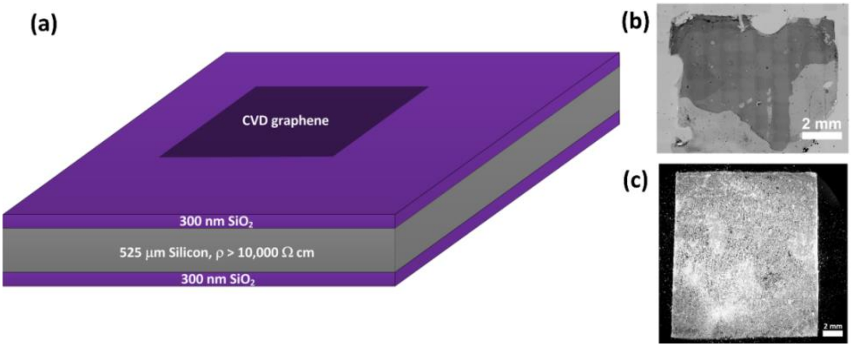

Figure 4.2: (a) Schematic of the sample structure. CVD graphene grown on single-crystalline Cu (111), transferred to HR-Si wafer with 300 nm SiO_2 layer. (b) Optical microscopy image of the CVD graphene grown on single-crystalline Cu after transfer onto oxidized HR-Si wafer. (c) Optical microscopy image of the CVD graphene grown on poly-crystalline Cu after transfer onto oxidized HR-Si wafer. Scale bars are 2 mm.

The THz conductivity of the two graphene films is measured in the range from 0.15-1.5 THz using a Picometrix© T-ray™ 4000 terahertz time-domain spectrometer, detailed in section 3.1, by the procedures described in section 3.3. The response of the graphene films is singled out by taking a reference measurement where the THz radiation is transmitted through the non-graphene-covered HR-Si substrate with n_{Si}=3.417[133,134] and comparing that to a sample measurement where the THz radiation is transmitted through the graphene-covered HR-Si substrate. For the graphene film grown on single-crystalline Cu (111) the THz conductivity is obtained from an analysis of THz waveforms transmitted directly through the sample. Meanwhile, due to a significantly lower THz response, the THz conductivity of the graphene film grown on poly-crystalline Cu foil is obtained from an analysis of the 1st roundtrip echo, resulting from multiple internal reflections in the sample. This approach increases the contrast between reference and sample measurements and works to improve the overall signal-to-noise ratio of the measurement for graphene films with a low THz response. For the graphene film grown on single-crystalline Cu (111) the sample and reference time-domain THz waveforms are shown in Figure 4.3(a), where the inset indicates the 20 ps duration of the Fermi-filtered time-windowing that has been applied around the first peak to the full 320 ps time trace recorded in the measurement. Similarly, Figure 4.3(b) shows sample and reference time-domain THz waveforms for the graphene film grown on poly-crystalline Cu foil, where the inset indicates the 10 ps time-window that was applied around the second peak. The time-window in Figure 4.3(b) is narrower in order to supress features related to the directly transmitted waveform.

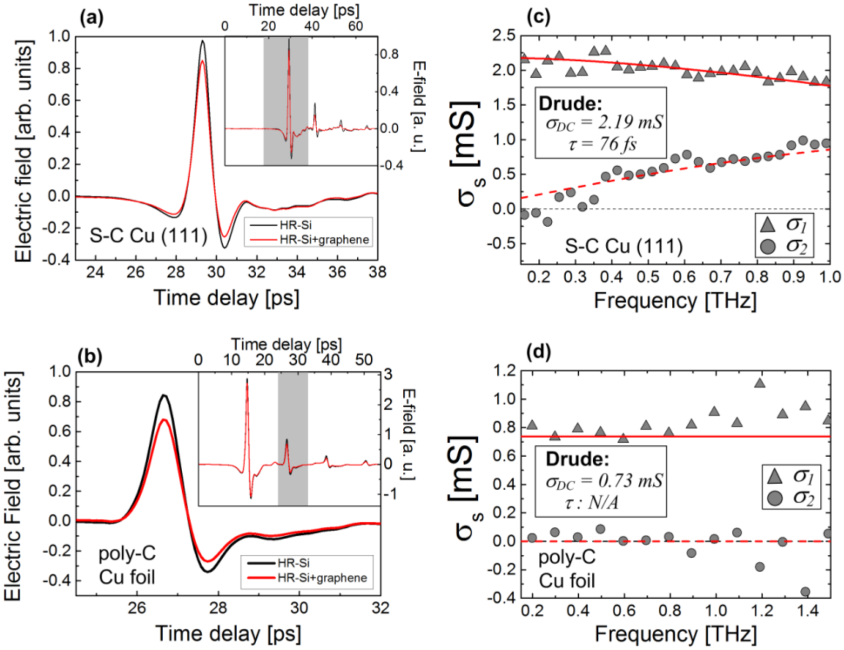

Figure 4.3: Sample and reference THz time-domain waveforms for CVD graphene films grown on (a) single-crystalline Cu (111) substrate (b) poly-crystalline Cu foil. Resulting sheet conductance spectra for (c) single-crystalline Cu (111) substrate (d) poly-crystalline Cu foil.

By analysing the complex Fourier transforms of the time-domain waveforms in Figure 4.3(a) and Figure 4.3(b) according to the procedures outlined in section 3.3, the complex, frequency-dependent sheet conductance, $\tilde{\sigma}_s$, of the two graphene films could be extracted, resulting in the spectra shown in Figure 4.3(c) and Figure 4.3(d). The time-domain measurement for the S-C Cu (111) graphene film in Figure 4.3(a) is an average of 10 recorded time traces, while the corresponding measurement for the poly-C Cu foil graphene film in Figure 4.3(b) is an average of 250 recorded time traces. This results in a wider usable spectroscopic bandwidth of 0.15 to 1.5 THz for the poly-C Cu foil graphene data, compared to 0.15 to 1.0 THz for the S-C Cu (111) graphene data.

The conductance spectrum observed for the S-C Cu (111) graphene film shows a real part of the conductance, σ_1, that is slowly decreasing with frequency and an imaginary part of the conductance, σ_2, that slowly increases with frequency. This type of conductance spectrum is consistent with the response of a Drude conductor, which is apparent from the good fit to the Drude model with σ_{DC} = 2.19 mS and τ = 76 fs, shown in Figure 4.3(c). The conductance spectrum that we observe for the poly-C Cu foil graphene film in contrast shows σ_1 and σ_2 that are predominantly flat and constant at values of around 0.73 mS and 0, respectively, in the accessible frequency range. Such a frequency dependent conductivity, $\tilde{\sigma}_s$, can also be described by the Drude model with a scattering rate that is much higher than the accessible frequencies. As a consequence of the very flat spectrum, however, a finite Drude scattering time cannot be inferred from the data obtained for the poly-C Cu foil graphene film, reflecting that the accessible frequency range is much lower than the scattering rate in the graphene film ($2\pi f \ll \Gamma$).

The sheet conductance spectra resulting from the THz-TDS investigation presented here thus strongly indicate that carrier transport in the two CVD graphene films is diffusive and well described within a Drude-type framework, confirming the observations made in other, similar studies of graphene. Based on a Hall mobilities of $\mu_H = 733 \pm 61 \,\mathrm{cm}^2/\mathrm{Vs}$ and $\mu_H = 333 \pm 30 \,\mathrm{cm}^2/\mathrm{Vs}$ for the S-C Cu and poly-C Cu films, respectively, measured using the micro four-point probe Hall effect method[135], an estimated typical Fermi level E_F for CVD graphene of –0.4 eV, and the observation of diffusive Drude-type transport in the graphene film, the carrier diffusivity can be estimated as[136]

$$D = \frac{E_F \sigma_s}{2 n_s e^2} = \frac{E_F \mu}{2e} = 147 \ \mathrm{cm}^2/\mathrm{s}, \tag{4.1}$$

and

$$D = \frac{E_F \sigma_s}{2 n_s e^2} = \frac{E_F \mu}{2e} = 66 \ \mathrm{cm}^2/\mathrm{s}, \tag{4.2}$$

for the two graphene films. The carrier diffusivity allows us to also estimate the characteristic carrier transport length, L, associated with the THz-TDS measurements at frequencies, f, from 0.15 to 1.5 THz. This is evaluated using the expression

$$L = \sqrt{\frac{D}{2\pi f}}, \tag{4.3}$$

resulting in characteristic transport lengths on the order of a few ten to a few hundred nm for both films in the present investigation. The agreement of the obtained conductance spectrum with a Drude model is thus a testament that the graphene film exhibits the traits of an electrically continuous conducting film without e.g. extended defects on the scale of a few ten to a few hundred nm.

Our investigation also indicates a pronounced difference in the extrapolated DC sheet conductance as well as carrier scattering time for the two CVD graphene films, where the S-C Cu graphene film shows a finite scattering time $\tau = 76$ fs in contrast with that of the the poly-C Cu foil graphene film which is too short to be resolved within the experiment bandwidth. The results thus suggest that CVD graphene grown on single-crystalline Cu (111) substrate offers a significantly improved carrier transport.

4.2 Experimental comparison between non-contact THz-TDS and contact-based M4PP conductance measurements

The carrier transport mechanisms in graphene has been extensively studied in countless DC electrical transport experiments, making the DC sheet conductance of graphene a well understood reference quantity to benchmark the validity of graphene sheet conductance measurements by THz-TDS. The extrapolated DC sheet conductance from a Drude fit to THz-TDS measurements is in principle directly comparable to the sheet conductance measured in contact-based DC experiments, given that the assumptions made in the Drude model (homogeneous medium with random, elastic, isotropic scattering events) are valid on the transport length scale of the DC measurement.

4.2.1 Micro four-point probes

In this section the sheet conductance of CVD graphene films measured by THz-TDS is compared to the sheet conductance determined by contact-based DC electrical measurements using micro four-point probes (M4PP). A M4PP is a miniaturized four point-probe, as shown in secondary electron micrograph in Figure 4.4, that facilitates non-invasive four-point van der Pauw measurements of local sheet resistance of thin films with spatial resolution down to approximately 1.5 μm.[137,138]

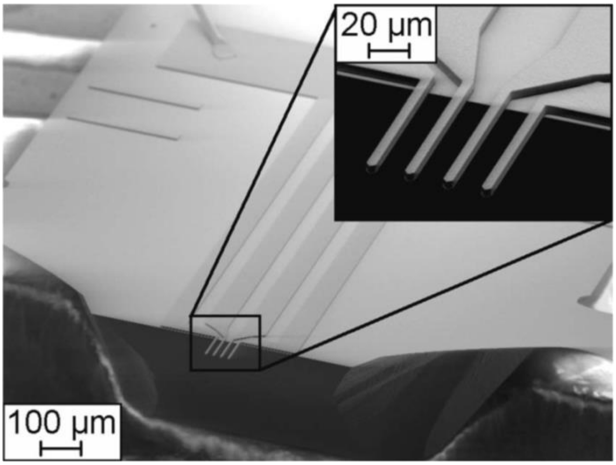

Figure 4.4: Secondary electron micrograph of a micro four-point probe. Reprinted[135]

A four-point probe is a probe with four elongated metal-covered cantilevers, used for making electrical contacts to the sample under investigation. To measure sheet conductance of thin films, a current, I_0, is passed through the thin film between two of the contact points, while a potential difference, V, is measured between the two other contact points. For all M4PP measurements presented in this thesis, the contact points are equidistant with variable electrode pitch, s. The current flowing in the resistive thin film between the current injection contact points results in an electrostatic potential distribution, $\Phi(x,y)$, in the vicinity of the contact points. The DC sheet resistance of a thin conducting film,

$$R_s = \sigma_s^{-1} = \left(e\mu n_s\right)^{-1}, \tag{4.4}$$

can be found from individual measurements of I_0 and V in the 3 independent A, B, and C configurations, illustrated in Figure 4.5, as

$$R_{s,i} = c_i \frac{V_i}{I_{0,i}}, \tag{4.5}$$

where c_i is a correction factor relating to the specific sample and configuration geometry.

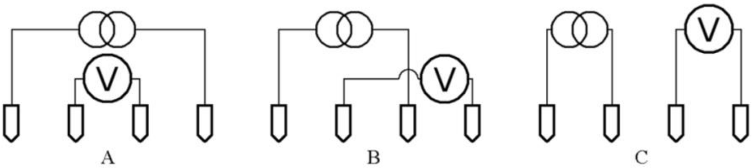

Figure 4.5: Illustration of the 3 independent configurations of contacts for current injection and contacts for probing potential difference without presence of a magnetic field.

For an infinite, uniformly conductive sheet c_i is given as

$$c_i = \frac{1}{2\pi} \ln \frac{|\mathbf{r}_{V-} - \mathbf{r}_{I+}||\mathbf{r}_{V+} - \mathbf{r}_{I-}|}{|\mathbf{r}_{V+} - \mathbf{r}_{I+}||\mathbf{r}_{V-} - \mathbf{r}_{I-}|}, \tag{4.6}$$

where **r** is the position vector of each current and voltage electrode as denoted by the subs. However, determination of the sheet conductance from equations (4.5) and (4.6) may lead to significant errors due to errors in the exact position of the four contacts[138] and due to unknown sample geometry. In the case relevant for the measurement presented in this thesis, where the four contact points are positioned collinearly, R_s may be obtained from two electrode configurations using the van der Pauw equation modified for linear contact configuration[139], with greatly reduced errors due to unknown contact position and sample geometry.

$$\exp\left(\frac{2\pi R_A}{R_s}\right) - \exp\left(\frac{2\pi R_B}{R_s}\right) = 1 \tag{4.7}$$

This technique is known as a dual-configuration M4PP sheet resistance measurement, and is generally the method used for determining sheet conductance with M4PPs in this thesis. For a simply connected infinite sheet, the dual configuration method completely eliminates in-line position errors and greatly reduces measurement errors on small regions with insulating boundaries in proximity of the four electrodes[140]. For an infinite, uniformly conducting sheet, the ratio between configurations A and B is nominally 1.26, as indicated in Figure 4.6, which shows an example of data recorded in a single dual configuration measurement.

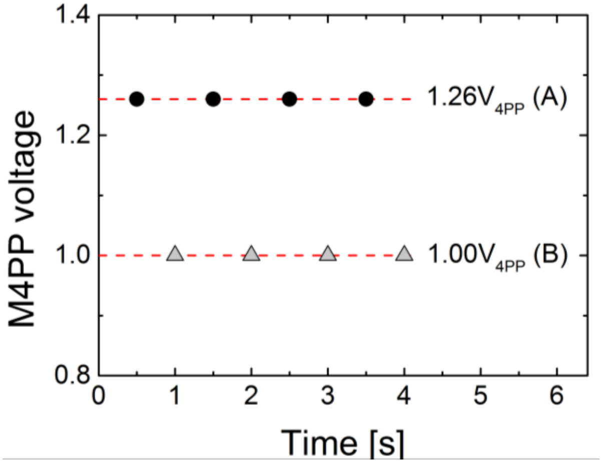

Figure 4.6: Example of the measurement outcome in a dual configuration M4PP sheet resistance measurement. As indicated, the ratio between resistances obtained in the A and B configurations is nominally 1.26 for an infinite, uniformly conducting sheet.

4.2.2 THz-TDS vs M4PP conductance: S-C Cu (111) graphene film

The sheet conductance of the CVD graphene film grown on single-crystalline Cu (111) was mapped by THz-TDS and dual configuration M4PP sheet resistance line scan measurement in 200 µm and in 50 µm steps, respectively, along the dashed line in Figure 4.7(a). The THz sheet conductance values are evaluated as the average real part of the conductance from 0.7 to 0.8 THz, a frequency range which was chosen to obtain the best compromise between a reasonably good spatial resolution of 400 µm and sheet conductance values reasonably close to the DC-extrapolated value. A single reference waveform recorded in a non-graphene-covered area of the HR-Si substrate is used for the evaluation in all positions. For the M4PP line scan, a 12 point-probe with 3 equidistant M4PP configurations of 4, 8 and 12 µm probe pitch as well as 2 equidistant four point-probes with probe pitches of 50 mm and 100 mm, were used to measure the DC sheet conductance at 5 transport lengths. For the THz-TDS conductance measurements the sample was scanned relative to a stationary THz focus, while the M4PPs were moved relative to the stationary sample to form the sheet conductance line scans. The resulting M4PP and THz sheet conductance line scans are shown in Figure 4.7(b).

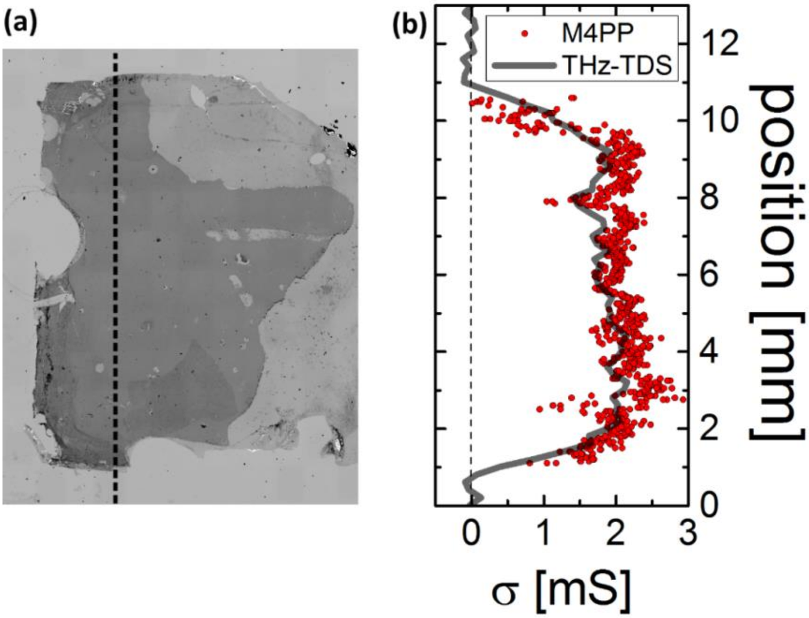

Figure 4.7: (a) Optical micrograph of the CVD graphene film grown on single-crystalline Cu (111). The dashed line indicates the line along which the sheet conductance was mapped by THz-TDS and dual configuration M4PP sheet resistance line scan measurement. (b) M4PP and THz-TDS DC-extrapolated sheet conductance as a function of position along the dashed line in (a).

The sheet conductance measured by THz-TDS and the DC sheet conductance measured by M4PP follow each other very closely, verifying that our THz-TDS measurements are indeed an accurate and reliable non-contact probe of the electrical sheet conductance of graphene films. The THz-TDS thus presents itself as a quantitative, fast and non-invasive method for sheet conductance measurements of graphene films. The slight tendency for the THz sheet conductance to be lower than the M4PP sheet conductance is attributed to the fact that the Drude sheet conductance at 0.7-0.8 THz is slightly lower than the Drude DC sheet conductance. Furthermore, as seen in Figure 4.8(a) where the M4PP DC sheet conductance measurements are plotted explicitly for each probe size, along with the THz-TDS sheet conductance, the M4PP DC measurements using all probe pitches between 4 μm and 100 μm agree well with each other as well as the THz-TDS sheet conductance.

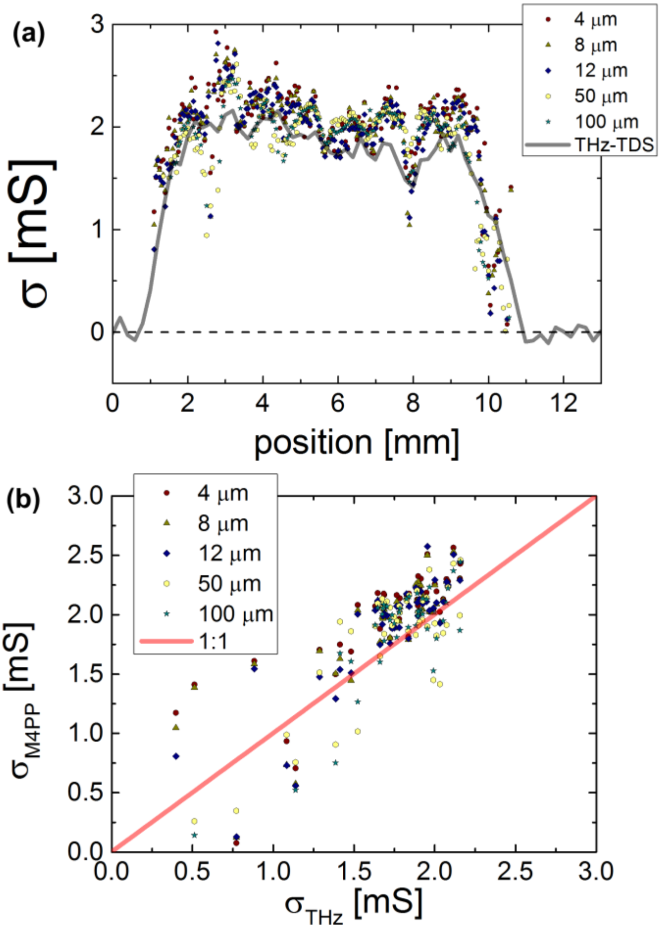

Figure 4.8: (a) Sheet conductance measured by THz-TDS and M4PP with 4, 8, 12, 50, and 100 μm probe pitch as a function of positions. (b) M4PP sheet conductance for various probe pitches plotted against THz-TDS sheet conductance shows an almost perfect 1:1 correlation. The full red line indicates a 1:1 correlation

This is further reflected in Figure 4.8(b), where each measured M4PP sheet conductance value has been plotted against the corresponding measured THz-TDS sheet conductance value in the line scan. The clear clustering of points around a 1:1 correlation testifies to excellent agreement between M4PP and THz-TDS techniques. These measurements thus indicate that the graphene film grown on S-C Cu (111) is electrically continuous from the nanoscale, probed by THz-TDS measurements, to a scale of 100 μm, probed by M4PP measurements.

4.2.3 THz-TDS vs M4PP conductance: poly-C Cu foil graphene film

A comparison of the sheet conductance measured by non-contact THz-TDS to that measured by contact-based M4PP DC measurements is also presented for the graphene film grown on poly-C Cu foil. As indicated in Figure 4.9(a), THz-TDS sheet conductance measurements and M4PP sheet conductance measurements with a single probe pitch of 10 μm were carried out in 146 locations across the graphene film in a similar fashion as that presented in the previous section for the S-C Cu (111) graphene film. In Figure 4.9(a) each measured M4PP sheet conductance value has been plotted against the corresponding measured THz-TDS sheet conductance value, evaluated as the average, real part of the conductance from 1.3 to 1.4 THz. For the poly-C Cu foil graphene film there is a pronounced tendency that the sheet conductance measured by M4PP is lower than that measured by THz-TDS. A reasonable explanation for this is that the graphene film contains pronounced electrical defects on a scale large enough that the THz-TDS experiments are unaffected, while the M4PP sheet conductance is lowered. This phenomenon will be investigated in further detail in chapter 5.

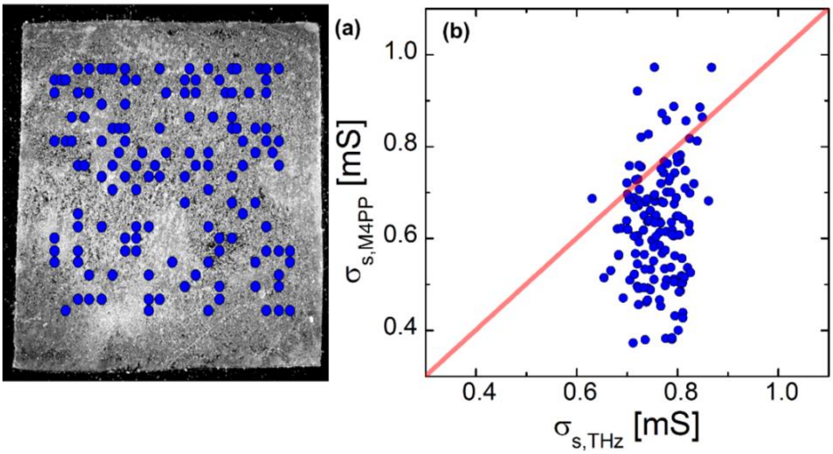

Figure 4.9: (a) Indications of the randomized M4PP sheet conductance measurement locations on the poly-C Cu foil graphene film. (b) Correlation plot showing measured M4PP sheet conductance as a function of measured THz-TDS sheet conductance in the locations on the graphene films indicated in (a). The full red line indicates a 1:1 correlation.

4.3 Carrier nano-localization and preferential back-scattering: Ultra-broadband THz conductance spectroscopy of CVD graphene at 1 to 15 THz

Ultra-broadband THz-TDS based on THz air photonics facilitates accurate experimental determination of the frequency-dependence of both real and imaginary parts of the conductance of graphene films over a wide frequency range. Due to a usable bandwidth of up to 15 THz obtained in the coherent THz-TDS measurements presented here, we are able to resolve real and imaginary parts of close to the entire frequency range associated with intraband optical conductivity of the investigated graphene films.

The CVD graphene samples investigated in sections 4.1 and 4.2 were characterized by ultra-broadband THz air photonics THz-TDS using the experimental setup described in section 3.2. The response of the graphene films is separated from that of the underlying HR-Si substrates by performing sample and reference measurements in graphene-covered and non-graphene-covered areas, respectively. Similar to the THz-TDS investigation in section 4.1, the response of the graphene film grown on single-crystalline Cu (111) is obtained from the directly transmitted THz waveform, while the response of the graphene film grown on poly-crystalline Cu foil is obtained from the 1st roundtrip echo, resulting from multiple internal reflections in the sample. Measuring and analysing the 1st echo increases the contrast between reference and sample measurements and works to improve the overall signal-to-noise ratio of the measurement for graphene films with a low THz response. At multi-THz frequencies, the phase change due to slight variations in the thickness of the HR-Si from sample position to reference position can be significant compared to the phase change induced by the graphene film. As shown in Figure 4.10, it was found that the substrate thickness of a 1 mm thick HR-Si wafer in extreme cases can vary by more than 10 μm across an area of 11.4x11.4 mm^2. The HR-Si thickness in Figure 4.10 was obtained through a fitting routine to the THz waveform in each pixel. In this approach, an input THz time-domain waveform, E_{in}, is first measured with no sample in the THz-TD spectrometer. The Fourier transform, $\tilde{E}_{in}(\omega)$, is computed, from which the directly transmitted pulse and 1st, 2nd, 3rd and 4th echoes are evaluated by the relations

$$\tilde{E}_1 = \tilde{E}_{in}\tilde{t}_{air\to sub}P\tilde{t}_{sub\to air} \tag{4.8}$$

$$\tilde{E}_2 = \tilde{E}_{in}\tilde{t}_{air\to sub}P^3\tilde{r}_{sub\to air}{}^2\tilde{t}_{sub\to air} \tag{4.9}$$

$$\tilde{E}_3 = \tilde{E}_{in}\tilde{t}_{air\to sub}P^5\tilde{r}_{sub\to air}{}^4\tilde{t}_{sub\to air} \tag{4.10}$$

$$\tilde{E}_4 = \tilde{E}_{in}\tilde{t}_{air\to sub}P^7\tilde{r}_{sub\to air}{}^6\tilde{t}_{sub\to air} \tag{4.11}$$

$$\tilde{E}_5 = \tilde{E}_{in}\tilde{t}_{air\to sub}P^9\tilde{r}_{sub\to air}{}^8\tilde{t}_{sub\to air} \tag{4.12}$$

where the Fresnel coefficients $\tilde{t}_{air\to sub}$, $\tilde{t}_{sub\to air}$ and $\tilde{r}_{sub\to air}$ are functions of the refractive index and the propagation factor P is a function of the refractive index and thickness of the substrate, as explained in section 3.3.

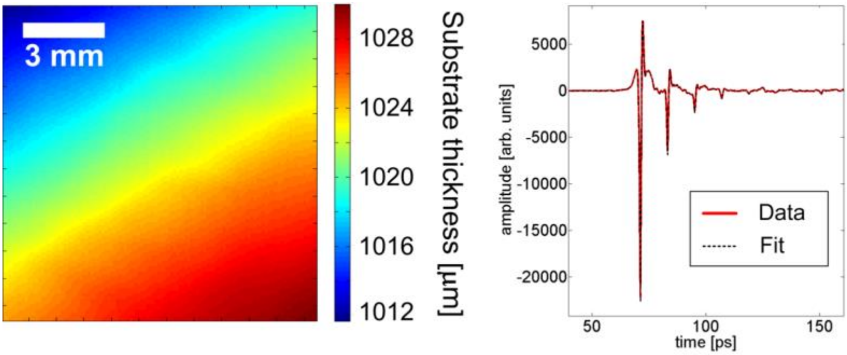

Figure 4.10: The substrate thickness of a 1mm thick HR-Si wafer was mapped with 100 µm step size in an 11.4x11.4 mm^2 area. The substrate thickness was obtained in each pixel of the map by a fitting routine. On the right an example of the outcome of one such fitting procedure is shown.

The output THz time-domain waveform, E_{out}, is then evaluated as the inverse Fourier transform of the superimposed individually calculated Fourier spectra

$$E_{out} = \mathrm{iFFT}\left(\tilde{E}_1 + \tilde{E}_2 + \tilde{E}_3 + \tilde{E}_4 + \tilde{E}_5\right), \tag{4.13}$$

which is fitted to the full transmitted THz time-domain waveform measured in each pixel, with the substrate thickness as the fitting parameter and the refractive index kept constant at n_{Si} = 3.417[133,134]. An example of the result from such a fitting routine is shown in the right panel in Figure 4.10.

Due to the relatively large phase shifts associated with these substrate thickness variations, it was necessary to correct the ultra-broadband THz measurements of the CVD graphene films accordingly. The reference waveform recorded for the S-C Cu (111) graphene film was thus corrected by adding a phase shift corresponding to propagation through 470 nm HR-Si, and the reference waveform recorded for the poly-C Cu foil graphene film was corrected by adding a phase shift corresponding to propagation through 100 nm HR-Si, which were the only values that were found to give meaningful sheet conductance spectra. This is a commonly used procedure, particularly in reflection THz-TDS, which was introduced by Jeon et al[141].

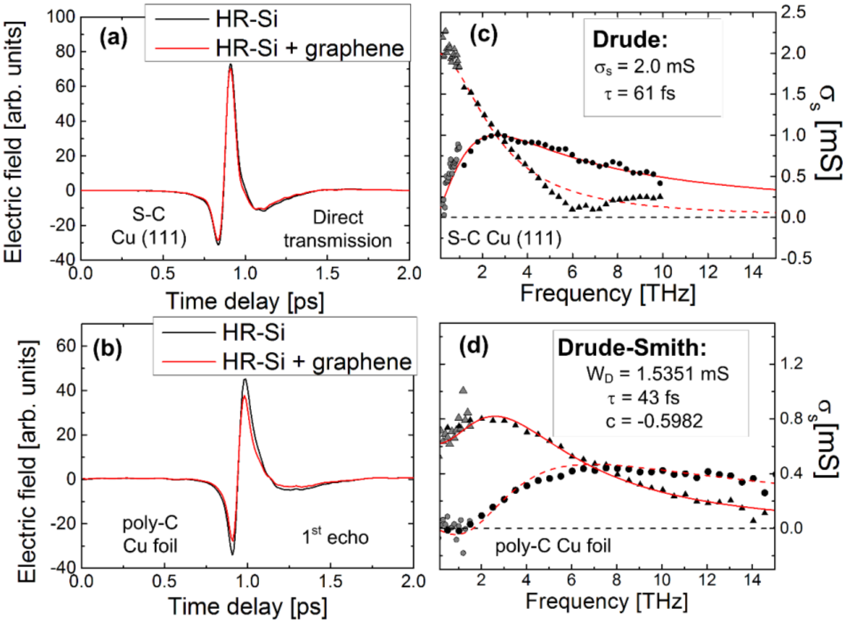

Figure 4.11: Sample and reference THz time-domain waveforms for CVD graphene films grown on (a) single-crystalline Cu (111) substrate (b) poly-crystalline Cu foil. Resulting sheet conductance spectra for (c) single-crystalline Cu (111) substrate (d) poly-crystalline Cu foil.

The resulting sample and reference THz time-domain waveforms for the two CVD graphene films are shown in Figure 4.11(a) and Figure 4.11(b). When analyzed according to the procedures outlined in section 3.3 to obtain the complex, frequency-dependent sheet conductance plotted in Figure 4.11(c) and Figure 4.11(d), we see a very distinct, qualitative difference between the two graphene films. For the case of the CVD graphene grown on single-crystalline Cu (111), the ultra-broadband conductance spectrum agrees very well at low frequencies with that measured by conventional THz-TDS and fits a Drude model with scattering time $\tau = 61$ fs and $\sigma_{DC} = 2.0$ mS, which is similar to the expectation from the analysis based on lower frequency,

]

conventional THz-TDS. Under an assumption of a Fermi velocity of v_F = 10^6 m/s, the measured carrier scattering time translates to a mean free path of

$$l_{mfp} = v_F \tau \simeq 10^6 \text{ m/s} \times 61 \cdot 10^{-15} \text{ s} = 61 \text{ nm}, \tag{4.14}$$

It should be noted that although the graphene Fermi velocity is widely accepted to be close to 10^6 m/s, recent studies have shown that v_F can in certain circumstances differ significantly from this value[142].

Under assumption of carrier transport dominated by long-range charged impurity scattering, the carrier density can subsequently be obtained from the measured σ_{DC} = 2.0 mS as described in section 0.

$$n = \frac{\pi \hbar^2}{e^4 {v_F}^2} \frac{{\sigma_{DC}}^2}{\tau^2} = 5.7 \times 10^{12} \text{ cm}^{-2}, \tag{4.15}$$

using a Fermi velocity $v_F = 10^6 \text{ m/s}$.

In addition, the carrier mobility of the film can subsequently be evaluated as also described in section 0.

$$\mu = \frac{e v_F}{\hbar \sqrt{\pi}} \frac{\tau}{\sqrt{n}} = 2208 \ \frac{\text{cm}^2}{\text{Vs}} \tag{4.16}$$

In the case of the CVD graphene grown on poly-crystalline Cu foil good agreement is also found at low frequencies with the flat conductance spectrum obtained by conventional THz-TDS in the few-THz range. The flat low-frequency conductance spectrum was initially expected to reflect a Drude-type conductance with a very short scattering time. The measured ultra-broadband conductance spectrum reveals, however, that the THz conductance response of this film in fact shows a slight, but distinct suppression of the real conductivity from DC to around 2 THz, accompanied by an imaginary conductivity that goes slightly negative (although very close to 0), which cannot be reproduced by the Drude model.

It is noteworthy that very similar conductance spectra have commonly been observed in nano-disordered, nano-defected or nano-patterned systems such as e.g. semiconductor nano-crystal systems[68–71]. It may therefore provide further understanding to interpret the measured conductance spectrum for the poly-C Cu graphene film in an analogous picture. In the previous studies of disordered semiconductor systems, the suppression of DC and low frequency conductivity reflected localization of charge carriers caused by electronic barriers on a nanoscopic length scale on the order of the characteristic probing length scale of the measurement. This can be thought of as the distance carriers diffuse before the field reverses its direction. As discussed in a previous section, the probing length scale, *L*, in an AC conductivity measurement such as that presented here, is defined through the frequency as $L=\sqrt{D/(2\pi f)}$, where *D* is the diffusion constant and *f* is the frequency. For the present investigation of the poly-C Cu graphene film, the associated probing length scales are on the order of 10-100 nm (8 nm – 84 nm, corresponding to frequencies from 15-0.15 THz, and $D=66\ \mathrm{cm}^2/\mathrm{s}$ based on a measured DC hall mobility $\mu_H=333\pm30\,\mathrm{cm}^2/\mathrm{Vs}$ and an estimated Fermi level of 0.4 eV of the graphene film[136]). Carrier localization by electronic barriers can also be perceived in terms of preferential back-scattering of charge carriers on extended barriers or defects. Preferential back-scattering covers a concept in which the carrier momentum subsequent to a scattering event is more likely to be in directions opposing the incoming carrier momentum direction, which is in contrast to a Drude behavior where carrier momentum direction is completely randomized subsequent to scattering. The impact on the conductance spectrum of preferential back-scattering is modeled in the Drude-Smith model, which is described in section 2.7, by phenomenological introduction of a memory effect to the scattering processes in a framework similar to that of the Drude model[65]. By the back-scattering parameter, *c*, the statistical degree of preferential back-scattering is parameterized in the Drude-Smith model (*c* = 0 describes an isotropic response identical to a Drude response, and decreasing values of *c* < 0 corresponds to higher degrees of preferential back-scattering), resulting in analytical expressions for the frequency-dependence of real and imaginary parts of the conductivity

$$\sigma_{real}(\omega)=\frac{W_D}{\left[1+(\omega\tau)^2\right]^2}\left[1+(\omega\tau)^2+c\left(1+\omega^2\tau^2\right)\right] \tag{4.17}$$

$$\sigma_{imag}(\omega)=\frac{W_D\omega\tau}{\left[1+(\omega\tau)^2\right]^2}\left[1+(\omega\tau)^2+2c\right] \tag{4.18}$$

As shown in Figure 4.11(d) the ultra-broadband THz conductance spectrum is well described by a Drude-Smith model with a Drude weight $W_D = 1.5351\,\mathrm{mS}$, a scattering time τ = 43 fs and a back-scattering coefficient c = -0.5982. In Monte Carlo simulations of the carrier transport in nanoparticle systems, the simulated conductivity spectra were found to follow that predicted by the Drude-Smith model, and the back-scattering parameter *c* was found to correlate with the inter-particle carrier transmission probability at particle boundaries[143]. The back-scattering parameter value of -0.5982 found from the Drude-Smith fit to the poly-C Cu graphene film conductance spectrum therefore might be interpreted as a sign of partial carrier localization on a characteristic scale on an order of between 10-100 nm, corresponding to the probing lengths of the experiment. Likely origins of electronic barriers on this length scale in CVD graphene films include crystal domain boundaries, incomplete growth coverage and transfer-related damages. However, the back-scattering parameter value of c = -0.5982 seems to reflect electronic barriers giving rise to only partial back-scattering of charge carriers. Since incomplete CVD growth as well as transfer-induced rips and fractures are prone to produce physically separated conductive domains, an interpretation of these data within the Drude-Smith picture of nanoscopic localization indicates that the observed conductance features are indeed a signature of carrier back-scattering on crystal domain boundaries in the poly-crystalline CVD graphene film.

Provided that the validity of such an analogy between carrier transport in poly-crystalline graphene and previously examined semiconductor nanoparticle systems holds, the present study provides observations of these types of extended defects specifically impeding the DC carrier transport in CVD graphene relative to the intrinsic Drude-type transport properties limited by point-defect scatterers. To draw final conclusions on this matter, however, further studies of the validity of this analogy are required, e.g. by systematic study of the ultra-broadband THz conductance of graphene films with varying domain sizes and morphology. The observation of transport well described by the Drude model in CVD graphene grown on single-crystalline Cu (111) substrate suggests that the impact of such extended electronic defects is highly dependent on graphene growth and/or transfer methods. In addition, the presented ultra-broadband THz-TDS experiments demonstrate the unique capability of ultra-broadband THz-TDS for accurate, non-contact measurement of fundamental transport parameters such as scattering time τ, mean free path l_{mfp}, carrier density n_s and carrier mobility μ without need for application of gating potentials or magnetic fields.

4.4 Wafer-scale graphene conductance mapping by THz-TDS imaging

For the conductance spectra found in sections 4.1 and 4.3 for CVD graphene films, which are well described by Drude and Drude-Smith models, the real part of the conductance at frequencies much lower than the scattering rate ($2\pi f \ll \Gamma$) is predicted to be close to the value of the DC conductance of the film. In the case of the presently investigated CVD graphene films, this frequency range of a close to constant real conductance spans from DC up to around 1.0 THz. The validity of this prediction was verified in section 4.2 for CVD graphene films grown on high quality, single-crystalline Cu (111) substrates and transferred to SiO_2 covered Si wafers using a 3-electrode electrochemical transfer method(see ref iv, List of Publications).

Based on these observation we present demonstrations of large-area mapping of CVD graphene sheet conductance by THz-TDS imaging, where the sheet conductance, σ_s, is evaluated as the average, real part of the graphene conductance from 0.9-1.0 THz measured as described in sections 4.1 and 0. Figure 4.12(a) and (b) shows an optical microscopy image and a THz sheet conductance map of a CVD graphene film of the same type as that investigated in previous sections, grown on a 1x1 cm^2 single-crystalline Cu (111) substrate.

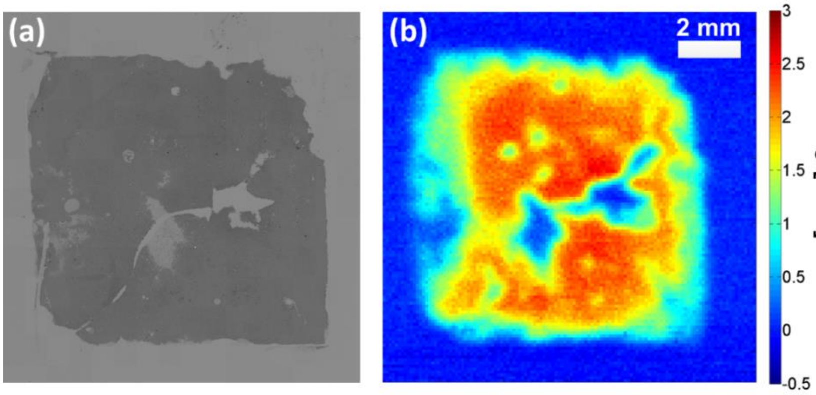

Figure 4.12: (a) Tiled optical microscopy image and (b) THz sheet conductance map of CVD graphene film grown on single-crystalline Cu (111) substrate (average sheet conductance in band from 0.9-1.0 THz).

The THz mapping is carried out using the Picometrix© T-ray™ 4000 system in conjunction with an X-Y scanning stage, which is used to raster scan the graphene/silicon sample in 100 μm steps in the THz focal plane between

THz emitter and detector. Since the spatial resolution of the measurement at 0.9-1.0 THz is approximately 400 μm this results in a significant oversampling of the image. THz time-domain waveforms could thus be recorded in each map of the pixel at an acquisition rate of 100 waveforms/second with no overhead time for mechanical movement owing to the non-contact nature of the THz-TDS technique. The THz sheet conductance map in Figure 4.12 was recorded with 10 waveforms averages in each pixel, resulting in a total acquisition time of 29 minutes. The regions of the graphene film of highest sheet conductance are very similar to that found in the THz-TDS investigations of the previous sections at slightly more than 2.0 mS. The THz sheet conductance replicates the contours apparent in the optical microscopy image but also reveals additional spatial variations in the sheet conductance of the graphene film, in particular towards the outer edges of the film.

As a demonstration of the applicability of THz-TDS imaging towards non-contact, in-line characterisation of graphene electrical properties in an industrial scope, we present the first full wafer-scale non-contact THz-TDS map of the sheet conductance of a 4 inch circular CVD graphene film. The graphene film, which is shown in a tiled optical microscopy image in Figure 4.13(a), was grown on a high-purity Cu film sputtered onto a 4 inch Si/SiO_2 wafer, and subsequently transferred to a 4 inch HR-Si/SiO_2 wafer by electrochemical transfer (see ref iv, List of Publications). The sheet conductance map, which is shown in Figure 4.13(b), was recorded by raster-scanning with a 400 μm step size and averaging of 10 recorded THz waveforms in each pixel, resulting in a total acquisition time of 104 minutes. It should be noted, however, that acquisition rates of 1 waveform/ms in current state-of-the-art THz-TDS imaging equipment makes it technologically feasible to perform a 4-inch wafer mapping with 1 mm resolution in less than 30 seconds. The map in Figure 4.13(b) show significant non-uniformity of the graphene sheet conductance across the wafer, highlighting the importance of tools for characterization of the large-scale uniformity of graphene electrical properties. In addition THz conductance maps recorded for CVD graphene films grown on Cu foil and Cu film deposited onto a 4 inch Si/SiO_2 wafer, respectively, and transferred by sacrificial etching of the Cu layers are shown in Figure 4.13 (c) and (d).

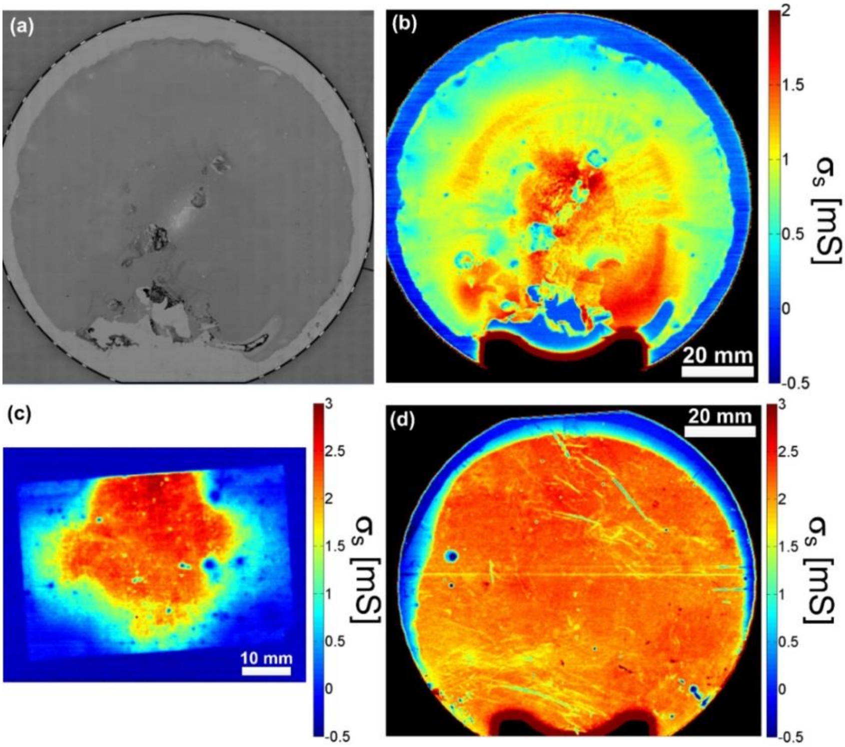

Figure 4.13: (a) Optical microscopy image and (b) THz sheet conductance map of a 4 inch circular CVD graphene film grown on a high purity Cu film sputtered onto a 4 inch Si/SiO_2 wafer. Transferred to HR-Si wafer by electrochemical transfer technique. Average sheet conductance in band from 0.9-1.0 THz. (c) THz sheet conductance map of a 6x4 cm^2 CVD graphene film grown on Cu foil. Transferred to HR-Si by sacrificial etching of Cu foil. Average sheet conductance in band from 0.9-1.0 THz. (graphene film is courtesy of Graphenea Inc.) (d) THz sheet conductance map of a 4 inch circular CVD graphene film grown on Cu foil. Transferred to HR-Si by sacrificial etching of Cu foil. Average sheet conductance in band from 0.9-1.0 THz. (graphene film is courtesy of Graphenea Inc.)

In spite of significant advances in terms of large-area growth of CVD graphene, and a strong motivation for commercial production and implementation of large area graphene for electronic applications such as flexible, transparent electrodes and high frequency RF (radio frequency) electronics, there has been almost no development in methods for direct characterization of electrical properties in graphene on a large scale. In the emerging applications requiring up to square meter dimensions of graphene, rapid, quantitative, contact-free inline characterization of the conductance is of vital importance, and we believe that this demonstration of wafer-scale graphene sheet conductance mapping will help pave the way toward that technologically important goal.

5 Study 2: THz and M4PP large area conductance mapping and correlation – a new light on defects

5.1 Corrections

It should be noted that new insight into the carrier dynamics of one of the graphene films presented in this chapter have been obtained after the time of the presented investigation. A more complete view of the carrier dynamics was facilitated by the ultra-broadband THz-TDS measurements presented in section 3.2. These indicate that in spite of early observations of a frequency-independent conductance response from 0.15-1.5 THz, the conductance of the graphene film is to some extent affected by extended electrical defects on a nanoscopic scale. Some of the conclusions relating to the nanoscopic electrical continuity of the investigated graphene films may therefore be subject to modifications. The investigation in section 4.3, suggests that the DC conductance of the investigated films may be suppressed due to extended electrical defects on the nanoscopic scale. The key conclusion of this chapter, stating that the microscopic DC conductance is reduced relative to the nanoscopic counterpart due to electrical defects on a scale on the order of 10 μm, however, remains unaffected.

5.2 Introduction

After the seminal work on graphene[1,3], its potential use in commercially lucrative technologies has initiated impressive progress in research into graphene-based technologies. Examples of electronic applications include integrated circuits[144], THz bandwidth RF electronics[145] and spintronics[146], and photonic and optoelectronic applications include photovoltaic[55] and light-emitting devices[147], saturable absorbers[148], optical limiters[149], nonlinear frequency conversion[150], and THz devices[151]. In particular, extended areas of single- or few-layer graphene will have a strong, positive impact as transparent conductors in photovoltaic devices and touch-screen devices, with the potential of replacing expensive and scarce materials[152] such as indium tin oxide. The potential use of graphene in this range of important technologies has sparked impressive progress in the number of available techniques for the large-scale synthesis of high-quality graphene in terms of electrical, mechanical and optical properties over large areas[54,57,136,153,154]. However, development of techniques targeting electrical characterization of graphene on a large scale has not kept pace, leaving the rapidly progressing field with inadequate means of assessing the electrical uniformity of synthesized films.

The electrical characterization of large area graphene that takes place today comprises ‘off-line’ transport measurements in lithographically defined structures such as Hall bar devices or time-consuming scanning tunneling microscopy and conductance atomic force microscopy measurements. None of these methods are suitable for high throughput characterization or for investigation of the large-scale uniformity and quality of graphene films with respect to electronic properties.

In recent years it has been shown that THz spectroscopy[155], used extensively to measure frequency-resolved conductance of bulk semiconductors[156] and semiconductor nanostructures[68], is a powerful method for investigating the electronic response of graphene, either in the embodiment of THz Fourier-Transform Infrared Spectroscopy[44] or THz time-domain spectroscopy (THz-TDS)[122–124,127,128], the latter also enabling ultrafast pump-probe investigations of THz conductance. It was also recently shown that the electronic response of single atomic layer of chemical vapor deposited (CVD) graphene can be imaged using THz-TDS[121,157]. Because of the non-contact nature of the THz-TDS technique, mapping of unimpaired electronic properties, which can otherwise be affected by formation of ohmic graphene-metal contact interfaces[158–161], can be carried out without risk of damage, and with a throughput that is orders of magnitude higher than alternative methods. Combined with the very fast data acquisition rates of state-of-the-art THz-TDS systems, this also allows the technique to provide a unique platform for mapping of electrical properties of graphene films on a very large scale, as demonstrated in section 4.4.

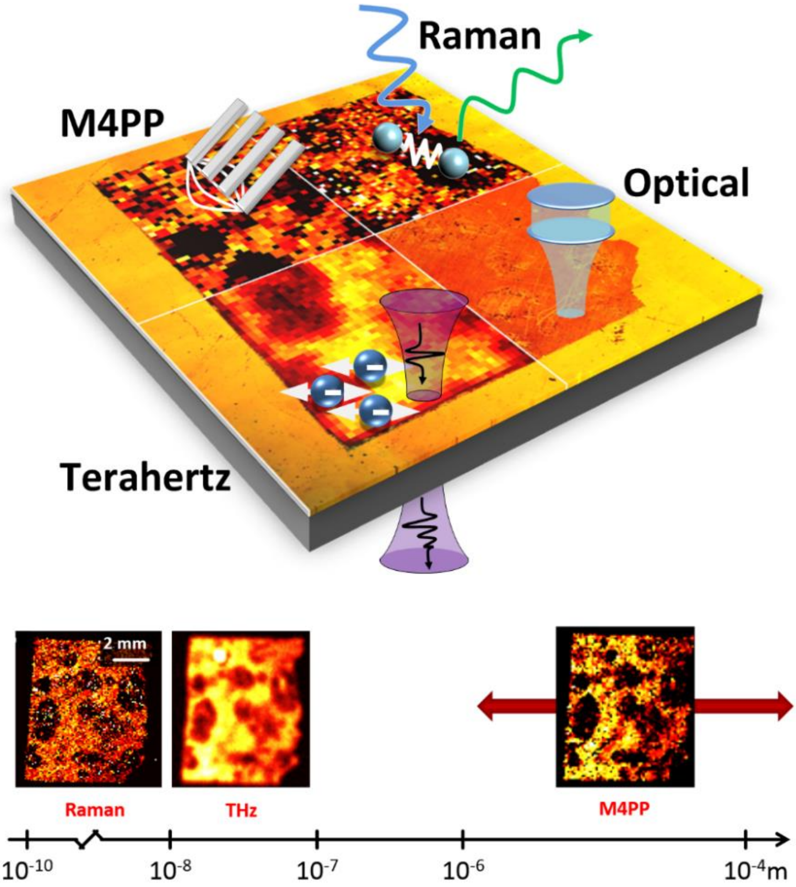

Figure 5.1: Combined THz-TDS, M4PP, Raman and optical mapping of large area graphene on SiO2-on-Si substrate. Sketch depicting the principle of parallel mapping of electrical conductance, Raman response and optical absorption on a single-layer large area graphene film by THz-TDS, M4PP, μ-Raman and optical microscopy. Bottom panel shows the relevant length scales of the physical processes probed by each techniques. The combined information of these techniques facilitates determination of electrical uniformity on nanometer and micrometer length scales and correlation of electrical features to Raman and structural features. The sketch is based on actual data maps.

Similarly, micro four-point probes (M4PP)[137], which were developed for the silicon industry[162] to replace conventional macroscopic four-point probes, van der Pauw technique, and spreading resistance probes because these methods lack reliability[163–168] and spatial resolution[162,169] when applied to advanced semiconductor layered structures, have recently been demonstrated as a tool for non-destructive characterization of graphene sheet conductance[170]. In sections 4.2.2 and 4.2.3, the M4PP technique was also applied for measurement of the microscopic/macroscopic DC conductance of CVD graphene films. For a description of the technique, the reader is referred to section 4.2.1.

In this chapter, a demonstration of correlated M4PP and non-contact THz-TDS measurements for centimeter scale quantitative mapping of the sheet conductance of large-area CVD graphene films is presented. It is shown that dual configuration M4PP measurements provide valuable statistical insight into the influence on the conductance of micro-scale defects, while THz-TDS imaging can probe the influence of nano-scale defects. THz-TDS furthermore has potential as a fast, non-contact metrology method for mapping of the spatially averaged nanoscopic conductance on wafer-scale graphene, with scan times of less than a minute for a 4 inch wafer.

The combination of M4PP and THz-TDS conductance measurements, supported by micro Raman spectroscopy and optical imaging reveals that the film is electrically continuous on the nanoscopic scale, but dominated in its micro-scale conductance by microscopic defects, likely originating from the transfer process. The conductance maps measured by M4PP and THz-TDS agree qualitatively with each other, showing a correlation indicative of the sensitivity of the two techniques towards electrical defects on different length scales, in agreement with the observations made in section 4.2.3. The M4PP measurements probe the microscopic sheet conductance and are particularly sensitive to micro-scale electrical defects in the graphene sheet, while THz-TDS measurements probe the spatially averaged nanoscopic sheet conductance, due to the very high frequency alternating current (AC) electric fields of the THz radiation. Through correlation of M4PP and THz-TDS maps, it is found that microscopic defects, likely originating from the transfer process dominate the micro-scale conductance of the investigated graphene film. Correlations with micro Raman spectroscopy (μ-Raman) maps and optical images of the CVD graphene film support this notion.

5.3 Experimental details

Mapping of the electrical conductance uniformity is carried out by M4PP and non-contact THz-TDS as well as mapping of the Raman response of centimeter scale CVD graphene transferred onto high resistivity silicon ($> 5{,}000\ \Omega \cdot \mathrm{cm}$) substrates covered with 90 nm SiO_2, cf. Figure 5.1(a). Two graphene samples grown by different recipes and transfer processes were investigated.

The first sample (labeled "sample 1" in the following) is the apparently least damaged graphene film, with dimensions of 2x2 cm^2. It was grown in a vertical furnace, where a 25 μm thick copper foil was first annealed in hydrogen at a temperature of 1025^o C and pressure of 0.133 mbar. The growth time was approximately 25 minutes during which the system was maintained at a pressure of 2 mbar and temperature of 1025 ^oC, with a methane flow of 2 standard cubic centimeters per minute (sccm) and a hydrogen flow of 0.5 sccm. These parameters are similar to previously reported conditions for monolayer graphene growth[24,54]. The grown graphene film was then transferred to a high resistivity silicon wafer by slow etching the copper foil in a solution of 0.1M ammonium persulfate ($(NH_4)_2S_2O_8$) with a thin supporting polymethylmethacrylate (PMMA) layer. The PMMA was subsequently removed in acetone.

The second sample (labeled "sample 2") is a 6×7 mm graphene film with distinct optically visible damages. It was grown in a cold-wall CVD system using pre-diluted CH_4 (5% in Ar) as carbon precursor. The deposition temperature was nominally 1000^o C and the growth time was 5 min. H_2 and Ar were used as auxiliary gases, where the partial pressure of CH_4 was kept very low (<0.01 mbar) to suppress the formation of multilayer flakes and enhance the quality and domain size of the graphene. More details about this CVD procedure are reported elsewhere[171–173]. The as-deposited graphene was subsequently transferred onto high resistivity silicon by a standard wet transfer process using PMMA as mechanical support and a dilute, aqueous HNO_3 solution to etch the copper film[54,171]. Finally, the polymer was removed by acetone.

The Raman response of the samples was mapped using a Thermo Fisher Scientific DXR μ-Raman microscope with a 532 nm excitation laser and a 2 μm spotsize. Spatial maps of the samples were produced with 200 μm and 75 μm lateral resolution for sample 1 and sample 2, respectively, providing spectroscopic information between 1100 and 3000 cm^{-1} (1 cm^{-1} resolution) in each pixel. The Raman maps are used as qualitative indicators of sample quality, areal coverage, strain and doping level. The resolution of the Raman maps is chosen as a realistic compromise between image quality and total data acquisition time (10-12 hours per mapping). Representative Raman spectra for the two CVD graphene samples, showing distinct D, G and 2D peaks, corresponding to single layer graphene with some indication of crystal defects are shown in Figure 5.2. For descriptions of common interpretations of the individual Raman bands, see section 2.2.

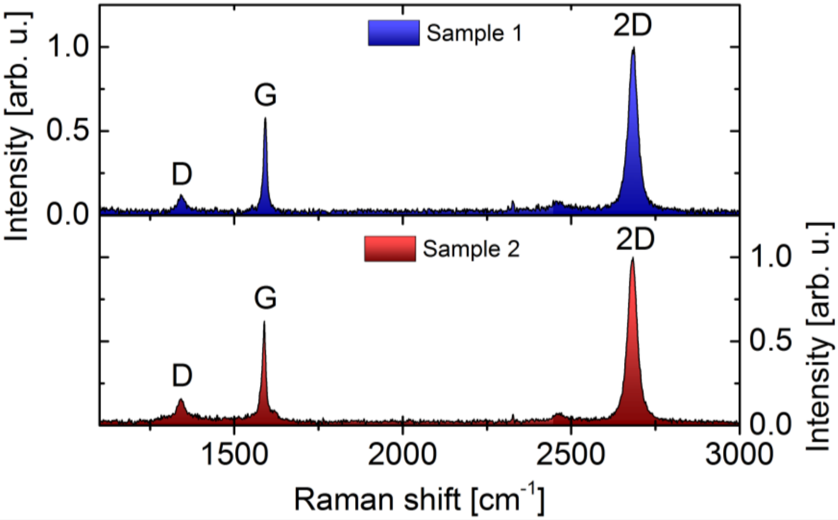

Figure 5.2: Representative Raman spectra for the two investigated CVD graphene samples.

M4PP mapping with up to 4000 individual measurements per sample was performed on a semi-automatic CAPRES MicroRsP-M150 scanner using a set current of 1 µA and lock-in technique (11 Hz). The dual configuration van der Pauw method[174] adapted to collinear four-point probes[139] was used, providing far higher accuracy and lower variability than a standard four-point measurement. The dual configuration technique is described in section 4.2.1. The set current of 1 µA has been shown not to lead to sample damage, since it is significantly below the previously observed damage threshold of approximately 100 µA[170]. The surface was detected using an integrated strain gauge cantilever sensor[175], and the cantilever electrodes were engaged to a nominal depth of 500 nm with a corresponding contact force of approximately 10 µN for each electrode. M4PP sheet conductance mapping was performed with an electrode pitch of 10 µm and a step size of 100 µm. To rule out potential time dependent sheet conductance variations, the measurement position chronology was randomized. Additional single approach measurements were performed with electrode pitches ranging from 3 µm to 59 µm.

THz sheet conductance maps were produced from THz-TDS data recorded using a Picometrix T-ray 4000 fiber-coupled spectrometer with an integrated X-Y scanning stage, as described in section 3.1. The samples were raster scanned in 100 um steps in the x-y direction of the focal plane between the fiber coupled emitter and detector units to form spatial maps. Partial internal reflections from the SiO_2-air interface in the substrate lead to a reflected signal that consists of multiple, periodic echoes with a temporal spacing given by the time-of-flight through the substrate, as outlined in section 3.3. Time windowing and subsequent Fourier transformation gives access to the amplitude and phase of the frequency content of each of the echoes $\tilde{E}_{out,1}(\omega), \tilde{E}_{out,2}(\omega), \ldots$ for every pixel in the map. As in the investigation in chapter 4, an analysis relying on the 2nd transmitted pulse was applied, as this was found to be the optimum trade-off between graphene signal magnitude and noise level for these films.

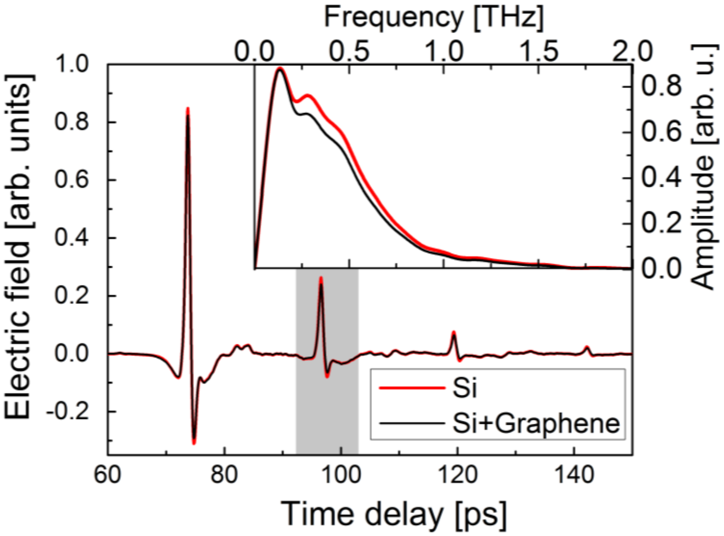

Figure 5.3: Example of THz-TDS time-domain data showing multiple echoes from partial internal reflections in the SiO_2-on-Si sample substrate. Sheet conductance extraction is based on the Fourier transform (FFT amplitude shown in inset) of the time-windowed 2nd transmitted pulse, E_2 (indicated by gray shading), for areas with (black line) and without (red line) graphene on the surface of the wafer.

Figure 5.3 shows an example of the transmitted train of THz pulses in the time-domain and the applied time-window indicated by gray shading, as well as the frequency-dependent amplitude of the time-windowed pulse,

$\tilde{E}_{out,2}(\omega)$, recorded at a pixel covered graphene and a pixel without graphene. Through an analysis of the Fresnel coefficients for the sample geometry, where the graphene film is modeled as an infinitely thin conducting film, the complex sheet conductance, $\tilde{\sigma}_s(\omega)$, is related to the complex transmission function, $\tilde{T}(\omega) = \tilde{E}_{out,2,G}(\omega) / \tilde{E}_{out,2,Si}(\omega)$, of the second transmitted pulses for areas with and without graphene coverage, as described in section 3.3.

$$\tilde{\sigma}_s(\omega) = \frac{\pm n_A\sqrt{n_A^2 + 4n_An_B\tilde{T}(\omega) + 4n_B^2\tilde{T}(\omega)} - n_A^2 - 2n_An_B^2\tilde{T}(\omega)}{2n_BZ_0\tilde{T}(\omega)}, \quad (5.1)$$

where $n_A = n_{Si}+1, n_B = n_{Si}-1$, $n_{Si} = 3.42$ is the refractive index of silicon and Z_0=377 Ω is the vacuum impedance. Examples of $\tilde{E}_{out,2,G}(\omega)$ and $\tilde{E}_{out,2,Si}(\omega)$ are shown in Figure 5.3.

The average of 250 subsequent time-domain traces were formed for the imaging, facilitating unambiguous determination of $\tilde{\sigma}_s(\omega)$ with reliable spectroscopic information in the frequency range 0.15-1.5 THz[176] for each pixel. For additional details on the THz-TDS experiments, the reader is referred to sections 3.1 and 3.3 .

5.4 AC and DC graphene conductance mapping

Figure 5.4(a) shows examples of the extracted THz conductance spectrum measured in the central regions of the two samples under investigation. $\tilde{\sigma}_s(\omega)$ is rather constant across the entire measurable frequency range of 0.15-1.5 THz in agreement with previous THz-TDS investigations of conductance in synthesized graphene, which have shown similar THz responses that are well described by the Drude model[44,123].

Careful edge-scan experiments, providing the FWHM of the THz beam as a function of frequency, shown in Figure 5.4(b), have revealed that the observed drop in THz sheet conductance at the low end of the spectrum is caused by the low frequency parts of the THz spot extending outside the area with uniform graphene coverage. This is sketched in the inset of Figure

5.4(a). The small peak observed at 1.1 THz in Re(σ_s) is an artifact caused by the water absorption line of ambient air.

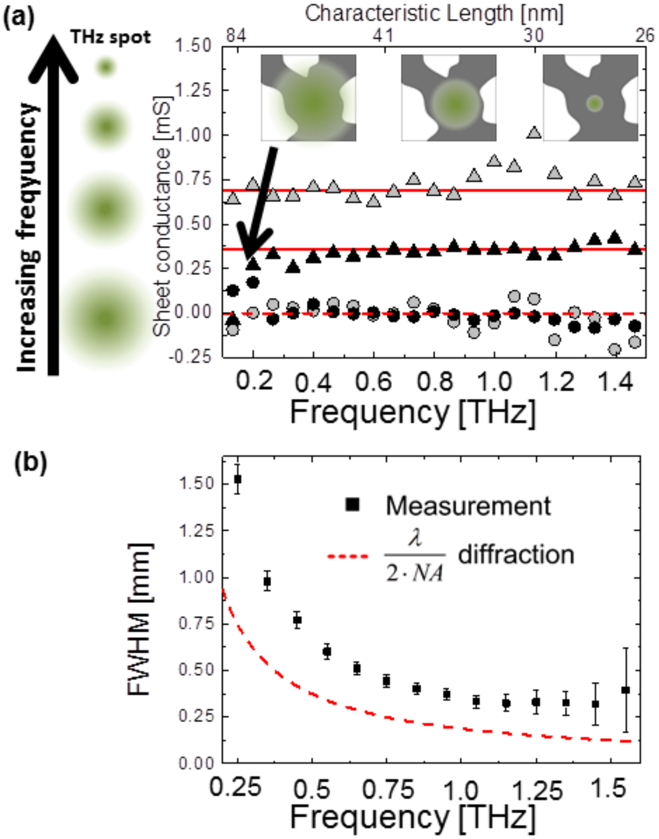

Figure 5.4: (a) Spectrally resolved sheet conductance of the two graphene films, measured by THz-TDS. Characteristic length scales are based on an estimated diffusion constant of *D* = 66 cm^2/s. Triangles represent Re(σ_s) and circles represent Im(σ_s). The spectra are obtained in the center of Figure 5.5(a) (sample 1, light grey) and in the central conducting part of Figure 5.7(b) (sample 2, black). The full red lines indicate the average real sheet conductances of the two samples, while the dashed red lines indicates the zero-value of the negligible imaginary sheet conductances of the two samples. The observed drop in THz sheet conductance at the low end of the spectrum for sample 2 is caused by the low frequency parts of the THz spot extending outside the area with uniform graphene coverage, as indicated in the inset, and the small peak observed at 1.1 THz in Re(σ_s) is an artifact caused by the water vapour absorption line of ambient air. The indicated characteristic length scale is discussed in the text. (b) Measured FWHM of the THz beam as a function of frequency.

For frequencies significantly below the inverse scattering time ($2\pi f << 1/\tau$) the Drude model dictates that the real part of $\tilde{\sigma}_s(\omega)$ is constant and near its DC value while the imaginary part is close to zero. The spectrally resolved

THz-TDS conductance measurement can thus be replaced by a single, real-valued quantity which can be compared directly to DC sheet conductance value as determined by M4PP measurements. In the sheet conductance mappings the THz-frequency conductance is represented by its average value in the region 1.3-1.4 THz as this range offers the optimum trade-off between the obtainable spatial resolution and signal-to-noise ratio of the measurements. With increased bandwidth, the THz-TDS technique also allows determination of the Drude carrier scattering time through fitting of the characteristic Drude model to the spectrum, as shown in chapter 0. Figure 5.4(b) shows the full-width-at-half-maximum (FWHM) of the THz beam as a function of frequency, inferred from the average rise distance of the THz amplitude response on the left edge of the graphene film in Figure 5.5. These measurements show that the THz spot diameter is approximately 0.32 mm FWHM in the 1.3-1.4 THz frequency range. This results in some blurring, as variations on a smaller length scale are not accurately reproduced.

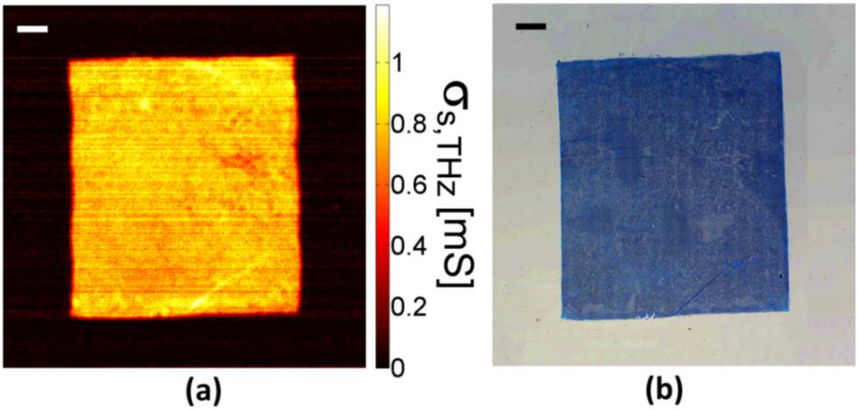

Figure 5.5: Images of homogeneous CVD grown graphene film on 90 nm SiO2 on Si (sample 1). Scale bars are 2 mm. (a) THz sheet conductance map. Average sheet conductance in 1.3-1.4 THz band. (b) Tiled optical microscope image.

Figure 5.5(a) shows direct mapping of the magnitude and uniformity of $\sigma_{s,THz}$ at 1.3-1.4 THz recorded by THz-TDS across the CVD graphene film with dimensions of approximately 2 x 2 cm^2 (sample 1), revealing an electrically homogeneous film. The Raman maps of the graphene film are fairly homogeneous, as shown in Figure 5.6, with the exception of one region of spectral redshift of the Raman D, G and 2D peaks, as shown in Figure 5.6(d), (e) and (f). This type of redshift is commonly interpreted as an indicator of local strain in the graphene film[24]. This strain does not seem to have a significant influence on $\sigma_{s,THz}$ of this particular graphene film, however, as the feature is not reproduced in the THz sheet conductance map in Figure 5.5(a).

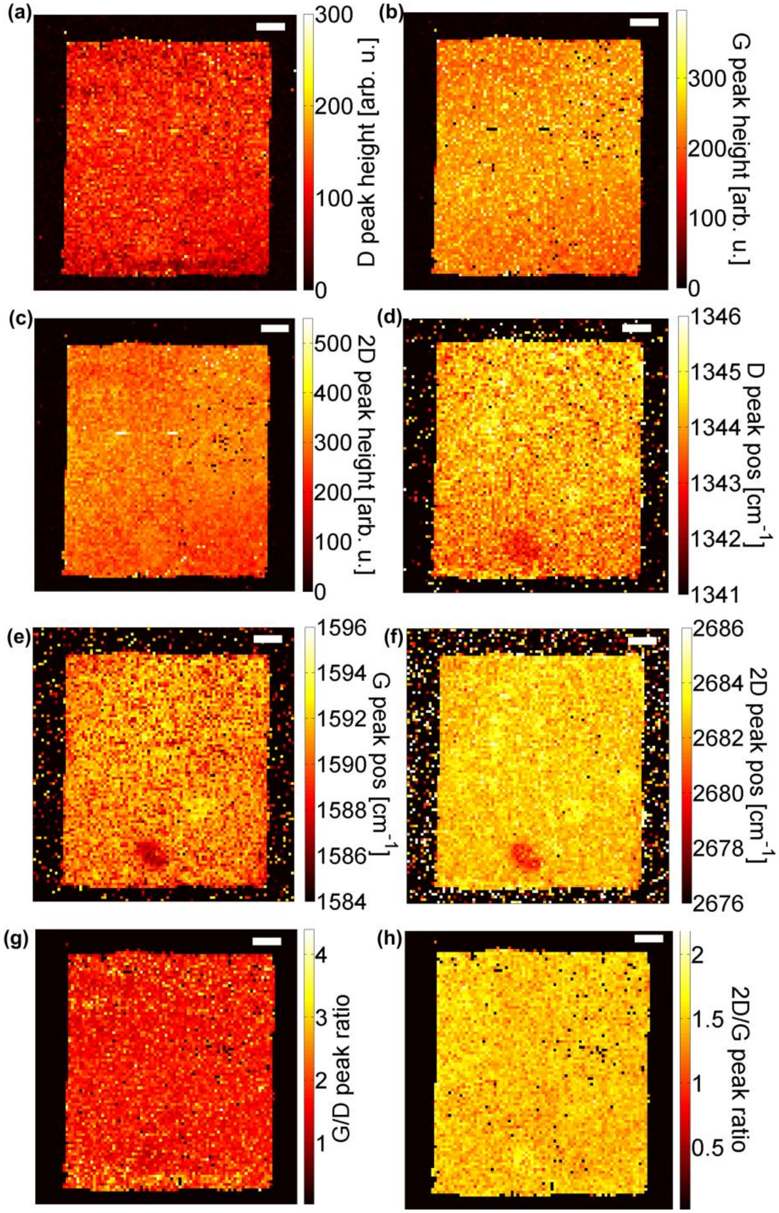

Figure 5.6: μ-Raman maps of homogeneous CVD grown graphene film on 90 nm SiO2 on Si (sample 1). Scale bars are 2 mm. (a) D peak height (b) G peak height (c) 2D peak height (d) D peak spectral position (e) G peak spectral position (f) 2D peak spectral position (g) G/D peak amplitude ratio (h) 2D/G peak amplitude ratio.

M4PP measurements carried out at 146 locations distributed throughout the sample 1 film show a mean sheet conductance of $\sigma_{s,\mathrm{M4PP}} = (0.64 \pm 0.13)\ \mathrm{mS}$. In comparison, THz-TDS measurements, extracted from the map shown in Figure 5.5(a), show an average sheet conductance of $\sigma_{s,\mathrm{THz}} = (0.768 \pm 0.077)\ \mathrm{mS}$ at 1.3-1.4 THz. With a measured relative standard deviation in repeatability of 3%, the large variation (20%) in sheet conductance measured with M4PP, as well as the discrepancy between $\sigma_{s,\mathrm{M4PP}}$ and $\sigma_{s,\mathrm{THz}}$ mean values might be explained by micron-scale defects and non-uniformity primarily affecting M4PP conductance. The measured sheet conductances (0.432 to 1.174 mS for THz - 0.248 to 0.973 mS for M4PP) correspond to between roughly 1.5 and 8 times the minimum DC conductance of graphene of $\sigma_{\min} = 0.154\ \mathrm{mS}$ found by Novoselov and co-workers[2], illustrating that both techniques reveal realistic graphene sheet conductances of comparable magnitude. While transport measurements[2] tend to yield $\sigma_{\min} = 4e^2/h = 0.154\ \mathrm{mS}$ or higher[32], theoretical papers[27] as well as optical spectroscopic investigations in the infrared[126,177] and visible[178], agree on a lower value of $\sigma_{\min} = e^2/4\hbar = 0.061\ \mathrm{mS}$.

As an example of a measurement revealing significantly larger spatial variation, σ_s was mapped across sample 2, a 6 x 7 mm CVD graphene film with distinct, optically visible inhomogeneities shown in Figure 5.7(a), by THz-TDS and M4PP techniques. The THz-TDS and M4PP sheet conductance maps are shown in Figure 5.7(b) and (c). The THz and M4PP sheet conductance maps are in good qualitative agreement, with the exception of a bright spot in the upper left corner of the THz image. This feature likely reflects a strongly scattering particle of high dielectric contrast, possibly a small grain of residual copper. As shown in Figure 5.7(d), convolution of the M4PP data with a 2D Gaussian profile of FWHM=0.32 mm, matching the THz spot size, reproduces most features of the THz image. It however also gives the first indications that the overall M4PP sheet conductance of sample 2 is significantly lower than the THz sheet conductance, as will be discussed in detail in the next section. A comparison of THz and M4PP maps with spatially resolved μ-Raman measurements, shown in Figure 5.8, reveals a strong spatial correlation, most prominent between σ_s and the Raman G and 2D peak heights, which follow each other closely.

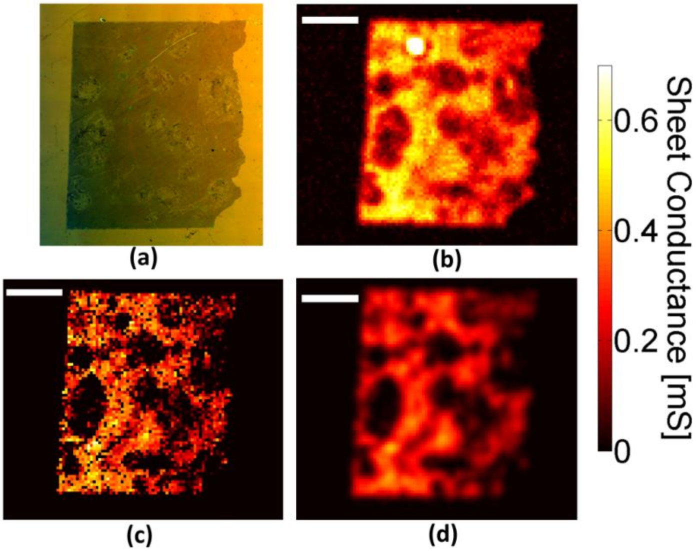

Figure 5.7: Images of a damaged CVD graphene film on 90 nm SiO2 on Si. Scale bars are 2mm. (a) Tiled optical microscope image, (b) THz sheet conductance image (1.3-1.4 THz), (c) M4PP sheet conductance map, (d) M4PP sheet conductance map convoluted with a 2D Gaussian profile of FWHM=0.32mm.

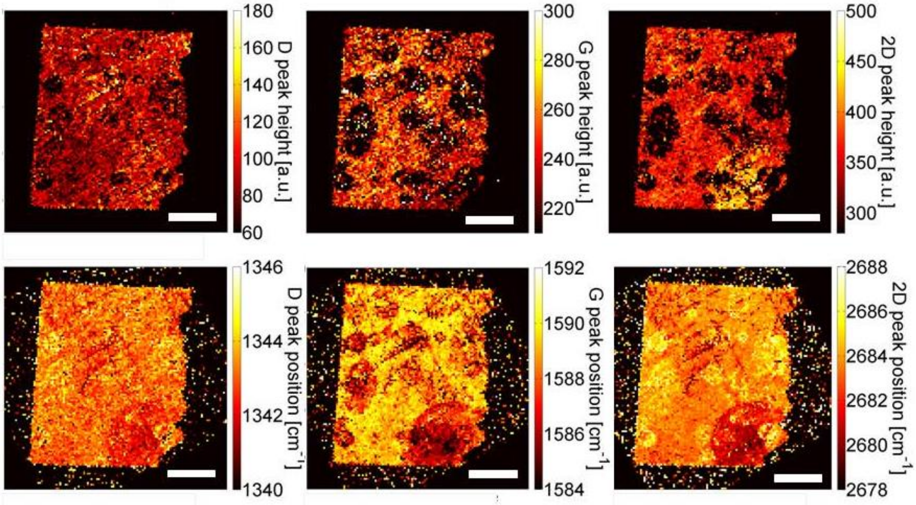

Figure 5.8: μ-Raman maps of inhomogeneous CVD grown graphene film on 90 nm SiO2 on Si (sample 2). Scale bars are 2 mm. (a) D peak height (b) G peak height (c) 2D peak height (d) D peak spectral position (e) G peak spectral position (f) 2D peak spectral position.

Correlated variations in the G and 2D peak heights most likely reflect variations in the local graphene areal coverage, indicating that the THz-TDS and M4PP conductance of this graphene film is mainly influenced by the local density of rips and defects induced by the transfer or by incomplete growth coverage. Other parameters identifiable by μ-Raman analysis, such as atomic defects, doping level and strain seem to be of secondary importance. There are also spatial features in the measured sheet conductance that are not reflected in the μ-Raman data, showing that direct sheet conductance mapping of CVD graphene films provide valuable additional information about sheet conductance uniformity that cannot be inferred from Raman analysis.

5.5 New light on electrical defects: Correlating THz and DC conductivity

A quantitative correlation analysis between THz and M4PP images of sample 2 (Figure 5.7(b) and (c)) is shown in Figure 5.9(a) and (b), where the corresponding values for $\sigma_{\mathrm{s,M4PP}}$ and $\sigma_{\mathrm{s,THz}}$ have been plotted against each other for all pixels where the M4PP measurement yielded a finite and non-zero conductance.

The subset of points with $\Gamma = \sigma_{s,M4PP}/\sigma_{s,THz} > 1.1$, shown with red dots in Figure 5.9(a) and (b), is related to a lowering of the measured $\sigma_{\mathrm{s,THz}}$ near edges of the film due to spot size blurring. If the measurements caused by this edge effect are ignored, it is evident that there is a tendency for the M4PP sheet conductance to be lower than that measured by THz-TDS. Although based on a smaller measurement population, the same tendency is observed in the correlation plot of THz and M4PP measurement from sample 1, shown in Figure 5.9(a). As will be discussed below, this behavior stems from the different ways in which THz and M4PP measurements are affected by micron-scale defects such as rips, wrinkles (transfer defects) and domain boundaries (growth defects) in the graphene film.

The M4PP conductance measurement probes carrier transport on the scale of the 10 μm electrode pitch, and is therefore very sensitive to microscopic defects. Rip-like defects or domain boundaries smaller than the electrode pitch of 10 μm may substantially decrease the measured $\sigma_{s,M4PP}$, even by orders of magnitude, compared to the case of a defect-free sheet[179,180]. Also insulating rips or boundaries of dimensions similar to the electrode pitch can in the worst case result in an underestimation of the sheet conductance by up to a factor of two[140]. The presence of a high density of defects of dimensions similar to the electrode pitch is indeed indicated in the graphene sample under investigation by the observed distribution of measured four-point probe resistance ratios, R_A/R_B (A and B configurations shown in insets of Figure 5.10).

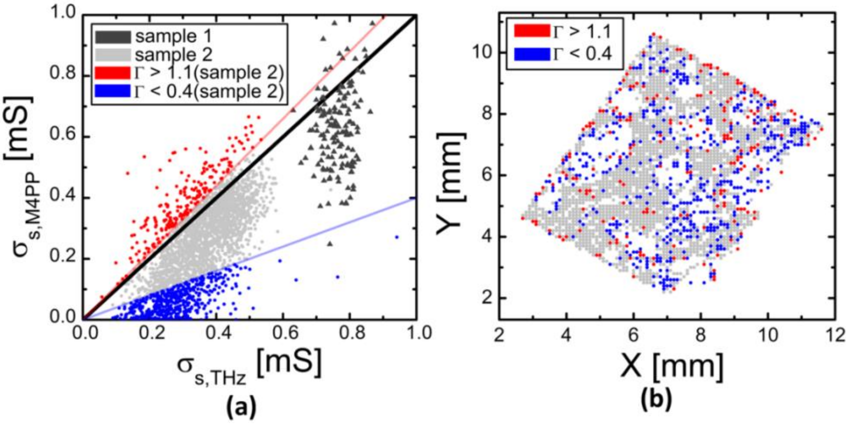

Figure 5.9: THz/M4PP correlation analysis. (a) Correlation diagram of THz and M4PP sheet conductance measurements for sample 1(dark gray triangles) and sample 2(light gray, blue and red circles). The full black line indicates 1:1 correlation. (b) Sample map showing pixel positions of correlation data for sample 2. In (a) and (b), the data subset with $\Gamma = \sigma_{s,M4PP}/\ \sigma_{s,THz} > 1.1$ is plotted as red dots and the data subset with $\Gamma = \sigma_{s,M4PP}/\ \sigma_{s,THz} < 0.4$ is plotted as blue dots. The red dots tend to cluster near the edges of the sample, while the blue dots dominate areas with large holes and other distinct visible transfer damages.

For the case of a continuous conductive sheet (2D conductance), a distribution of resistance ratios will result from variations in the absolute electrode positions, with a peak centered at $R_A/R_B = \ln(4)/\ln(3) \approx 1.26$, cf. Monte Carlo (MC) simulations based on analytical calculation of the resistance ratio as function of Monte Carlo displacement of electrodes from their ideal positions[181]. In contrast to a continuous conductive sheet, the measured R_A/R_B distribution, shown in Figure 5.10, displays features testifying that the graphene film cannot be assumed to be a simply connected conducting sheet on the scale of the electrode pitch. The narrow peak at $R_A/R_B = 1.00$ is a distinctive trait of electrically conductive wire-like structures (1D conductance) or otherwise highly confined structures on the scale of the electrode pitch, whereas the broader distribution centered on approx. $R_A/R_B = 1.15$ indicates a defected, electrically discontinuous, conductive film, containing multiple insulating boundaries of dimensions similar to the electrode pitch in proximity of the four electrodes, as also seen for small samples[140].

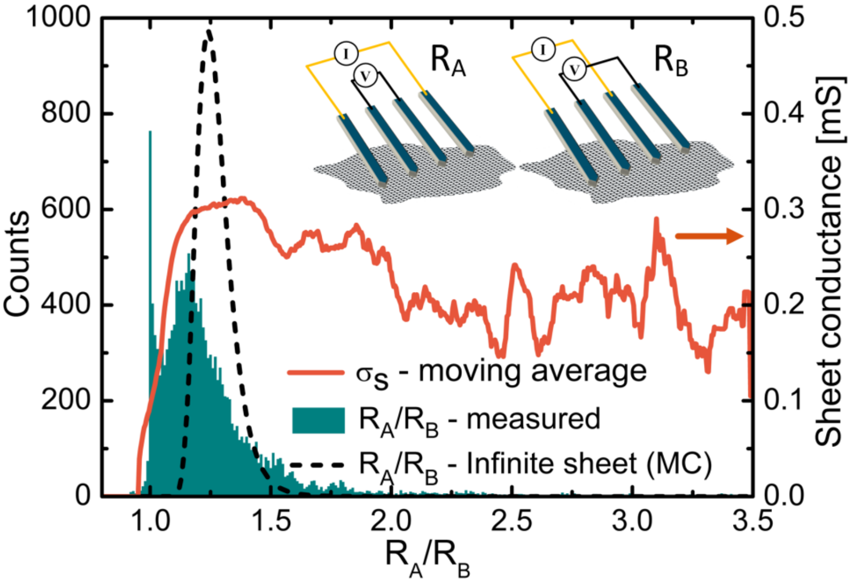

Figure 5.10: Distribution of measured resistance ratio R_A/R_B in the dual configuration M4PP map shown in Figure 5.7(c) (turquoise bars), Monte Carlo simulation of R_A/R_B distribution for an infinite, continuous conducting sheet with 500 nm normal distributed electrode position errors (dashed, black line) and running average of the measured dual configuration sheet conductance as a function of R_A/R_B (full, orange curve).

From the behavior of the orange curve in Figure 5.10, calculated as the running average of the $\sigma_{s,M4PP}$ values, it is also apparent that the M4PP sheet conductance shows a distinct drop in magnitude for the measurements with R_A/R_B close to 1.00, indicating that this type of defect is associated with severely degraded micro-scale conductance. More specifically, measurements with variable electrode pitch, shown in Figure 5.11, indicate that in a region with very low conductance, the R_A/R_B ratio approaches 1.00 and the conductance exhibits an increase for smaller electrode pitches (3 and 6 µm), as seen in Figure 5.12, while no significant dependence on electrode pitch appears in a region of high conductance, where the measured R_A/R_B ratio is also closer to the ideal 2D case. This is in good agreement with an interpretation that the M4PP sheet conductance is dominated by a high density of defects on the scale of the electrode pitch, and that this shows up as regions with laterally constricted or even wire-like conductance behavior.

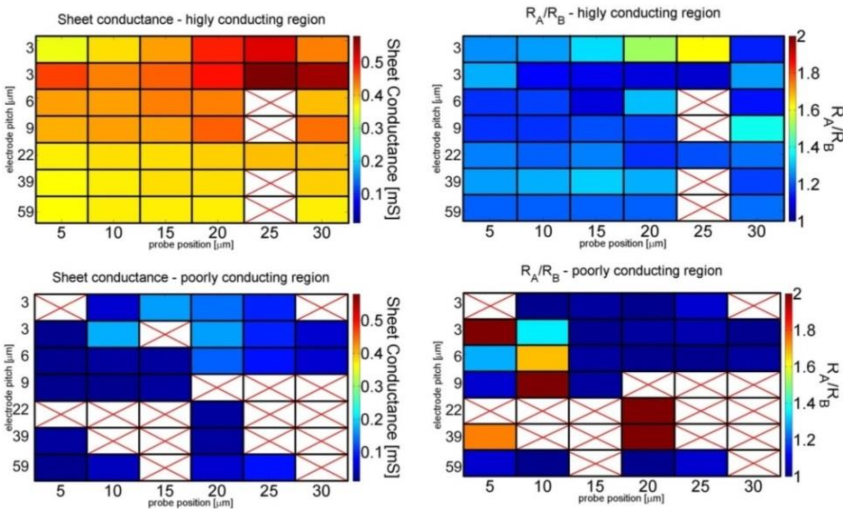

Figure 5.11: M4PP dual configuration sheet conductance and R_A/R_B values for different electrode pitches and positions along two line-scans in a highly conducting region and a poorly conducting region on 'sample 2'. The data is recorded with a 12 point probe, facilitating 7 different equidistant M4PP configurations, in 6 engages with 5 µm spacing.

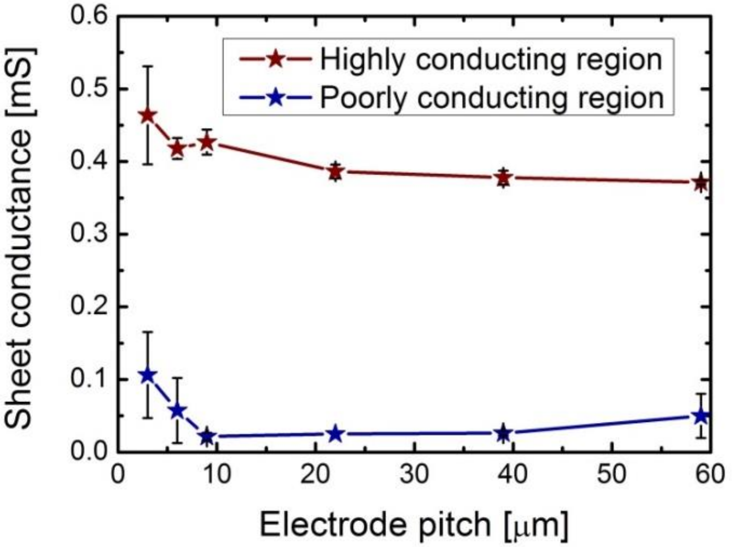

Figure 5.12: average M4PP dual configuration sheet conductance of 6 engages as a function of electrode pitch for a highly conducting region and a poorly conducting region on 'sample 2'

Due to its AC nature, THz-TDS in contrast to M4PP probes carrier transport at a characteristic length scale given by the probing frequency and the material diffusion constant[67,136]. Under the assumption of a diffusive transport regime, this characteristic length scale can be estimated as

$$L = \sqrt{\frac{D}{2\pi f}}\ , \tag{5.2}$$

$$D = \frac{E_F \sigma_s}{2 n_s e^2} = \frac{E_F \mu}{2e}\ , \tag{5.3}$$

where L is the characteristic length scale, D is the diffusion constant, f is the frequency, E_F is the Fermi level, n_s is the carrier density, e is the elementary charge, σ_s is the sheet conductance and μ is the carrier mobility. L is on the order of 10^{-8} to 10^{-7} m (approximately 84 nm and 26 nm at 0.15 and 1.5 THz, respectively, as indicated in Figure 5.4) for an estimated D = (66±15) $\mathrm{cm^2/s}$ (corresponding to a Hall mobility of $\mu = (3.3 \pm 0.7)\cdot 10^2\ \mathrm{cm^2/Vs}$ measured in a high conductance area and thus an estimated Fermi level of $E_F = (0.40 \pm 0.04)\ \mathrm{eV}$). This means that the measured THz conductance reflects the spatially averaged nanoscopic conductance of the graphene film, and is thus far less affected by the microscopic defects found to greatly affect the M4PP conductance of this graphene film. The THz conductance is, however, highly sensitive to defects on the nanoscopic scale. The THz conductance spectrum for sample 2, shown in Figure 5.4(a), which displays no significant frequency dependence is an indication of an electrically homogeneous and continuous film on the scale from a few tens of nm to around a hundred nm.

The behavior of the graphene film as a continuous sheet on the nanoscopic probing length scale of THz conductance measurements in contrast to its behavior as a highly defected sheet on the microscopic transport length scale of the M4PP conductance measurements is the most obvious explanation for the discrepancy between THz-TDS and M4PP sheet conductance values. These two results in combination suggest that this sample is electrically continuous on the few tens to around a hundred nanometer length scale while dominated in its micro-scale electrical response by a high density of insulating defects of dimensions similar to the M4PP electrode pitch of 10 μm. The origin of such insulating micro-scale defects could be damage occurring during the transfer process as well as incomplete growth coverage or crystal growth defects, as certain graphene crystal domain boundaries have been shown to produce perfectly reflecting interfaces for low energy charge carriers[64]. For sample 2, however, it is likely that the defects are transfer-related as the typical domain size obtained with the low partial pressure growth procedure is around 200 μm[63,171]. This conclusion is supported by the fact that the pixels shown as blue dots in Figure 5.9(a) and (b) with $\Gamma = \sigma_{s,M4PP}/\sigma_{s,THz} > 0.4$, i.e. pixels where M4PP sheet conductance is most substantially lowered by micro-scale defects, tend to cluster around holes in the film and regions of very distinct optically visible transfer damage. μ-Raman mapping results also support this notion, as they indicate strong correlation between M4PP and THz-TDS sheet conductance and graphene coverage.

5.6 Conclusions

In summary direct, quantitative mapping of the sheet conductance of cm-scale CVD graphene films by M4PP and non-contact THz-TDS was demonstrated, facilitating characterization of the electrical uniformity of large area graphene films. It was shown that the THz-TDS measurement probes the spatially averaged nanoscopic transport properties of the graphene film while the M4PP microscopic transport measurement is highly sensitive to micro-scale defects. The THz conductance measurement thus provides the natural upper limit for M4PP sheet conductance measurement in graphene. A correlation analysis of quantitative M4PP and THz-TDS mappings of the sheet conductance of a large area CVD graphene film reveals that the film is electrically continuous on the characteristic length scale associated with the THz-TDS measurement of a few tens of nanometers to a few hundred nanometers, while its micro-scale sheet conductance probed by M4PP, is dominated by a high density of insulating defects with dimensions similar to the electrode pitch of 10 μm. μ-Raman mapping of the sample shows that both M4PP and THz-TDS conductances are strongly correlated to the graphene coverage, indicating that the microscopic insulating defects originate from the transfer process or from incomplete growth coverage.

Both the M4PP and the THz-TDS conductance mapping techniques, as demonstrated and quantified here for cm-size graphene areas, are immediately scalable to full wafer dimensions and straightforwardly extended to work on a wide range of substrates, including thin, flexible polymers and doped semiconductors. A THz-TDS scan time of less than 1 minute (1 ms/pixel) for a 4” wafer is technologically possible today (5 s/pixel for M4PP), making this technique particularly promising as a high-throughput, non-contact metrology tool for mapping of the spatially averaged nanoscopic conductance on wafer-scale graphene. In a wider perspective, the application of THz-TDS for nanoscopic conductance mapping can be extended to various electrically non-uniform or structured materials, such as for instance polymer-based, polycrystalline or structured photovoltaic materials. In addition, the combination of M4PP and THz-TDS offers the exciting potential of directly mapping both the Hall mobility[135] and the carrier scattering time[156,182] across wafer-scale areas of graphene films, without need for post-process patterning.

In emerging applications requiring up to square meter dimensions of graphene (electronics, displays, touch screens, photovoltaic applications), rapid, quantitative, contact-free inline characterization of the conductance is of vital importance. The results presented here may help pave the way towards that technologically important goal.

6 Study 3: Gated THz conductance mapping for non-contact graphene mobility mapping

Graphene[2] is finding its uses in an increasing number of commercially oriented applications[55,56,144,148,183–186] and industrial development environments[57,59,187], motivated by its combination of exceptional electronic, optical, and mechanical properties as well as the increasing availability of synthesized large-area graphene films. In particular, there is a profound interest in the commercial adaptation of large-area graphene of high electrical quality for electronic applications, including terahertz (THz) electronics as well as transparent, flexible, and durable electrodes for graphene-based touch-sceens and solar cells[188].

There have been several demonstrations of the unique suitability of terahertz time-domain spectroscopy for rapid and contact-free conductance measurements of large-area graphene[122,123,125,] including the work presented in this thesis. Rapid data acquisition and non-contact nature of the technique facilitates practical implementations of in-line spatial mapping of graphene sheet conductance on a large scale[121,129,189]. For typical electronic applications[190], however, the conductance of a graphene film in itself gives an insufficient picture in terms of its expected performance, necessitating an insight into more fundamental material properties. For many scientific as well as commercial applications, the carrier mobility, μ, and the carrier density, n_s, are essential figures of merit[14,54], and the most straightforward way to obtain information on μ and n_s is through the electric field effect, which requires a variable gate potential. In contact-based electrical measurements μ is thus most commonly measured in the form of the field effect mobility, μ_{FE}, by recording graphene sheet conductance as a function of carrier density which is modulated by an electrostatic back-gate as exemplified in the early work by Novoselov et al.[2] in Figure 6.1.

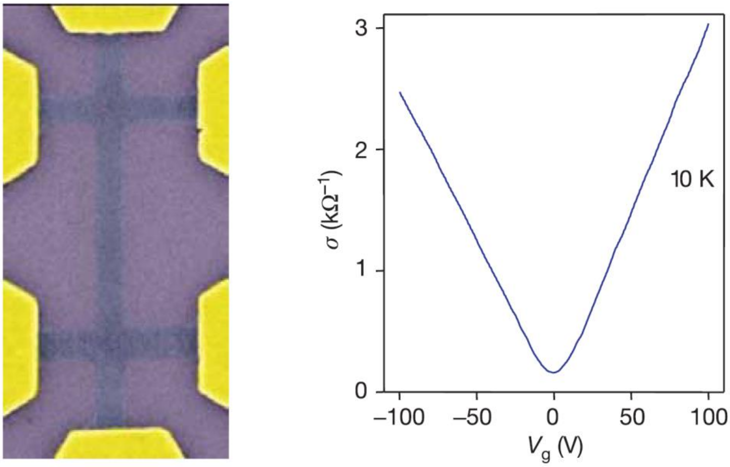

Figure 6.1: SEM micrograph of graphene Hall bar device and gate-sweep measurement showing dependence of graphene sheet conductance on back-gate voltage. Graphene film is separated from a highly doped Si wafer by a 300 nm thick SiO$_2$ layer. Reprinted[2]

Application of a gate voltage, V_g, between a back-gate electrode and the graphene film induces a proportional change, Δn_s, in the free sheet carrier density of the graphene film described by[19]

$$\left|\Delta n_S\right| = \frac{C_g}{e} V_g . \tag{6.1}$$

Here C_g is the gate capacitance and e is the electronic charge. Under typical experiment conditions the quantum capacitance of the system can be neglected[19], and the gate capacitance is given simply as the capacitance of an ideal plate capacitor with a dielectric medium of dielectric constant ε_r, $C = \frac{\varepsilon_0 \varepsilon_r}{t}$:

$$\left|\Delta n_S\right| = \frac{\varepsilon_0 \varepsilon_r}{t \cdot e} V_g , \tag{6.2}$$

where ε_0 is the vacuum permittivity and t is the thickness of gate dielectric. This assumption for the capacitance is valid for highly doped back-gate electrodes where depletion width is negligible. Within the regime of charge transport limited by long-range, charged impurity scattering [19,34,35,42], the added free graphene carriers result in a roughly linear change in the graphene sheet conductance, σ_s, with the field effect mobility being a proportionality factor. The differential sheet conductance, $\Delta\sigma_s$, is thus given as

$$\left|\Delta\sigma_s\right| = e\mu_{FE}\left|\Delta n_s\right| = \frac{\mu_{FE}\varepsilon_0\varepsilon_r}{t}V_g\ , \tag{6.3}$$

Which makes it evident that the field effect mobility can be extracted as the slope of the plot in Figure 6.1 as

$$\mu_{FE} = \frac{t}{\varepsilon_0\varepsilon_r}\left|\frac{\Delta\sigma_s}{\Delta V_g}\right|. \tag{6.4}$$

It should be noted that this relation only holds true far from the charge-neutrality point where a majority carrier density is well-defined[19].

6.1 THz conductance mapping of back-gated graphene: Low-doped silicon back-gate

By means of an electrostatic gate, semi-transparent to THz radiation, graphene carrier density can be controlled during THz-TDS sheet conductance measurements, resulting in substantial changes in the THz contrast of the graphene film, as shown in the series of gated THz conductance maps in Figure 6.2 and demonstrated in references [44,127,128].

Here, CVD graphene grown on poly-crystalline commercially available Cu foil is transferred onto a silicon substrate with a moderate doping level of around 10^{15} cm^{-3}, resulting in a resistivity of approximately 1.6 Ω-cm. In contrast to high resistivity silicon substrates, it is possible to use this type of wafer substrate as a back-gate electrode for creating a gating electric field between substrate and graphene film, while still allowing some THz contrast between graphene-covered and un-covered regions.

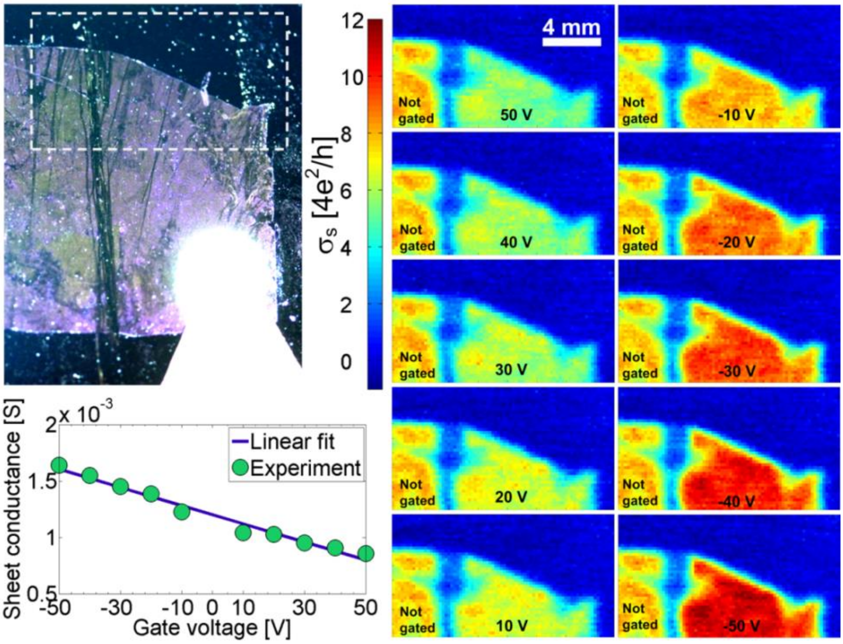

Figure 6.2: Back-gated CVD graphene THz-TDS conductance maps. Fermi level is controlled during THz-TDS conductance mapping by applying a DC voltage between CVD graphene film and a semi-transparent n-type silicon substrate (1.6 Ω-cm) separated by a 300 nm SiO_2 film

However, while it is possible to alter the Fermi level and thus the sheet carrier density of the CVD graphene film by applying a gate voltage to this structure during THz-TDS conductance mapping, the method does not strictly allow quantitative assessment of μ_{FE} for two reasons. Firstly, when the silicon gate is operated in accumulation mode, it is not possible to isolate the gate-differential response of the graphene charge carriers from that of the silicon charge carriers. This problem arises because equal numbers of oppositely charged carriers are injected into the graphene film as well as a thin accumulation layer in the top layer of the silicon wafer substrate, as illustrated in Figure 4.3(a). Since the combined thickness, T, of graphene film, gate dielectric and the silicon top layer is significantly smaller than the THz wavelength, the sheet conductance measured in a THz-TDS experiment is the parallel conductance associated with both graphene carriers and silicon carriers:

$$\Delta\sigma_{s,measured} = \Delta\sigma_{Graphene} + \Delta\sigma_{Si} = e\left|\Delta n_s\right|\left(\mu_{Graphene} + \mu_{Si}\right) \tag{6.5}$$

For typical CVD graphene samples with mobilities in the range 500-10,000 cm^2/Vs, the contribution from silicon charge carriers with mobility up to 1,400 cm^2/vs (450 cm^2/vs for holes) is therefore non-negligible[8].

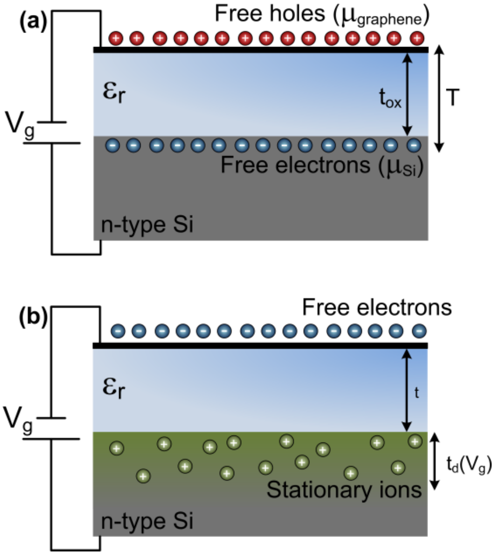

Figure 6.3: Silicon-dielectric-graphene capacitor structure where the silicon substrate is in (a) accumulation and (b) depletion.

Secondly, the assumption of a voltage-independent gate capacitance made in equation (6.2) does not necessarily hold true for semiconductor gate electrodes with low doping levels due to voltage drops across the gate voltage-dependent width of depletion regions, illustrated in Figure 4.3(b). For silicon with a doping density of 10^{15} cm^{-3}, the voltage-dependent width of such depletion regions in a metal-oxide-semiconductor (MOS) structures can be as wide as 850 nm, while the maximum depletion width is only 34 nm for a carrier density of 10^{18} cm^{-3}. The voltage drop across such a region, which is in general dependent on the applied gate voltage, can therefore in cases of low doped semiconducting gates be significant in comparison with the voltage drop across the gate dielectric which is typically of thicknesses between 50-300 nm. The appearance of these wide depletion regions in capacitor structures based on low doped semiconductors can thus result in highly non-linear gate capacitances, making quantitative extraction of graphene field effect mobility rather complicated and unreliable.

For the reasons listed above, a substrate with a low-mobility, high carrier concentration gate electrode was developed and utilized in the following section to present a first demonstration of quantitative field effect carrier mobility mapping of large-scale graphene.

6.2 Quantitative large-area mapping of carrier mobility in graphene: Highly doped poly-silicon back-gate

Here we demonstrate quantitative mapping of the field-effect carrier mobility in a large-area monolayer CVD graphene film based on in-situ electrically gated THz-TDS imaging. In contrast to prior electrically gated THz spectroscopy experiments[44,124,127,128] performed on graphene we employ a low-mobility, high carrier concentration gate-electrode material, in this case nano-crystalline, highly doped silicon, to ensure an insignificant gate-differential THz conductance response from free carriers injected into the gate-electrode and to reduce potential non-linearities from changing silicon depletion widths. This allows for isolation of the gate-induced graphene conductance and thus a quantitative extraction of the graphene field-effect mobility.

6.2.1 Method

The experiments are carried out using a Picometrix© T-ray™ 4000 fiber-coupled THz time-domain spectrometer relying on photoconductive switches for THz generation and detection, which is detailed in section 3.1. A large-area graphene film is grown on commercially available Cu foil by means of a standard catalytic CVD and is subsequently transferred onto the layered substrate shown in Figure 6.4(a) by a standard polymer-assisted technique, involving complete etching of the Cu substrate in $(NH_4)_2S_2O_8$. The substrate comprises 525 μm, $\rho > 10{,}000\ \Omega$ cm, high resistivity silicon (HR-Si), 50 nm p-doped poly-crystalline (poly-Si) silicon, and 296 nm silicon nitride (Si_3N_4). The whole sample is placed in the THz focal plane formed between 2 aspheric polymer lenses each with a working distance of 25.4 mm. By raster-scanning the graphene sample in steps of 200 μm in the THz focus, pulse waveforms are recorded in every pixel of a spatially resolved map with close to 7500 pixels covering the full extent of the 10x10 mm^2 graphene film. Through utilization of the electric field effect in graphene, THz maps are recorded at different carrier densities by applying voltages, V_g, in the range from -25V to 50V between poly-Si thin film and graphene film. The full acquisition time for each map is 16 minutes, where V_g is increased in discrete steps of 5V between each map, resulting in an average gate voltage sweep rate of 0.3125 V/min.

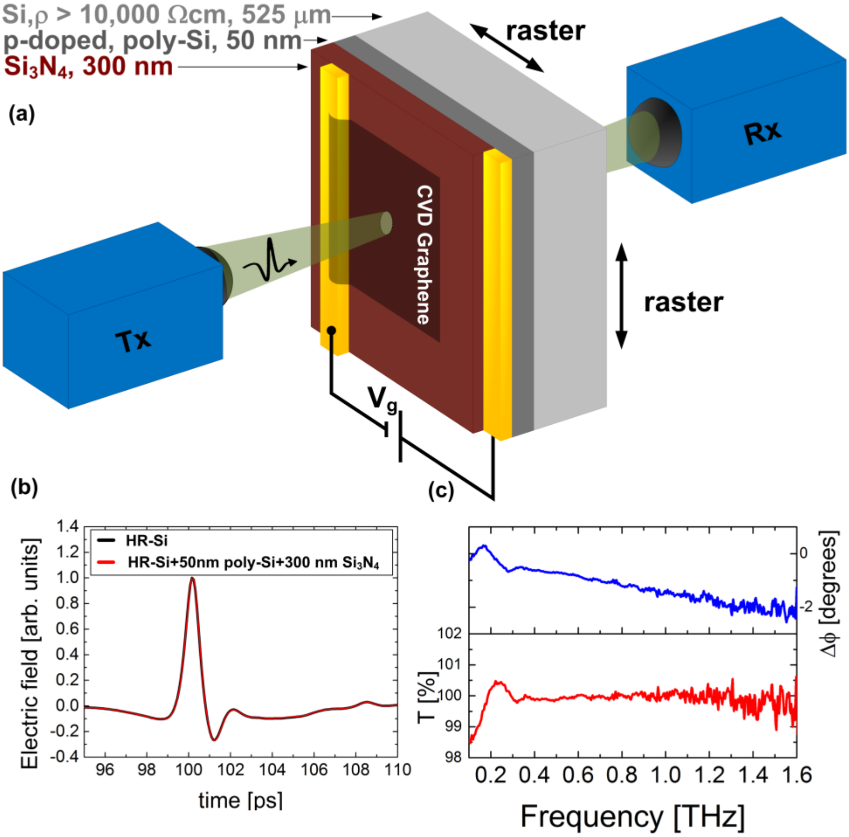
Si,ρ > 10,000 Ωcm, 525 μm
p-doped, poly-Si, 50 nm
Si3N4, 300 nm
(a)
raster
raster
Rx
Tx
CVD Graphene
Vg
(b)
(c)
HR-Si
HR-Si+50nm poly-Si+300 nm Si3N4
Electric field [arb. units]
time [ps]
T [%]
Δϕ [degrees]
Frequency [THz]

Figure 6.4: a) Schematic of sample consisting of large-area monolayer CVD graphene film residing on layered substrate comprising 525 mm HR-Si, 50 nm boron-doped poly-crystalline silicon with n ≈ 10^{18} cm-3, and 300 nm Si3N4. Au contacts are used for contacting the graphene film and the poly-crystalline silicon film. (b) Time-domain waveforms of THz pulses transmitted through a bare HR-Si substrate and a layered HR-Si/poly-Si/Si3N4 substrate (c) Amplitude transmission coefficient and phase-shift for poly-Si and Si3N4 films. The THz response of the thin films is found to be negligible.

The THz response of the poly-Si and Si_3N_4 films was characterized by performing transmission measurements on a bare HR-Si substrate as well as the layered HR-Si/poly-Si/Si_3N_4 structure, as shown in Figure 6.4(b). It was found that the THz response of the poly-Si and Si_3N_4 films is negligible, as also evidenced by the frequency-independent transmission of 100%, shown in Figure 6.4(c). The 2-point contact DC sheet conductance of the poly-Si thin film was also measured at a value of σ_S=0.03 mS, which is at the limit of sensitivity of the spectrometer. The 2-point sheet conductance value is consistent with an expected carrier mobility[191] of 40 cm^2/Vs and carrier density of 10^{18} cm^{-3}, as measured by secondary ion mass spectroscopy profiling. The phase-shift of 2 degrees, seen in Figure 6.4(c), is attributed to slight differences in HR-Si substrate thickness between the positions of the reference and sample measurements. The THz response of poly-Si and Si_3N_4 layers are therefore neglected in the data analysis. Finally, contacts to poly-Si thin film and contacts for a subsequently transferred CVD graphene film is defined by electron-beam deposition of 5 nm Ti and 100 nm Au through an aluminium shadow mask.

6.2.2 Substrate fabrication

As described above, the utilization of a back-gate material combining a sufficiently low carrier mobility relative to that of CVD graphene and a carrier density high enough to suppress the impact of a voltage-dependent depletion width on the gate capacitance of the system is essential for quantitative extraction of field effect mobility in electrically gated THz-TDS studies of graphene. In addition, a suitable substrate also has to provide a useful contrast between graphene-covered and non-graphene-covered areas. In practical terms for transmission THz-TDS measurements, this requires that the total sheet conductance of the substrate is kept low enough that a substantial amount of THz radiation is transmitted through the substrate. Since no off-the-shelf substrates offer the combination of low mobility, high carrier density and low total sheet conductance, substrates were designed and fabricated specifically for this purpose. To keep the sheet conductance of the substrate low, while allowing the use of a high carrier density gate material, an approach was chosen where a deposited thin film is used as back gate. To meet the requirements of low carrier mobility and high carrier density, a boron-doped chemical vapor deposited poly-crystalline silicon thin film was chosen, as it yields a carrier mobility of less than 40 cm^2/Vs [191] and facilitates high doping densities.

The entire fabrication process is outlined in Figure 6.5. The CVD process that was used introduces 80 sccm of SiH_4 and 7 sccm of B_2H_6 during low pressure chemical vapor deposition at 620^o C for in-growth doping to a carrier density of 10^{18} cm^{-3}. Using this method, 50 nm thick boron-doped poly-crystalline silicon films were deposited on high resistivity double-side-polished silicon wafers ($\rho > 10{,}000\ \Omega \cdot \mathrm{cm}$), resulting in a sheet conductance of the thin film of σ_s=0.03 mS. As shown in Figure 6.4(b) and (c), this results in negligible absorption and reflection of THz radiation. The poly-Si film deposited on the back-side of the wafer is removed by reactive ion etching using an RF plasma of SF_6 and O_2 species. Subsequently, a gate dielectric layer of 300 nm Si_3N_4 is deposited by a cyclic plasma-enhanced CVD (PECVD) process on the top side, after which a window is opened in the Si_3N_4 by a partial dip in buffered hydrofluoric acid (BHF) for 10 minutes.

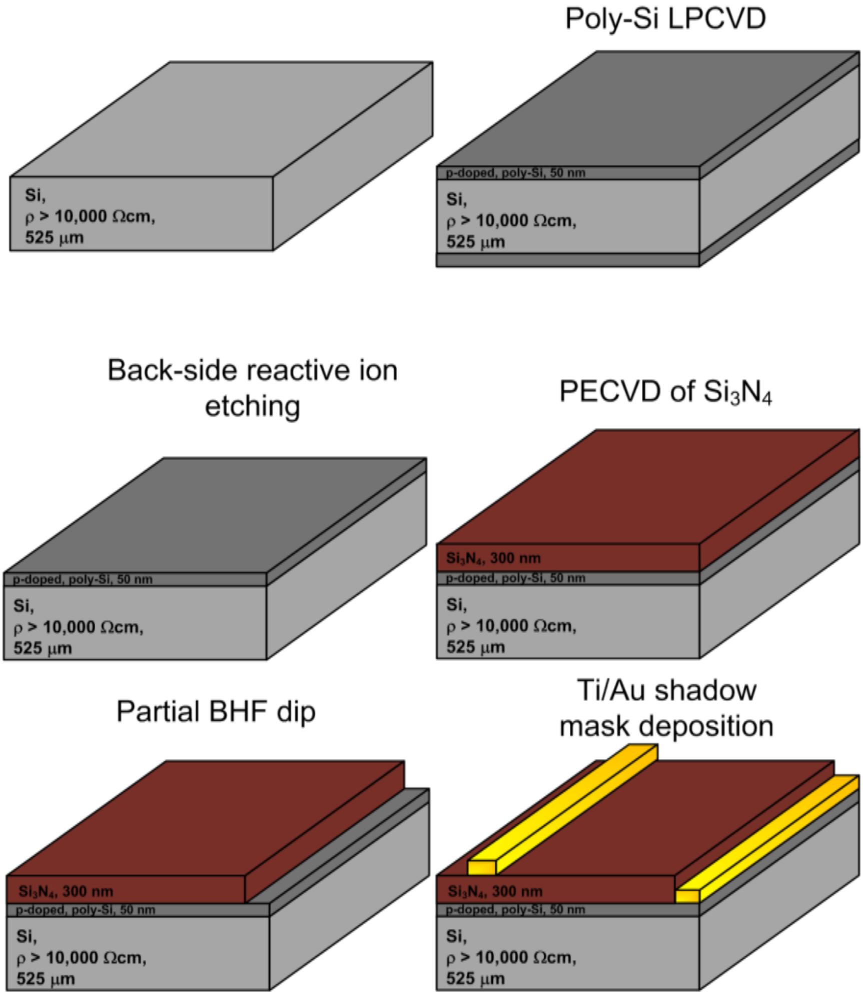
Si,
ρ > 10,000 Ωcm,
525 µm
Poly-Si LPCVD
p-doped, poly-Si, 50 nm
Si,
ρ > 10,000 Ωcm,
525 µm
Back-side reactive ion etching
p-doped, poly-Si, 50 nm
Si,
ρ > 10,000 Ωcm,
525 µm
PECVD of Si3N4
Si3N4, 300 nm
p-doped, poly-Si, 50 nm
Si,
ρ > 10,000 Ωcm,
525 µm
Partial BHF dip
Si3N4, 300 nm
p-doped, poly-Si, 50 nm
Si,
ρ > 10,000 Ωcm,
525 µm
Ti/Au shadow mask deposition
Si3N4, 300 nm
p-doped, poly-Si, 50 nm
Si,
ρ > 10,000 Ωcm,
525 µm

Figure 6.5: Outline of the design and fabrication of substrates for quantitative extraction of carrier mobility from THz-TDS measurement. Based on poly-crystalline silicon thin film back-gate and plasma-enhanced chemical vapour deposited Si_3N_4 gate dielectric

6.2.3 Results and Discussion

THz maps of the CVD graphene film were recorded at 15 different gate voltages between -25V and 50V, as shown in Figure 6.6(a) where the data is represented by images showing the transmitted THz power. Since the CVD graphene film is heavily p-doped, most likely due to exposure to the $(NH_4)_2S_2O_8$ Cu etchant[62], the conductance and therefore the THz response of the graphene film are lowest in the V_g = 35V THz map.

The differential gate-induced sheet conductance of the graphene film was extracted in each pixel of the THz maps based on its direct relation, shown in equation(6.7), to the complex-valued transmission coefficient, $\Delta\tilde{T}\left(\omega\right)$. Equation (6.7) is derived from Fresnel coefficients for the boundaries in the sample geometry, which is modeled as an infinitely thin conducting surface of sheet conductance, $\Delta\tilde{\sigma}_s\left(\omega\right)$[94,119] on a thick HR-Si dielectric medium with refractive index n_{Si}=3.417[133]. The complex transmission function is calculated as the ratio of the Fourier transform of the transmitted THz waveform, $\tilde{E}_N$, to that of the corresponding pixel in the V_g = 35 V map, $\tilde{E}_{35V}$.

$$\Delta\tilde{T}(\omega)=\frac{\tilde{E}_N}{\tilde{E}_{35V}}=\frac{n_{Si}+1}{n_{Si}+1+Z_0\Delta\tilde{\sigma}_s}. \tag{6.6}$$

From this relation it follows that the differential sheet conductance is

$$\Delta\tilde{\sigma}_s\left(\omega\right)=\frac{1}{Z_0}\left(\frac{n_{Si}+1}{\Delta\tilde{T}(\omega)}-n_{Si}-1\right), \tag{6.7}$$

where Z_0 = 377 Ω is the vacuum impedance. Figure 6.6(b) shows an example of the extracted $\Delta\tilde{\sigma}_s\left(\omega\right)$ spectrum from the central region of the graphene film with low THz transmission. The gate-induced THz sheet conductance exhibits a constant real part of the conductance with magnitude varying with gate voltage and a constant imaginary part of the conductance, which is generally close to zero in the accessible frequency range of 0.15-1.4 THz. This is consistent with a Drude conductance response, which has been reported for graphene in numerous prior investigations[44,122–124,126–128].

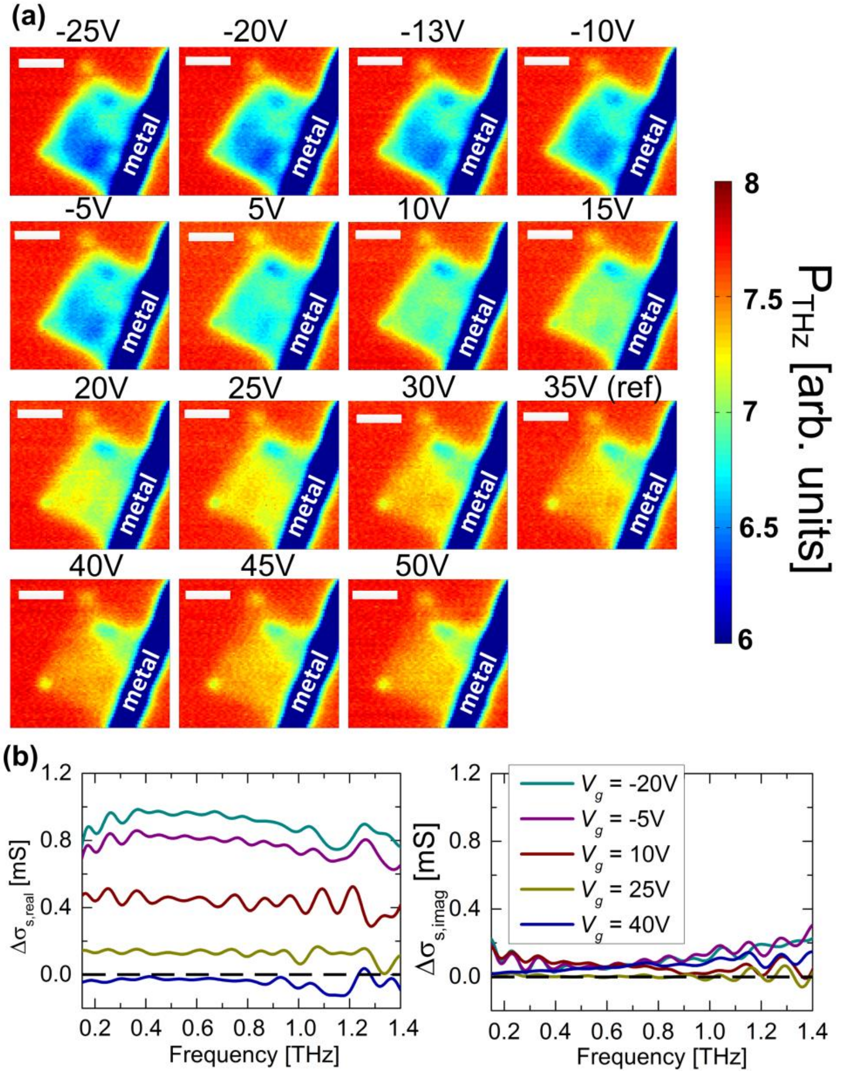

Figure 6.6: (a) Raster images showing the transmitted THz power at different gate voltages. The THz power scale has been compressed to highlight the contrast of the graphene film. White scale bars are 5 mm. (b) Frequency-dependent, gate-induced sheet conductance of the graphene film in the central region at series of different gate voltages. Left: real part of the sheet conductance. Right: imaginary part of the sheet conductance. The features around 1.15 THz are artifacts due to residual atmospheric water vapour absorption.

For frequencies significantly below the inverse scattering time ($2\pi f \ll 1/\tau$), the Drude model dictates that the real part of $\Delta\tilde{\sigma}_s(\omega)$ is constant and near its DC value while the imaginary part is close to zero. Our spectrally resolved measurement can thus be replaced by a single, real-valued quantity reflecting the gate-induced DC conductance. In Figure 6.7 we have used this approach to form spatial maps of the gate-induced graphene sheet conductance, represented by the average value of $\mathrm{Re}\left(\Delta\tilde{\sigma}_s\left(\omega\right)\right)$ between 0.5-0.9 THz, from here on referred to as $\Delta\sigma_S$. The evolution of $\Delta\sigma_s$ with varying V_g in the series of images in Figure 6.7 is a result of the electric field effect in graphene and thus provides vital information on the carrier mobility in the film. Figure 6.8(a) shows $\Delta\sigma_S$ as a function of V_g for 3 distinct positions of the mapped area with highly conducting graphene, less conducting graphene, and no graphene coverage. In contrast to recent back-gated THz spectroscopy investigations of CVD graphene[44,127,128], our measurement of $\Delta\sigma_s$ shows a linear dependence on the applied gate voltage in the range from V_g = -25V to V_g = 30V with different slopes throughout the extent of the graphene film reflecting the local field-effect mobility. This observation is found to be representative throughout the graphene film area. The linear dependence of $\Delta\sigma_S$ on V_g is expected for graphene films where long-range, charged impurity scattering dominates over short-range neutral defect scattering[19,41], and typically observed in DC transport measurements of samples with field effect mobility μ < 10.000 cm^2/Vs[2,32,36]. In DC transport measurements, a sub-linear regime is normally only observed in ultra-clean exfoliated graphene flakes deposited on substrates with very low interaction with the graphene layer[32,192]. For gate voltages 30V < V_g < 50V a plateau with close to constant $\Delta\sigma_S$ is found, which is consistent with a gate-independent charge-puddle regime near the charge-neutrality-point (CNP) in graphene[19]. Application of a gate voltage, V_g, between the poly-Si thin film and the graphene film induces a proportional change in the free carrier density, Δn_S, in the poly-Si and graphene films, as described by equation(6.8) . Within the regime of long-range, charged impurity scattering, the added free graphene carriers result in a roughly linear change in the graphene sheet conductance, $\Delta\sigma_S$, with the field effect mobility being a proportionality factor. The differential sheet conductance, $\Delta\sigma_S$, of the graphene film is thus described by the relations[19]:

$$\left|\Delta n_S\right| = \frac{C_g}{e}\Delta V_g = \frac{\varepsilon_0\varepsilon_{SiN}}{t\cdot e}\Delta V_g \, , \tag{6.8}$$

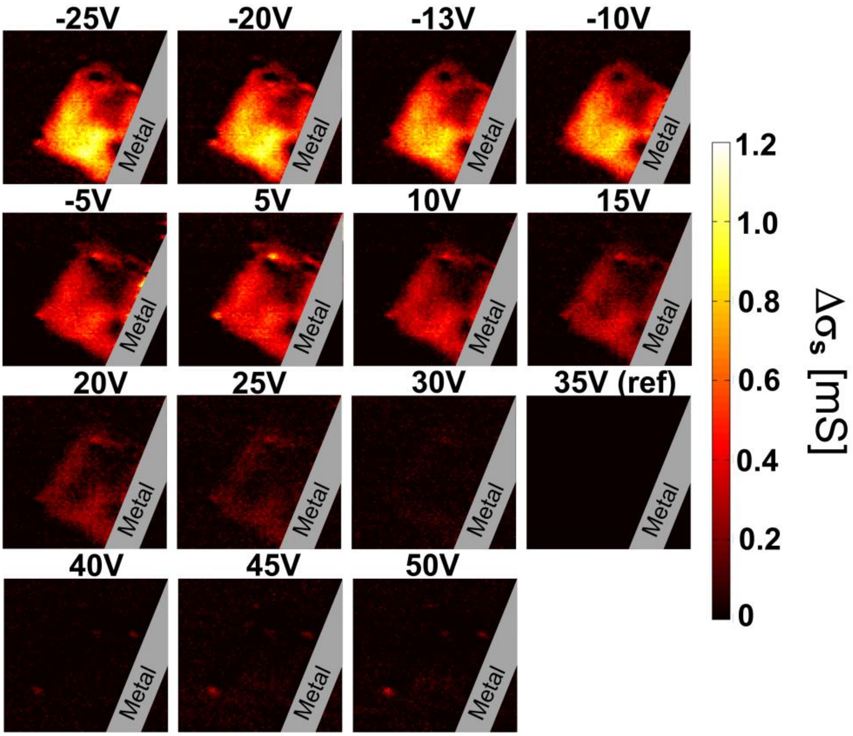

Figure 6.7: Sheet conductance images represented by the average, real sheet conductance value from 0.5-0.9 THz.

$$\left|\Delta\sigma_S\right| = e\mu_{FE}\left|\Delta n_S\right| = \frac{\mu_{FE}\varepsilon_0\varepsilon_{SiN}}{t}\Delta V_g \ , \tag{6.9}$$

and

$$\mu_{FE} = \frac{t}{\varepsilon_0\varepsilon_{r,SiN}}\left|\frac{\Delta\sigma_S}{\Delta V_g}\right| \tag{6.10}$$

where C_g is the gate capacitance, e is the electronic charge, ε_0 is the vacuum permittivity, ε_{SiN}=7.5 is the relative permittivity of silicon nitride, t is the thickness of silicon nitride gate dielectric, and μ_{FE} is the field-effect mobility of the graphene film. The gate-induced conductance change in the poly-Si substrate can be neglected because the carrier mobility in thin, boron-doped polycrystalline silicon films $\mu_{poly\text{-}Si}$, < 40 cm^2/Vs[191], and therefore is insignificant relative to that of graphene, which in our case is more than an order of magnitude higher.

Because of the choice of a low-mobility, high carrier concentration gate material, the experiments presented here provide a direct and reliable measure of the gate-induced conductance evolution of the graphene film with an insignificant contribution from gate-induced carriers in the substrate. Following equation(6.10), the graphene field effect mobility can thus be obtained in each pixel of the mapped area by retrieving the slope $|\Delta\sigma_s/\Delta V_g|$ in the high density-region away from the CNP.

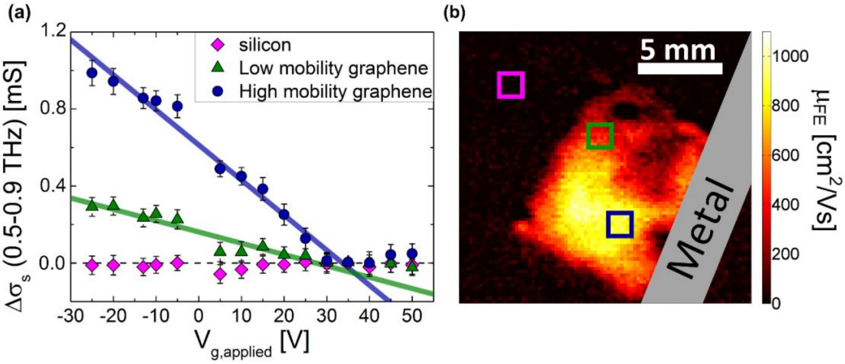

Figure 6.8: (a) Average, real, gate-induced sheet conductance from 0.5 to 0.9 THz as a function of Vg for 3 distinct positions of the mapped area. Circles, triangles and squares are experimental data and the full lines are linear fits to the data for Vg from -25V to +20V. (b) Map showing the spatial distribution of field effect mobility across the CVD graphene film evaluated at 0.5-0.9 THz.

Based on this central result we are able to show a spatially resolved field-effect mobility map for the large-area CVD graphene film in Figure 6.8(b), resulting from the application of equation (6.10) to the entire dataset, where the slope $|\Delta\sigma_s/\Delta V_g|$ has been found in each pixel by a linear fitting routine to $\Delta\sigma_s$ vs. V_g from -25V to +20V. Even on a scale of a few mm, it is found that the carrier mobility varies by a factor of 2-3, highlighting the importance of techniques that either facilitate a statistical approach for assessing transport properties in CVD graphene or allow spatial mapping of graphene transport properties such as that presented here. We find that such a procedure gives far more comprehensive information than the typical convention of relying on a few representative electrical measurements from random or selected areas of a large graphene film. The general observation of a CNP position at V_g higher than 30 V suggests a non-intentional chemical doping density higher than $4\cdot 10^{12}$ cm^{-2}. This relatively high chemical doping density further supports the likelihood that the electronic transport is dominated by long-range scattering on charged impurities[19]. With the use of a higher quality gate dielectric, allowing wider gate sweeps and thereby accurate observations of the CNP for each pixel, the presented method can be straightforwardly extended to provide independent probing and spatially resolved mapping of carrier density and chemical impurity doping density in large-area graphene films.

It should be noted that the local carrier mobilities obtained in these measurements are expected to be a slight underestimate of the actual carrier mobilities of the graphene film. Due to the low gate sweep rate of 0.3125 V/min, water adsorption and trapping of charges in the silicon nitride is expected to reduce the effective gate voltage significantly[193,194]. This issue may be explored further by a transition to a measurement protocol, where the gate voltage instead is swept for each raster-position of the sample, allowing for variation of the gate sweep rate in a range (typically around 1 V/s[193,194]) relevant for the processes leading to gate hysteresis.

We anticipate that such quantitative, non-contact mapping of graphene carrier mobility will have a significant technological importance for the advancement of production and implementations of large-area graphene in commercial electronic applications and that it can contribute to the fundamental insight into charge carrier dynamics of the graphene solid-state-system by paving the way for investigations of transport dynamics with unprecedented statistical basis.

6.2.4 Conclusion

In conclusion, we have presented non-contact, quantitative mapping of graphene field effect mobility in a 10x10 mm^2 large-area CVD film by in-situ electrically gated THz-TDS measurements. A THz-TDS scan time of less than 1 min (1 ms/pixel) for a 4” wafer is technologically possible today, making the presented method immediately scalable to full wafer dimensions. While THz-TDS is based on an optical characterization, the frequency range is well below the inverse scattering time of graphene, and thus the spectroscopically obtained conductance can be directly extrapolated to its DC value. The technique thus opens up the possibility for assessment of fundamental electrical transport properties such as carrier mobility and chemical impurity doping density on basis of large statistical ensembles, or large-area spatial mapping of carrier mobility and carrier density. Far from the charge-neutrality-point, our measurements show a linear dependence of the THz sheet conductance on carrier density, which is a signature of electrical transport limited by long-range, charged impurity scattering, also observed in most DC transport measurements on graphene. On a scale of just few mm, we find significant spatial variations of a factor of 2-3 in carrier mobility, which highlights the importance of techniques that facilitate highly statistical or spatially resolved approaches for assessing transport properties in CVD graphene.

7 Conclusions

The main goal of the work presented in this thesis has been to utilize terahertz time-domain spectroscopy for assessing the terahertz transport dynamics of graphene charge carriers. Specifically, the efforts have been directed towards two aspects of terahertz time-domain spectroscopy measurements on graphene; (1) investigation of the fundamental carrier transport dynamics at femtosecond to picosecond timescales and (2) the application of terahertz time-domain spectroscopy to commercially relevant non-contact, large-area electrical characterization of graphene.

Investigations of chemical vapor deposited graphene films, combining conventional and ultra-broadband terahertz time-domain spectroscopy, revealed qualitatively different terahertz transport dynamics in graphene films grown on poly-crystalline copper foils and single-crystalline copper (111) substrates. While the terahertz conductance of graphene grown on single-crystalline copper agreed with predictions of a Drude-type electrical response in graphene, the terahertz conductance of graphene grown on poly-crystalline copper foil was found to be distinctly better described by the Drude-Smith model. This astounding observation was interpreted in the context of preferential carrier back-scattering on extended electronic barriers with a characteristic length scale corresponding to the probing length scale of the AC field on the order of 10-100 nm. Although the cause of such back-scattering was not experimentally identified, the most likely origin of partially reflecting electronic barriers on this length scale in CVD graphene films is crystal domain boundaries in the poly-crystalline CVD graphene film. Direct and accurate measurement of the carrier scattering time and the Drude weight in graphene grown on single-crystalline copper allowed evaluation of the mean free path, carrier density and carrier mobility within the framework of diffusive transport limited by long-range scattering on charged impurities. These results underline the unique potential of ultra-broadband terahertz time-domain spectroscopy for non-contact measurement of the nature of conduction and fundamental electrical transport parameters without need for application of external gating potentials or magnetic fields. The observed Drude and Drude-Smith spectra imply that the THz conductance of the films is close to its DC value at frequencies well below the scattering rate. This was confirmed in experiments, systematically comparing line scans of terahertz AC and micro four-point probe DC sheet conductance, based on which full wafer-scale, non-contact mapping of CVD graphene electrical sheet conductance was demonstrated by terahertz time-domain spectroscopic imaging. This demonstration shows that THz-TDS can indeed facilitate the rapid and reliable large-scale measurement of electronic properties and their uniformity in large-scale graphene, which might be viewed as a vital requirement for industrial implementation of the material.

The correlation between terahertz AC conductance and micro four-point probe DC conductance was investigated in detail based on concurrent conductance mapping by terahertz time-domain spectroscopy and micro four-point probe measurements in centimeter-scale CVD graphene films. On the statistical basis of more than 4000 individual electrical conductance measurements it was found that the micrometer-scale conductance of the investigated film was dominated by electrical defects on a characteristic scale on the order of 10 μm. Even though the recent ultra-broadband terahertz spectroscopy results presented in this thesis show presence of electrical defects also on the nanoscopic scale, the micro four-point probe microscopic conductance was thus found to be significantly reduced relative to the terahertz nanoscopic conductance. The terahertz conductance therefore provides a natural upper limit for the micro four-point probe conductance in the graphene film.

Finally, large-scale, quantitative, non-contact mapping of field effect mobility in a 10x10 mm^2 CVD graphene film was demonstrated by in-situ electrically gated terahertz time-domain spectroscopic imaging. Quantitative extraction of the field effect mobility was enabled by the use of designed and fabricated substrates with a low-mobility, high-carrier density poly-crystalline silicon back-gate, which ensures an insignificant gate-induced conductance response from carriers injected into the gate electrode. Far from the charge-neutrality-point, the terahertz sheet conductance shows a linear dependence on carrier density, which is a signature of electrical transport limited by long-range, charged impurity scattering, also observed in most DC transport measurements on graphene. Significant spatial variations in carrier mobility of a factor of 2-3 was found on a scale of just few millimeters, highlighting the importance of techniques that facilitate highly statistical or spatially resolved approaches for assessment of transport properties in CVD graphene.

8 Bibliography

8.1 List of references

1. Novoselov, K. S. *et al.* Electric Field Effect in Atomically Thin Carbon Films. *Science (80-.).* **306,** 666–669 (2004).

2. Novoselov, K. S. *et al.* Two-dimensional gas of massless Dirac fermions in graphene. *Nature* **438,** 197–200 (2005).

3. Zhang, Y., Tan, Y.-W., Stormer, H. L. & Kim, P. Experimental observation of the quantum Hall effect and Berry's phase in graphene. *Nature* **438,** 201–204 LA – en (2005).

4. Ad-hoc-working-group (European commision). *Critical raw materials for the EU - Report of the Ad-hoc Working Group on defining critical raw materials*. 1–84 (2010).

5. De, S. & Coleman, J. N. Are there fundamental limitations on the sheet resistance and transmittance of thin graphene films? *ACS Nano* **4,** 2713–20 (2010).

6. Hecht, D. S., Hu, L. & Irvin, G. Emerging transparent electrodes based on thin films of carbon nanotubes, graphene, and metallic nanostructures. *Adv. Mater.* **23,** 1482–513 (2011).

7. Schwierz, F. Graphene transistors. *Nat. Nanotechnol.* **5,** 487–496 (2010).

8. Jacoboni, C., Canali, C., Ottaviani, G. & Alberigi Quaranta, A. A review of some charge transport properties of silicon. *Solid. State. Electron.* **20,** 77–89 (1977).

9. Fistul, V. I., Iglitsyn, M. I. & Omelyanovskii, E. M. Mobility of electrons in germanium strongly doped with arsenic. *Sov. Physics-Solid Sate* **4,** 784–785 (1962).

10. Jacoboni, C., Nava, F., Canali, C. & Ottaviani, G. Electron drift velocity and diffusivity in germanium. *Phys. Rev. B* **24,** 1014–1026 (1981).

11. Blakemore, J. S. Semiconducting and other major properties of gallium arsenide. *J. Appl. Phys.* **53,** R123 (1982).

12. Karataev, V. V., Milvidskii, M. G., Rytova, N. S. & Fistul, V. I. Compensation in n-type InAs. *Sov. Phys. Semicond.* **11,** 1009–1011 (1977).

13. Dürkop, T., Getty, S. A., Cobas, E. & Fuhrer, M. S. Extraordinary Mobility in Semiconducting Carbon Nanotubes. *Nano Lett.* **4,** 35–39 (2004).

14. Mayorov, A. S. *et al.* Micrometer-scale ballistic transport in encapsulated graphene at room temperature. *Nano Lett.* **11,** 2396–9 (2011).

15. Geim, A. K. & Novoselov, K. S. The rise of graphene. *Nat Mater* **6,** 183–191 (2007).

16. Novoselov, K. S. *et al.* Two-dimensional atomic crystals. *Proc. Natl. Acad. Sci.* **102,** 10451–10453 (2005).

17. Charlier, J.-C., Eklund, P. C. & Ferrari, A. C. in *Carbon Nanotub. Adv. Top. Synth. Struct. Prop. Appl.* **111,** 673–709 (Springer Berlin Heidelberg, 2008).

18. Castro Neto, A. H., Peres, N. M. R., Novoselov, K. S. & Geim, A. K. The electronic properties of graphene. *Rev. Mod. Phys.* **81,** 109–162 (2009).

19. Das Sarma, S., Adam, S., Hwang, E. H. & Rossi, E. Electronic transport in two-dimensional graphene. *Rev. Mod. Phys.* **83,** 407–470 (2011).

20. Geim, A. K. & MacDonald, A. H. Graphene: Exploring carbon flatland. *Phys. Today* **60,** 35–41 (2007).

21. Morozov, S. *et al.* Giant Intrinsic Carrier Mobilities in Graphene and Its Bilayer. *Phys. Rev. Lett.* **100,** 016602 (2008).

22. Ferrari, A. C. Raman spectroscopy of graphene and graphite: Disorder, electron-phonon coupling, doping and nonadiabatic effects. *Solid State Commun.* **143,** 47–57 (2007).

23. Ferrari, A. C. & Basko, D. M. Raman spectroscopy as a versatile tool for studying the properties of graphene. *Nat. Nanotechnol.* **8,** 235–46 (2013).

24. Yu, V., Whiteway, E., Maassen, J. & Hilke, M. Raman spectroscopy of the internal strain of a graphene layer grown on copper tuned by chemical vapor deposition. *Phys. Rev. B* **84,** (2011).

25. Aleiner, I. L. & Efetov, K. B. Effect of Disorder on Transport in Graphene. *Phys. Rev. Lett.* **97,** 236801 (2006).

26. Altland, A. Low-Energy Theory of Disordered Graphene. *Phys. Rev. Lett.* **97,** 236802 (2006).

27. Peres, N. M. R., Guinea, F. & Castro Neto, A. H. Electronic properties of disordered two-dimensional carbon. *Phys. Rev. B* **73,** 125411 (2006).

28. Tworzydło, J., Trauzettel, B., Titov, M., Rycerz, A. & Beenakker, C. Sub-Poissonian Shot Noise in Graphene. *Phys. Rev. Lett.* **96,** 246802 (2006).

29. Bardarson, J., Tworzydło, J., Brouwer, P. & Beenakker, C. One-Parameter Scaling at the Dirac Point in Graphene. *Phys. Rev. Lett.* **99,** 106801 (2007).

30. Kashuba, A. Conductivity of defectless graphene. *Phys. Rev. B* **78,** 085415 (2008).

31. Fritz, L., Schmalian, J., Müller, M. & Sachdev, S. Quantum critical transport in clean graphene. *Phys. Rev. B* **78,** 085416 (2008).

32. Tan, Y.-W. *et al.* Measurement of Scattering Rate and Minimum Conductivity in Graphene. *Phys. Rev. Lett.* **99,** 246803 (2007).

33. Martin, J. *et al.* Observation of electron–hole puddles in graphene using a scanning single-electron transistor. *Nat. Phys.* **4,** 144–148 (2007).

34. Hwang, E., Adam, S. & Sarma, S. Carrier Transport in Two-Dimensional Graphene Layers. *Phys. Rev. Lett.* **98,** 186806 (2007).

35. Adam, S., Hwang, E. H., Galitski, V. M. & Das Sarma, S. A self-consistent theory for graphene transport. *Proc. Natl. Acad. Sci. U. S. A.* **104,** 18392–7 (2007).

36. Chen, J.-H. *et al.* Charged-impurity scattering in graphene. *Nat. Phys.* **4,** 377–381 (2008).

37. Meyer, J. C. *et al.* The structure of suspended graphene sheets. *Nature* **446,** 60–3 (2007).

38. Mayorov, A. S. *et al.* How Close Can One Approach the Dirac Point in Graphene Experimentally? *Nano Lett.* **12,** 4629–34 (2012).

39. Schlom, D. G. & Pfeiffer, L. N. Oxide electronics: Upward mobility rocks! *Nat. Mater.* **9,** 881–3 (2010).

40. Geim, A. K. & Novoselov, K. S. The rise of graphene. *Nat. Mater.* **6,** 183–91 (2007).

41. Ando, T. Screening Effect and Impurity Scattering in Monolayer Graphene. *J. Phys. Soc. Japan* **75,** 074716 (2006).

42. Nomura, K. & MacDonald, A. H. Quantum Transport of Massless Dirac Fermions. *Phys. Rev. Lett.* **98,** 076602 (2007).

43. Peres, N., Lopes dos Santos, J. & Stauber, T. Phenomenological study of the electronic transport coefficients of graphene. *Phys. Rev. B* **76,** 073412 (2007).

44. Horng, J. *et al.* Drude conductivity of Dirac fermions in graphene. *Phys. Rev. B* **83,** 165113 (2011).

45. Petrone, N. *et al.* Chemical vapor deposition-derived graphene with electrical performance of exfoliated graphene. *Nano Lett.* **12,** 2751–6 (2012).

46. Tao, L. *et al.* Uniform Wafer-Scale Chemical Vapor Deposition of Graphene on Evaporated Cu (111) Film with Quality Comparable to Exfoliated Monolayer. *J. Phys. Chem. C* **116,** 24068–24074 (2012).

47. Hernandez, Y. *et al.* High-yield production of graphene by liquid-phase exfoliation of graphite. *Nat. Nanotechnol.* **3,** 563–8 (2008).

48. Stankovich, S. *et al.* Synthesis of graphene-based nanosheets via chemical reduction of exfoliated graphite oxide. *Carbon N. Y.* **45,** 1558–1565 (2007).

49. Li, X. *et al.* Highly conducting graphene sheets and Langmuir–Blodgett films. *Nat. Nanotechnol.* **3,** 538–542 (2008).

50. Lotya, M. *et al.* Liquid phase production of graphene by exfoliation of graphite in surfactant/water solutions. *J. Am. Chem. Soc.* **131,** 3611–20 (2009).

51. First, P. N. *et al.* Epitaxial Graphenes on Silicon Carbide. *MRS Bull.* **35,** 296–305 (2011).

52. Emtsev, K. V *et al.* Towards wafer-size graphene layers by atmospheric pressure graphitization of silicon carbide. *Nat. Mater.* **8,** 203–7 (2009).

53. Berger, C. *et al.* Ultrathin Epitaxial Graphite: 2D Electron Gas Properties and a Route toward Graphene-based Nanoelectronics. *J. Phys. Chem. B* **108,** 19912–19916 (2004).

54. Li, X. *et al.* Large-Area Synthesis of High-Quality and Uniform Graphene Films on Copper Foils. *Science (80-.).* **324,** 1312 –1314 (2009).

55. Li, X. *et al.* Transfer of Large-Area Graphene Films for High-Performance Transparent Conductive Electrodes. *Nano Lett.* **9,** 4359–4363 (2009).

56. Eda, G., Fanchini, G. & Chhowalla, M. Large-area ultrathin films of reduced graphene oxide as a transparent and flexible electronic material. *Nat. Nanotechnol.* **3,** 270–4 (2008).

57. Bae, S. *et al.* Roll-to-roll production of 30-inch graphene films for transparent electrodes. *Nat. Nanotechnol.* **5,** 574–578 (2010).

58. Hass, J. *et al.* Structural properties of the multilayer graphene/4H-SiC(0001¯) system as determined by surface x-ray diffraction. *Phys. Rev. B* **75,** 214109 (2007).

59. Kim, K. S. *et al.* Large-scale pattern growth of graphene films for stretchable transparent electrodes. *Nature* **457,** 706–710 (2009).

60. Li, X. *et al.* Large-Area Graphene Single Crystals Grown by Low-Pressure Chemical Vapor Deposition of Methane on Copper. *J. Am. Chem. Soc.* **133,** 2816–2819 (2011).

61. Li, X. *et al.* Graphene films with large domain size by a two-step chemical vapor deposition process. *Nano Lett.* **10,** 4328–34 (2010).

62. Yu, Q. *et al.* Control and characterization of individual grains and grain boundaries in graphene grown by chemical vapour deposition. *Nat. Mater.* **10,** 443–9 (2011).

63. Kim, D. W., Kim, Y. H., Jeong, H. S. & Jung, H.-T. Direct visualization of large-area graphene domains and boundaries by optical birefringency. *Nat. Nanotechnol.* **7,** 29–34 (2011).

64. Yazyev, O. V. & Louie, S. G. Electronic transport in polycrystalline graphene. *Nat. Mater.* **9,** 806–809 (2010).

65. Smith, N. V. Classical generalization of the Drude formula for the optical conductivity. *Phys. Rev. B* **64,** 155106 (2001).

66. Homes, C. *et al.* Optical conductivity of the stable icosahedral quasicrystal Al_{63.5}Cu_{24.5}Fe_{12}. *Phys. Rev. Lett.* **67,** 2694–2696 (1991).

67. Henning, P. F. *et al.* Infrared Studies of the Onset of Conductivity in Ultrathin Pb Films. *Phys. Rev. Lett.* **83,** 4880–4883 (1999).

68. Cooke, D. G. *et al.* Transient terahertz conductivity in photoexcited silicon nanocrystal films. *Phys. Rev. B* **73,** 193311 (2006).

69. Cooke, D. G., Meldrum, A. & Uhd Jepsen, P. Ultrabroadband terahertz conductivity of Si nanocrystal films. *Appl. Phys. Lett.* **101,** 211107 (2012).

70. Gordon M. Turner, Matthew C. Beard, and & Schmuttenmaer*, C. A. Carrier Localization and Cooling in Dye-Sensitized Nanocrystalline Titanium Dioxide. (2002).

71. Beard, M. C. *et al.* Electronic Coupling in InP Nanoparticle Arrays. *Nano Lett.* **3,** 1695–1699 (2003).

72. Cheung, K. P. & Auston, D. H. A novel technique for measuring far-infrared absorption and dispersion. *Infrared Phys.* **26,** 23–27 (1986).

73. Exter, M. van, Fattinger, C. & Grischkowsky, D. Terahertz time-domain spectroscopy of water vapor. *Opt. Lett.* **14,** 1128 (1989).

74. Winnewisser, G. Spectroscopy in the terahertz region. *Vib. Spectrosc.* **8,** 241–253 (1995).

75. Černe, J. *et al.* Terahertz Dynamics of Excitons in GaAs/AlGaAs Quantum Wells. *Phys. Rev. Lett.* **77,** 1131–1134 (1996).

76. Auston, D. H., Cheung, K. P. & Smith, P. R. Picosecond photoconducting Hertzian dipoles. *Appl. Phys. Lett.* **45,** 284 (1984).

77. Fattinger, C. & Grischkowsky, D. Terahertz beams. *Appl. Phys. Lett.* **54,** 490 (1989).

78. Yang, K. H., Richards, P. L. & Shen, Y. R. Generation of Far-Infrared Radiation by Picosecond Light Pulses in LiNbO3. *Appl. Phys. Lett.* **19,** 320 (1971).

79. Hu, B. B., Zhang, X.-C., Auston, D. H. & Smith, P. R. Free-space radiation from electro-optic crystals. *Appl. Phys. Lett.* **56,** 506 (1990).

80. Nahata, A., Weling, A. S. & Heinz, T. F. A wideband coherent terahertz spectroscopy system using optical rectification and electro-optic sampling. *Appl. Phys. Lett.* **69,** 2321 (1996).

81. Wu, Q. & Zhang, X.-C. Free-space electro-optic sampling of terahertz beams. *Appl. Phys. Lett.* **67,** 3523 (1995).

82. Jepsen, P. *et al.* Detection of THz pulses by phase retardation in lithium tantalate. *Phys. Rev. E* **53,** R3052–R3054 (1996).

83. Nahata, A., Auston, D. H., Heinz, T. F. & Wu, C. Coherent detection of freely propagating terahertz radiation by electro-optic sampling. *Appl. Phys. Lett.* **68,** 150 (1996).

84. Thomson, M. D., Blank, V. & Roskos, H. G. Terahertz white-light pulses from an air plasma photo-induced by incommensurate two-color optical fields. *Opt. Express* **18,** 23173–82 (2010).

85. Dai, J., Liu, J. & Zhang, X.-C. Terahertz Wave Air Photonics: Terahertz Wave Generation and Detection With Laser-Induced Gas Plasma. *IEEE J. Sel. Top. Quantum Electron.* **17,** 183–190 (2011).

86. Walther, M., Plochocka, P., Fischer, B., Helm, H. & Uhd Jepsen, P. Collective vibrational modes in biological molecules investigated by terahertz time-domain spectroscopy. *Biopolymers* **67,** 310–3 (2002).

87. Nuss, M. C. *et al.* Terahertz time-domain measurement of the conductivity and superconducting band gap in niobium. *J. Appl. Phys.* **70,** 2238 (1991).

88. Kaindl, R. A., Carnahan, M. A., Hägele, D., Lövenich, R. & Chemla, D. S. Ultrafast terahertz probes of transient conducting and insulating phases in an electron-hole gas. *Nature* **423,** 734–8 (2003).

89. Huber, R., Kaindl, R., Schmid, B. & Chemla, D. Broadband terahertz study of excitonic resonances in the high-density regime in GaAs∕AlxGa1−xAs quantum wells. *Phys. Rev. B* **72,** 161314 (2005).

90. Huber, R. *et al.* How many-particle interactions develop after ultrafast excitation of an electron-hole plasma. *Nature* **414,** 286–289 (2001).

91. Schall, M., Walther, M. & Uhd Jepsen, P. Fundamental and second-order phonon processes in CdTe and ZnTe. *Phys. Rev. B* **64,** 094301 (2001).

92. Schmuttenmaer, C. A. Exploring dynamics in the far-infrared with terahertz spectroscopy. *Chem. Rev.* **104,** 1759–79 (2004).

93. Schall, M. & Jepsen, P. U. Photoexcited GaAs surfaces studied by transient terahertz time-domain spectroscopy. *Opt. Lett.* **25,** 13 (2000).

94. Lui, K. P. H. & Hegmann, F. A. Ultrafast carrier relaxation in radiation-damaged silicon on sapphire studied by optical-pump–terahertz-probe experiments. *Appl. Phys. Lett.* **78,** 3478 (2001).

95. Auston, D. H. Picosecond optoelectronic switching and gating in silicon. *Appl. Phys. Lett.* **26,** 101 (1975).

96. Fattinger, C. & Grischkowsky, D. Point source terahertz optics. *Appl. Phys. Lett.* **53,** 1480 (1988).

97. Yang, Y., Mandehgar, M. & Grischkowsky, D. Time domain measurement of the THz refractivity of water vapor. *Opt. Express* **20,** 26208–18 (2012).

98. Lee, Y.-S. *Principles of Terahertz Science and Technology*. (Springer, 2008).

99. Jepsen, P. U., Jacobsen, R. H. & Keiding, S. R. Generation and detection of terahertz pulses from biased semiconductor antennas. *J. Opt. Soc. Am. B* **13,** 2424–2436 (1996).

100. Cook, D. J. & Hochstrasser, R. M. Intense terahertz pulses by four-wave rectification in air. *Opt. Lett.* **25,** 1210 (2000).

101. Löffler, T., Jacob, F. & Roskos, H. G. Generation of terahertz pulses by photoionization of electrically biased air. *Appl. Phys. Lett.* **77,** 453 (2000).

102. Xie, X., Dai, J. & Zhang, X.-C. Coherent Control of THz Wave Generation in Ambient Air. *Phys. Rev. Lett.* **96,** 075005 (2006).

103. Dai, J., Xie, X. & Zhang, X.-C. Detection of Broadband Terahertz Waves with a Laser-Induced Plasma in Gases. *Phys. Rev. Lett.* **97,** (2006).

104. Matsubara, E., Nagai, M. & Ashida, M. Coherent infrared spectroscopy system from terahertz to near infrared using air plasma produced by 10-fs pulses. *J. Opt. Soc. Am. B* **30,** 1627 (2013).

105. Kress, M., Löffler, T., Eden, S., Thomson, M. & Roskos, H. G. Terahertz-pulse generation by photoionization of air with laser pulses composed of both fundamental and second-harmonic waves. *Opt. Lett.* **29,** 1120 (2004).

106. Karpowicz, N. & Zhang, X.-C. Coherent Terahertz Echo of Tunnel Ionization in Gases. *Phys. Rev. Lett.* **102,** 093001 (2009).

107. Dai, J., Karpowicz, N. & Zhang, X.-C. Coherent Polarization Control of Terahertz Waves Generated from Two-Color Laser-Induced Gas Plasma. *Phys. Rev. Lett.* **103,** 023001 (2009).

108. Kim, K.-Y., Glownia, J. H., Taylor, A. J. & Rodriguez, G. Terahertz emission from ultrafast ionizing air in symmetry-broken laser fields. *Opt. Express* **15,** 4577 (2007).

109. Kim, K. Y., Taylor, A. J., Glownia, J. H. & Rodriguez, G. Coherent control of terahertz supercontinuum generation in ultrafast laser–gas interactions. *Nat. Photonics* **2,** 605–609 (2008).

110. Zhong, H., Karpowicz, N. & Zhang, X.-C. Terahertz emission profile from laser-induced air plasma. *Appl. Phys. Lett.* **88,** 261103 (2006).

111. You, Y. S., Oh, T. I. & Kim, K. Y. Off-Axis Phase-Matched Terahertz Emission from Two-Color Laser-Induced Plasma Filaments. *Phys. Rev. Lett.* **109,** 183902 (2012).

112. Klarskov, P., Strikwerda, A. C., Iwaszczuk, K. & Jepsen, P. U. Experimental three-dimensional beam profiling and modeling of a terahertz beam generated from a two-color air plasma. *New J. Phys.* **15,** 075012 (2013).

113. Klarskov, P., Wang, T., Buron, J. D., Strikwerda, A. C. & Jepsen, P. U. Spatial properties of a terahertz beam generated from a two-color air plasma. in *SPIE Opt. Eng. + Appl.* (Razeghi, M., Baranov, A. N. & Zavada, J. M.) 88460R–88460R–9 (International Society for Optics and Photonics, 2013). doi:10.1117/12.2023821

114. Xie, X., Dai, J. & Zhang, X.-C. Coherent Control of THz Wave Generation in Ambient Air. *Phys. Rev. Lett.* **96,** (2006).

115. Karpowicz, N. *et al.* Coherent heterodyne time-domain spectrometry covering the entire "terahertz gap."*Appl. Phys. Lett.* **92,** 011131 (2008).

116. Wang, C. S., Chen, J. M., Becker, R. & Zdetsis, A. Second order Raman spectrum and phonon density of states of silicon. *Phys. Lett. A* **44,** 517–518 (1973).

117. Wei, S. & Chou, M. Phonon dispersions of silicon and germanium from first-principles calculations. *Phys. Rev. B* **50,** 2221–2226 (1994).

118. Zalkovskij, M. Terahertz time-domain spectroscopy of chalcogenide glasses and devices for terahertz radiation manipulation. (2013).

119. Glover, R. & Tinkham, M. Conductivity of Superconducting Films for Photon Energies between 0.3 and 40kTc. *Phys. Rev.* **108,** 243–256 (1957).

120. Cooke, D. G. Time-resolved terahertz spectroscopy of bulk and nanoscale semiconductors. 194 LA – English (2006).

121. Tomaino, J. L. *et al.* Terahertz imaging and spectroscopy of large-area single-layer graphene. *Opt. Express* **19,** 141–146 (2011).

122. Dawlaty, J. M. *et al.* Measurement of the optical absorption spectra of epitaxial graphene from terahertz to visible. *Appl. Phys. Lett.* **93,** 131905–131905–3 (2008).

123. Choi, H. *et al.* Broadband electromagnetic response and ultrafast dynamics of few-layer epitaxial graphene. *Appl. Phys. Lett.* **94,** 172102 (2009).

124. Jnawali, G., Rao, Y., Yan, H. & Heinz, T. F. Observation of a transient decrease in terahertz conductivity of single-layer graphene induced by ultrafast optical excitation. *Nano Lett.* **13,** 524–30 (2013).

125. Liu, W., Valdés Aguilar, R., Hao, Y., Ruoff, R. S. & Armitage, N. P. Broadband microwave and time-domain terahertz spectroscopy of

chemical vapor deposition grown graphene. *J. Appl. Phys.* **110,** 083510–083510–5 (2011).

126. Li, Z. Q. *et al.* Dirac charge dynamics in graphene by infrared spectroscopy. *Nat. Phys.* **4,** 532–535 (2008).

127. Ren, L. *et al.* Terahertz and Infrared Spectroscopy of Gated Large-Area Graphene. *Nano Lett.* **12,** 3711–3715 (2012).

128. Maeng, I. *et al.* Gate-Controlled Nonlinear Conductivity of Dirac Fermion in Graphene Field-Effect Transistors Measured by Terahertz Time-Domain Spectroscopy. *Nano Lett.* **12,** 551–555 (2012).

129. Buron, J. D. *et al.* Graphene Conductance Uniformity Mapping. *Nano Lett.* **12,** 5074–5081 (2012).

130. Hu, B. *et al.* Epitaxial growth of large-area single-layer graphene over Cu(111)/sapphire by atmospheric pressure CVD. *Carbon N. Y.* **50,** 57–65 (2012).

131. Wood, J. D., Schmucker, S. W., Lyons, A. S., Pop, E. & Lyding, J. W. Effects of polycrystalline cu substrate on graphene growth by chemical vapor deposition. *Nano Lett.* **11,** 4547–54 (2011).

132. Gao, L., Guest, J. R. & Guisinger, N. P. Epitaxial Graphene on Cu(111). (2010).

133. Grischkowsky, D. R., Keiding, S., Vanexter, M. & Fattinger, C. Far-infrared time-domain spectroscopy with terahertz beams of dielectrics and semiconductors. *J. Opt. Soc. Am. B-Optical Phys.* **7,** 2006–2015 (1990).

134. Dai, J., Zhang, J., Zhang, W. & Grischkowsky, D. Terahertz time-domain spectroscopy characterization of the far-infrared absorption and index of refraction of high-resistivity, float-zone silicon. *J. Opt. Soc. Am. B* **21,** 1379 (2004).

135. Petersen, D. H., Hansen, O., Lin, R. & Nielsen, P. F. Micro-four-point probe Hall effect measurement method. *J. Appl. Phys.* **104,** 013710–013710–10 (2008).

136. Berger, C. *et al.* Electronic confinement and coherence in patterned epitaxial graphene. *Science* **312,** 1191–6 (2006).

137. Petersen, C. . *et al.* Scanning microscopic four-point conductivity probes. *Sensors Actuators A Phys.* **96,** 53–58 (2002).

138. Petersen, D. H., Hansen, O., Hansen, T. M., Petersen, P. R. E. & Bøggild, P. Static contact micro four-point probes with <11nm positioning repeatability. *Microelectron. Eng.* **85,** 1092–1095 (2008).

139. Rymaszewski, R. Relationship between the correction factor of the four-point probe value and the selection of potential and current electrodes. *J. Phys. E.* **2,** 170–174 (1969).

140. Thorsteinsson, S. *et al.* Accurate microfour-point probe sheet resistance measurements on small samples. *Rev. Sci. Instrum.* **80,** 53902–53910 (2009).

141. Jeon, T.-I. & Grischkowsky, D. Characterization of optically dense, doped semiconductors by reflection THz time domain spectroscopy. *Appl. Phys. Lett.* **72,** (1998).

142. Hwang, C. *et al.* Fermi velocity engineering in graphene by substrate modification. *Sci. Rep.* **2,** (2012).

143. Němec, H., Kužel, P. & Sundström, V. Far-infrared response of free charge carriers localized in semiconductor nanoparticles. *Phys. Rev. B* **79,** 115309 (2009).

144. Lin, Y.-M. *et al.* Wafer-Scale Graphene Integrated Circuit. *Science (80-.).* **332,** 1294–1297 (2011).

145. Liao, L. *et al.* Sub-100 nm Channel Length Graphene Transistors. *Nano Lett.* **10,** 3952–3956 (2010).

146. Son, Y.-W., Cohen, M. L. & Louie, S. G. Half-metallic graphene nanoribbons. *Nature* **444,** 347–349 (2006).

147. Matyba, P. *et al.* Graphene and Mobile Ions: The Key to All-Plastic, Solution-Processed Light-Emitting Devices. *ACS Nano* **4,** 637–642 (2010).

148. Bao, Q. *et al.* Atomic-Layer Graphene as a Saturable Absorber for Ultrafast Pulsed Lasers. *Adv. Funct. Mater.* **19,** 3077–3083 (2009).

149. Feng, M., Zhan, H. & Chen, Y. Nonlinear optical and optical limiting properties of graphene families. *Appl. Phys. Lett.* **96,** 033107–033107–3 (2010).

150. Gu, T. *et al.* Regenerative oscillation and four-wave mixing in graphene optoelectronics. *Nat. Photonics* **6,** 554–559 (2012).

151. Boubanga-Tombet, S. *et al.* Ultrafast carrier dynamics and terahertz emission in optically pumped graphene at room temperature. *Phys. Rev. B* **85,** (2012).

152. Bonaccorso, F., Sun, Z., Hasan, T. & Ferrari, A. C. Graphene photonics and optoelectronics. *Nat. Photonics* **4,** 611–622 (2010).

153. Sutter, P. W., Flege, J.-I. & Sutter, E. A. Epitaxial graphene on ruthenium. *Nat. Mater.* **7,** 406–411 (2008).

154. Reina, A. *et al.* Large Area, Few-Layer Graphene Films on Arbitrary Substrates by Chemical Vapor Deposition. *Nano Lett.* **9,** 30–35 (2008).

155. Jepsen, P. U., Cooke, D. G. & Koch, M. Terahertz spectroscopy and imaging – Modern techniques and applications. *Laser Photon. Rev.* **5,** 124–166 (2011).

156. Katzenellenbogen, N. & Grischkowsky, D. Electrical characterization to 4 THz of N- and P-type GaAs using THz time-domain spectroscopy. *Appl. Phys. Lett.* **61,** 840 (1992).

157. Sensale-Rodriguez, B. *et al.* Broadband graphene terahertz modulators enabled by intraband transitions. *Nat. Commun.* **3,** 780 (2012).

158. Barraza-Lopez, S., Vanević, M., Kindermann, M. & Chou, M. Y. Effects of Metallic Contacts on Electron Transport through Graphene. *Phys. Rev. Lett.* **104,** (2010).

159. Huard, B., Stander, N., Sulpizio, J. A. & Goldhaber-Gordon, D. Evidence of the role of contacts on the observed electron-hole asymmetry in graphene. *Phys. Rev. B* **78,** 121402 (2008).

160. J. H. Lee, E., Balasubramanian, K., Weitz, R. T., Burghard, M. & Kern, K. Contact and edge effects in graphene devices. *Nat. Nanotechnol.* **3,** 486–490 (2008).

161. Khomyakov, P. A., Starikov, A. A., Brocks, G. & Kelly, P. J. Nonlinear screening of charges induced in graphene by metal contacts. *Phys. Rev. B* **82,** 115437 (2010).

162. Petersen, D. H. *et al.* Comparative study of size dependent four-point probe sheet resistance measurement on laser annealed ultra-shallow junctions. *J. Vac. Sci. Technol. B Microelectron. Nanom. Struct.* **26,** 362 (2008).

163. Clarysse, T. *et al.* in (Pawlak, B., Jones, K., Felch, S. & Hane, M.) **912,** 197–202 (Materials Research Society, 2006).

164. Clarysse, T. *et al.* Photovoltage versus microprobe sheet resistance measurements on ultrashallow structures. *J. Vac. Sci. Technol. B Microelectron. Nanom. Struct.* **28,** C1C8 (2010).

165. Clarysse, T. *et al.* Advanced carrier depth profiling on Si and Ge with micro four-point probe. *J. Vac. Sci. Technol. B Microelectron. Nanom. Struct.* **26,** 317 (2008).

166. Clarysse, T. *et al.* On the analysis of the activation mechanisms of sub-melt laser anneals. *Mater. Sci. Eng. B* **154–155,** 24–30 (2008).

167. Clarysse, T., Eyben, P., Hantschel, T. & Vandervorst, W. Towards sub-10 nm carrier profiling with spreading resistance techniques. *Mater. Sci. Semicond. Process.* **4,** 61–66 (2001).

168. Vandervorst, W. USJ metrology : from 0D to 3D analysis. *AIP Conf. Proc.* **931,** 233–245 (2007).

169. Wang, F., Petersen, D. H., Osterberg, F. W. & Hansen, O. Accuracy of micro four-point probe measurements on inhomogeneous samples: A probe spacing dependence study. in *2009 17th Int. Conf. Adv. Therm. Process. Semicond.* 1–6 (IEEE, 2009). doi:10.1109/RTP.2009.5373449

170. Klarskov, M. B. *et al.* Fast and direct measurements of the electrical properties of graphene using micro four-point probes. *Nanotechnology* **22,** 445702 (2011).

171. Sun, J. *et al.* Low Partial Pressure Chemical Vapor Deposition of Graphene on Copper. *IEEE Trans. Nanotechnol.* **11,** 255–260 (2012).

172. Sun, J., Lindvall, N., Cole, M. T., Teo, K. B. K. & Yurgens, A. Large-area uniform graphene-like thin films grown by chemical vapor deposition directly on silicon nitride. *Appl. Phys. Lett.* **98,** 252103–252107 (2011).

173. Sun, J., Cole, M. T., Lindvall, N., Teo, K. B. K. & Yurgens, A. Noncatalytic chemical vapor deposition of graphene on high-temperature substrates for transparent electrodes. *Appl. Phys. Lett.* **100,** 22102–22103 (2012).

174. Van Der Pauw, L. J. A method of measuring the resistivity and Hall coefficient on lamellae of arbitrary shape. **20,** 220–224 (1958).

175. Petersen, D. H. *et al.* Review of electrical characterization of ultra-shallow junctions with micro four-point probes. *J. Vac. Sci. Technol. B Microelectron. Nanom. Struct.* **28,** C1C27 (2010).

176. Jepsen, P. U. & Fischer, B. Dynamic range in terahertz time-domain transmission and reflectionspectroscopy. *Opt. Lett.* **30,** 29–31 (2005).

177. Mak, K. F. *et al.* Measurement of the Optical Conductivity of Graphene. *Phys. Rev. Lett.* **101,** 196405 (2008).

178. Nair, R. R. *et al.* Fine Structure Constant Defines Visual Transparency of Graphene. *Science (80-.).* **320,** 1308–1308 (2008).

179. Koon, D. W. & Knickerbocker, C. J. What do you measure when you measure resistivity? *Rev. Sci. Instrum.* **63,** 207–210 (1992).

180. Herring, C. Effect of Random Inhomogeneities on Electrical and Galvanomagnetic Measurements. *J. Appl. Phys.* **31,** 1939–1953 (1960).

181. Petersen, D. H. *et al.* High precision micro-scale Hall effect characterization method using in-line micro four-point probes. in *16th IEEE Int. Conf. Adv. Therm. Process. Semicond. 2008. RTP 2008* 251 –256 (IEEE, 2008). doi:10.1109/RTP.2008.4690563

182. Cooke, D. G., Krebs, F. C. & Jepsen, P. U. Direct Observation of Sub-100 fs Mobile Charge Generation in a Polymer-Fullerene Film. *Phys. Rev. Lett.* **108,** 056603 (2012).

183. Su, F.-Y. *et al.* Flexible and planar graphene conductive additives for lithium-ion batteries. *J. Mater. Chem.* **20,** 9644 (2010).

184. Liao, L. *et al.* High-speed graphene transistors with a self-aligned nanowire gate. *Nature* **467,** 305–308 (2010).

185. Lin, Y.-M. *et al.* Operation of Graphene Transistors at Gigahertz Frequencies. *Nano Lett.* **9,** 422–426 (2009).

186. Xia, F., Mueller, T., Lin, Y., Valdes-Garcia, A. & Avouris, P. Ultrafast graphene photodetector. *Nat. Nanotechnol.* **4,** 839–843 (2009).

187. www.investorintel.com. Game Changer: Grafoid's new patent-pending MesoGraf^{TM} technology sets the standard for high-energy-density graphene -.

188. Novoselov, K. S. *et al.* A roadmap for graphene. *Nature* **490,** 192–200 (2012).

189. Paul, M. J. *et al.* Terahertz imaging of inhomogeneous electrodynamics in single-layer graphene embedded in dielectrics. *Appl. Phys. Lett.* **101,** 091109 (2012).

190. Avouris, P. & Xia, F. Graphene applications in electronics and photonics. *MRS Bull.* **37,** 1225–1234 (2012).

191. Kamins, T. I. Hall Mobility in Chemically Deposited Polycrystalline Silicon. *J. Appl. Phys.* **42,** 4357 (1971).

192. Dean, C. R. *et al.* Boron nitride substrates for high-quality graphene electronics. *Nat. Nanotechnol.* **5,** 722–6 (2010).

193. Wang, H., Wu, Y., Cong, C., Shang, J. & Yu, T. Hysteresis of electronic transport in graphene transistors. *ACS Nano* **4,** 7221–8 (2010).

194. Kalon, G., Jun Shin, Y., Giang Truong, V., Kalitsov, A. & Yang, H. The role of charge traps in inducing hysteresis: Capacitance–voltage

measurements on top gated bilayer graphene. *Appl. Phys. Lett.* **99,** 083109 (2011).

8.2 List of Publications

8.2.1 Peer reviewed Journal publications

i. Jonas Due Buron, Dirch Hjorth Petersen, Peter Bøggild, David G. Cooke, Michael Hilke, Jie Sun, Eric Whiteway, Peter F. Nielsen, Ole Hansen, August Yurgens and Peter Uhd Jepsen, ***"Graphene conductance uniformity mapping"***. *Nano Letters,* vol. 12, issue nr. 10, pages 5074-5081, oct. 2012.

ii. Jonas Due Buron, Filippo Pizzocchero, Peter Uhd Jepsen and Peter Bøggild, ***"Large-area mapping of carrier mobility in graphene by electrically gated terahertz time-domain spectroscopy"***, Submitted to *Small,* oct. 2013.

iii. Jonas Due Buron, Filippo Pizzocchero, Peter Bøggild, Michael Hilke, Eric Whiteway and Peter Uhd Jepsen, ***"Observation of nano-localization by carrier back-scattering at THz frequencies in CVD graphene"***, in preparation.

iv. Filippo Pizzocchero, Jonas Due Buron, Natalie Kostesha, Bjarke Sørensen Jessen, Daved MacKenzie, Adam C. Stoot, Martin B. B. Larsen, Dirch Hjorth Petersen, P. Greenwood, Peter Uhd Jepsen, Peter Bøggild and Tim Booth, ***"Bubble-free electrochemical transfer of arbitrarily large graphene films from reusable substrate"***, in preparation

v. Filippo Pizzocchero, Dirch Hjorth Petersen, Jonas Due Buron, Bjarke Sørensen Jessen, Tim Booth, Peter Folmer Nielsen, Ole Hansen, Peter Uhd Jepsen and Peter Bøggild, ***"Electrically continuous synthesized graphene from single crystal copper (111)"***, in preparation

8.2.2 Conference Proceedings

- Jonas Due Buron, Dirch Hjorth Petersen, Peter Bøggild, David G. Cooke, Jie Sun, Michael Hilke, Eric Whiteway, Peter Folmer Nielsen, Avgust Yurgens and Peter Uhd Jepsen, ***"Quantitative mapping of large area graphene conductance"***, proceedings for

The 37th International Conference on Infrared, Terahertz and Millimeter waves, Wollongong, Australia, 23-28 Oct. 2012.

- Pernille Klarskov Pedersen, Tianwu Wang, Jonas Due Buron, Andrew C. Strikwerda and Peter Uhd Jepsen, ***"Spatial properties of a terahertz beam generated from a two-color air plasma"***, *SPIE Optical Engineering + Applications*, pages 88460R-88460R-9, 2013

8.2.3 Conference contributions

Presenter is underlined.

- Jonas Due Buron, Peter Uhd Jepsen, ***"Terahertz optical technology for sensing and spectroscopy"***, presentation at *PIERS 2013: Progress in electromagnetics research symposium*, Stockholm, Sweden, 12-15 august 2013.

- Morten Møller, Jonas Due Buron, Martin B. B. Larsen, Peter Bøggild, David MacKenzie, Filippo Pizzocchero, Tim Booth and Peter Uhd Jepsen, ***"Large area THz mapping of electrically controlled graphene conductance"***, presentation at *International workshop on Optical Terahertz Science and Technology 2013*, Kyoto, Japan, 1-5 April 2013.

- Jonas Due Buron, Dirch Hjorth Petersen, Morten Møller, Peter Bøggild, David G. Cooke, Jie Sun, Eric Whiteway, Michael Hilke, Alba Centeno, A. Pesquera, Amaia Zurutuza and Peter Uhd Jepsen, ***"Terahertz dynamics of graphene charge carriers"***, poster at *International workshop on the electronic properties of novel materials 2013*, Kirchberg, Austria, 2-9 March 2013.

- Jonas Due Buron, Dirch Hjorth Petersen, Peter Bøggild, David G. Cooke, Jie Sun, Michael Hilke, Eric Whiteway, Peter Folmer Nielsen, Avgust Yurgens and Peter Uhd Jepsen, ***"Correlation between THz AC and micro-four-point-probe DC conductivity***

mapping of graphene sheets”, presentation at *Laser and Tera-Hertz Science and Technology*, Wuhan, China, 1-2 November, 2012.

- Jonas Due Buron, Dirch Hjorth Petersen, Peter Bøggild, David G. Cooke, Jie Sun, Michael Hilke, Eric Whiteway, Peter Folmer Nielsen, Avgust Yurgens and Peter Uhd Jepsen, ***“Quantitative mapping of large area graphene conductance”***, presentation at *The 37th International Conference on Infrared, Terahertz and Millimeter waves*, Wollongong, Australia, 23-28 Oct. 2012.

- Jonas Due Buron, Dirch Hjorth Petersen, Peter Bøggild, David G. Cooke, Jie Sun, Michael Hilke, Eric Whiteway, Peter Folmer Nielsen, Avgust Yurgens and Peter Uhd Jepsen, ***“Terahertz and micro four point probe conductance mapping of large area graphene – a new light on defects”***, presentation at *Carbonhagen 2012*, Copenhagen, Denmark, 25-26 June 2012.

- Jonas Due Buron, Dirch Hjorth Petersen, Peter Bøggild, David G. Cooke, Jie Sun, Michael Hilke, Eric Whiteway, Peter Folmer Nielsen, Avgust Yurgens and Peter Uhd Jepsen, ***“Terahertz and M4PP conductivity mapping of large area CVD grown graphene films”***, presentation at *3rd EOS topical meeting on terahertz science and technology 2012*, Prague, Czech Republic, 17-20 June 2012

- Jonas Due Buron, Dirch Hjorth Petersen, Peter Bøggild, David G. Cooke, Jie Sun, Michael Hilke, Eric Whiteway, Peter Folmer Nielsen, Avgust Yurgens and Peter Uhd Jepsen, ***“Correlation between THz AC conductivity and DC conductivity mapping of large-area graphene”***, presentation at *International Conference on Optical, Optoelectronic and Photonics Materials and Applications*, Nara, Japan, 3-7 June 2012.

- Jonas Due Buron, David G. Cooke, Tim Booth, Peter Bøggild and Peter Uhd Jepsen, ***“Terahertz dynamics of graphene charge carriers”***, poster at *Carbonhagen 2010*, Copenhagen, Denmark, 15-16 November 2010.

8.2.4 Patent applications

European patent application number 13188295.3

METHOD FOR CHARACTERISATION OF ELECTRICAL PROPERTIES OF ULTRA-SHALLOW JUNCTIONS

Inventors:

Jonas Christian Due Buron

Peter Uhd Jepsen

Dirch Hjort Petersen

Filed with the European Patent Office on October 11 2013

European patent application number 13188296.1

METHOD FOR CHARACTERISATION OF ELECTRICAL PROPERTIES OF AN ARRAY OF LINEAR, PARTIALLY LINEAR, SUBSTANTIALLY LINEAR, OR OTHER ROTATIONALLY ANISOTROPIC CONDUCTIVE ELEMENTS

Inventors:

Jonas Christian Due Buron

Peter Uhd Jepsen

Dirch Hjort Petersen

Peter Bøggild

Filed with the European Patent Office on October 11 2013

Copyright:
Jonas Christian Due Buron
and DTU Fotonik
All rights reserved
ISBN: 978-87-93089-19-8

Published by:
DTU Fotonik
Department of Photonic Engineering
Technical University of Denmark
Ørstyeds Plads, building 343
DK-2800 Kgs. Lyngby

Jonas Christian Due Buron was born in 1984 in Rødovre, Denmark. He received the BSc and MSc degrees in physics and nanotechnology from the Technical University of Denmark in 2008 and 2010, respectively. During his MSc studies he spent 6 months at the Royal Melbourne Institute of Technology, Australia. In August 2010 he undertook his PhD studies at DTU Fotonik and DTU Nanotech, which were focused on the investigation of transport dynamics in graphene using terahertz time-domain spectroscopy and the development of terahertz time-domain spectroscopy as a versatile and reliable graphene metrology tool.

DTU Fotonik
Department of Photonics Engineering